UNIVERSITY OF CALIFORNIA SAN DIEGO

Stratified Ekman layer over a rough surface

A dissertation submitted in partial satisfaction of the
requirements for the degree
Doctor of Philosophy

in

Engineering Sciences (Mechanical Engineering)

by

Sungwon Lee

Committee in charge:

Professor Sutanu Sarkar, Chair
Professor Juan Carlos del Alamo
Professor Stefan G. Llewellyn Smith
Professor Robert Pinkel
Professor David Saintillan

2020

The dissertation of Sungwon Lee is approved, and it is acceptable in quality and form for publication on microfilm and electronically:

_____

_____

_____

_____

_____

Chair

University of California San Diego

2020

DEDICATION

To Grace,

my lovely wife,

whose sacrificial love for me

made it possible to complete this work,

and to our beautiful daughters,

Sophia & Rachel,

who are indeed a treasure from the Lord.

EPIGRAPH

There is a time for everything,

and a season for every activity

under the heavens

— Ecclesiastes 3:1

TABLE OF CONTENTS

LIST OF FIGURES

LIST OF TABLES

ACKNOWLEDGEMENTS

I would like to express my gratitude to my advisor Professor Sutanu Sarkar for his guidance and encouragement of my Ph.D. study at UCSD. I also want to thank my committee members, Prof. Juan Carlos del Alamo, Stefan G. Llewellyn Smith, Robert Pinkel, David Saintillan. It has been a pleasure to work in a good environment with great professors.

This work could not have been completed without support of my colleagues at CFDLAB: Hieu Pham, Anikesh Pal, Masoud Jalali, Karu Chongsiripinyo, Iman Gohari, Alexandra Vandine, Vicky Verma, Jose Ortiz, Pranav Suresh, Sheel Nidhan and Divyanshu Gola. I would like to thank them for the precious discussion and all the fun that we have in last 5 years.

I want to thank my Korean friends in UCSD: Eric Kim, Yikyung Yu and Sean Kim. We met at the course of MAE 294A! It is fun to study with you and I really enjoyed a coffee break with you. I also want to thank basketball team Uncle K, most of them are quite old to play basketball with young UCSD students. We should be proud of that we are the SD adult basketball league champion!

Chapter 3, in full, is a reprint of the material as it appears in "Journal of Fluid Mechanics" Sungwon Lee, S.M. Iman Gohari, Sutanu Sarkar, Cambridge-Press, vol.902, 2020. The dissertation author was the primary investigator and author of this paper. Chapter 4, in full, is a reprint of the material as it appears in "Journal of Physics: Conference Series" Jose L. Ortiz-Tarin, Sungwon Lee, Oscar Flores, Sutanu Sarkar, Institute of Physics, vol.1522, 2020. The dissertation author was one of the primary investigator and coauthor of this paper.

Finally, I want to thank my families: parents, parents-in-law, sister's family. I love you all.

VITA

2020	Ph. D. in Engineering Sciences (Mechanical Engineering), University of California San Diego, California, USA.
2007	M. S. in Mechanical and Aerospace Engineering (Fluid and Thermal Sciences), Seoul National University, Seoul, South Korea.
2005	B. S. in Mechanical and Aerospace Engineering, Seoul National University, Seoul, South Korea.

PUBLICATIONS

Sungwon Lee, S.M. Iman Gohari and Sutanu Sarkar (2020), "Direct numerical simulation of stratified Ekman layers over a periodic rough surface", *Journal of Fluid Mechanics*.

Jose L. Ortiz-Tarin, **Sungwon Lee**, Oscar Flores and Sutanu Sarkar (2020), "Global modes and large-scale structures in an Ekman boundary layer", *Journal of Physics: Conference Series*.

Noma Park, **Sungwon Lee**, Jungil Lee and Haecheon Choi (2006), "A dynamic subgrid-scale eddy viscosity model with a global model coefficient", *Physics of Fluids*.

ABSTRACT OF THE DISSERTATION

Stratified Ekman layer over a rough surface

by

Sungwon Lee

Doctor of Philosophy in Engineering Sciences (Mechanical Engineering)

University of California San Diego, 2020

Professor Sutanu Sarkar, Chair

Ekman layers over a rough surface are studied using direct numerical simulation (DNS). The roughness takes the form of periodic two-dimensional bumps whose non-dimensional amplitude is fixed at a small value ($h^+ = 15$) and whose mean slope is gentle. The neutral Ekman layer is subjected to a stabilizing cooling flux for approximately one inertial period ($2\pi/f$) to impose the stratification. The Ekman Boundary Layer (EBL) is in a transitionally rough regime and, without stratification, the effect of roughness is found to be mild in contrast to the stratified case. Roughness, whose effect increases with the slope of the bumps, changes the boundary layer qualitatively from the very stable (Mahrt, 1998) regime, which has a strong thermal inversion and a pronounced low-level jet, in the flat case to the stable regime, which has a weaker thermal inversion and

stronger surface-layer turbulence, in the rough cases. The flat case exhibits initial collapse of turbulence which eventually recovers, albeit with inertial oscillations in turbulent kinetic energy. The roughness elements interrupt the initial collapse of turbulence. In the quasi-steady state, the thickness of the turbulent stress profiles and of the near-surface region with sub-critical gradient Richardson number increase in the rough cases. Analysis of the turbulent kinetic energy (TKE) budget shows that, in the surface layer, roughness counteracts the stability-induced reduction of TKE production. The flow component, coherent with the surface undulations, is extracted by a triple decomposition, and leads to a dispersive component of near-surface turbulent fluxes. The significance of the dispersive component increases in the stratified cases. Motivated by the dynamics of the atmospheric boundary layer, we also examines the influence of Coriolis acceleration on wall-bounded turbulence. The large-scale structures of an Ekman boundary layer are compared to those of a channel. The distribution of energy across scales is studied by looking into the spectra of the velocity fluctuations. Linear stability analysis reveals the existence of an unstable range of wavenumbers which sustain the turbulence and lead to transverse "roll" structures observed in instantaneous snapshots of the flow. Finally, additional DNS has been performed to find the effect of the roughness geometry in counteracting the buoyancy. Changing the bump height without changing its aspect ratio has little influence. However, for sufficiently large surface cooling flux, roughness is unable to maintain a turbulent state. Comparison of all the simulated cases shows that the final value of Ri_b is sufficient to provide guidance on the overall state of the boundary layer and its characterization into the following regimes: (i) weakly stable, (ii) very stable with turbulence collapse and rebirth to a state of global intermittency, or (iii) very stable with turbulence collapse and no recovery.

Chapter 1

Introduction

The atmospheric boundary layer (ABL) is the lowest part of the Earth's atmosphere in which we live and breathe. It has been studied numerically by many researchers since the pioneering work of Deardorff (1972) concerning an unstable atmospheric boundary layer. The ABL is an important example in nature of wall-bounded turbulent flows. From the evolution of weather and climate patterns to the dispersion of contaminants, the dynamics of the ABL are critical to human activity. The variety of ABL processes, e.g. wind, diurnal cycle, surface roughness, stratification, and Coriolis acceleration have led to much fluid mechanics work in recent decades on surface-atmosphere interactions. One key aspect of this problem concerns the behaviour of the ABL at night. During the day, solar radiation warms the surface of the Earth and, under normal conditions, the air temperature decreases with height. At night, however, this effect is reversed and surface cooling leads to the formation of a stably stratified inversion layer with the potential to suppress turbulent motions (Townsend, 1967). The conditions under which surface cooling can completely or intermittently relaminarize the flow remain the subject of current research. Figure 1.1 shows a schematic diagram of the diurnal variation of the ABL. At sunrise, heating from Earth's surface gives rise to a convective boundary layer while, after sunset, heat loss from the surface terminates convection and creates a thin nocturnal boundary

layer due to radiative cooling. Similarly, a stable inversion is formed by winter-time cooling with the inversion strength being particularly strong at high latitudes and polar regions.

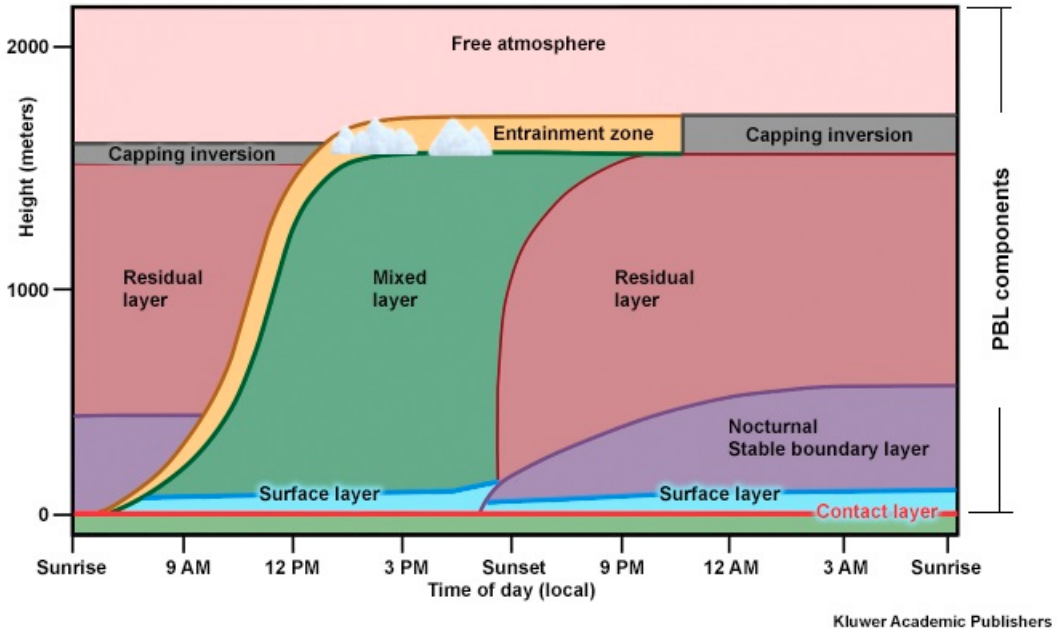

Figure 1.1: A schematic diagram of the diurnal variation of the atmospheric boundary layer (Stull, 1988)

The meteorology of the stable boundary layer includes states of continuous turbulence and intermittent turbulence (Businger, 1973). Mahrt (1998) categorized two prototypical states: the *weakly stable boundary layer* and the *very stable boundary layer*. The weakly stable boundary layer is normally characterized by windy conditions such that the surface cooling is relatively low. The very stable boundary layer is characterized by weak winds and clear skies that lead to strong net radiative cooling at the surface. The weakly stable boundary layer is described by the Monin-Obukhov similarity theory (Monin, 1970), in which turbulence, although reduced, is continuous. On the contrary, the very stable boundary layer is characterized by global intermittency where turbulence is reduced for periods which are long compared with the time scale of individual eddies (Mahrt, 1989). Internal gravity waves are also present in the very stable boundary layer.

The ABL flow field is strongly influenced by direct interaction with the surface of the earth. The surface-air interaction occurs in two primary forms: mechanical and thermal. Thermal turbulence is generally generated by unstable configurations of buoyancy while mechanical turbulence is generated by vertical wind shear. Turbulence is the primary mechanism for vertical exchange in the boundary layer where the flow is directly influenced by surface forcing, e.g. heating/cooling and friction. The mechanical contact between the wind and the ground surface leads to wind shear and creates turbulence. Surface friction, terrain and solar heating all influence the part of the atmosphere closest to the surface, leading to mechanical turbulence, convective activity and variation in wind direction and speed.

The turbulent boundary layer over a rough surface has been reviewed by Raupach et al. (1991) and Jiménez (2004), among others. One measure of roughness elements is their height as quantified by a roughness Reynolds number, $h^+ = h/\delta_\nu$, the ratio of the height of the elements to the viscous scale, δ_ν. With increasing h^+, the boundary layer changes from a smooth to a transitionally rough to a fully-rough boundary layer. The fully-rough boundary layer has enhanced momentum transport and drag. For a given h^+, the shape and spatial distribution of the roughness elements are important as reviewed by Flack and Schultz (2010) among others. In the present work, we consider a periodic array of sinusoidal bumps with moderate slope (figure 3.1). The analogous problem of unstratified flow over a wavy bottom has received attention in experiments (Zilker et al., 1977; Gong et al., 1996)) and, more recently, in numerical studies using DNS or wall-resolved LES (e.g., De Angelis et al. (1997); Sullivan et al. (2000); Napoli et al. (2008); Yang and Shen (2010)). Turbulent flow over rough surfaces has a component in the time-averaged field which is coherent with the surface structure and gives rise to a dispersive component of the turbulent fluxes. The coherent velocity can be extracted using a triple decomposition, and the so-called dispersive component is a significant contributor to turbulent fluxes in the near-surface layer (Finnigan, 2000; Sullivan et al., 2000; Poggi et al., 2004; Li and Bou-Zeid, 2019).

There is not much systematic study of the competing effects of stable stratification and

roughness in canonical problems. Ohya et al. (1997) and Ohya (2001) performed laboratory experiments of stratified boundary layers that develop in a wind tunnel over smooth and rough surfaces, respectively. The bottom wall in the rough case had a two-dimensional roughness imposed by a chain of oval rings and had a colder temperature than the bulk flow with $\Delta\theta$ varying between 27.4K and 44.1K. Vertical profiles showed reduction of turbulence levels with increasing stability in both rough and smooth cases. Sullivan and McWilliams (2002) conducted DNS of turbulent Couette flow over waves (including the stationary-wave case) under moderate stable and unstable stratification. Their results show a decrease (increase) of turbulence levels under stable (unstable) stratification.

Turbulence in the boundary layer can collapse in the presence of sufficiently strong stability. Banta et al. (2007) find long periods of suppressed turbulence in nights with a strongly stable ABL. The near-surface layer appears to decouple from the upper regions of the ABL during these episodes of suppressed turbulence. The bulk Richardson number, Ri_b, defined later by Eq. (3.7), is a critical parameter with large values of Ri_b indicative of large stability. During periods with $Ri_b > 2$ during the CASES-99 observational campaign, the coupling between the near-surface layer and the outer layer was found to be weak. Correspondingly, two layers of turbulent kinetic energy (TKE) surrounding a local minimum were identified by Banta et al. (2007) and Cuxart and Jiménez (2007). Such a two-layer configuration of TKE was also found in a recent direct numerical simulation (DNS) of the stratified Ekman boundary layer by Gohari and Sarkar (2018).

Turbulence in the boundary layer can collapse in the presence of sufficiently strong stability. Banta et al. (2007) found long periods of suppressed turbulence during nights with a strongly stable ABL. The near-surface layer appears to decouple from the upper regions of the ABL during these episodes of suppressed turbulence. The bulk Richardson number (Ri_b, defined later by Eq. (3.7)) is a critical parameter; large values of Ri_b are indicative of strong stability. During periods with $Ri_b > 2$ in the Cooperative Atmosphere-Surface Exchange Study in 1999

(CASES-99) observational campaign, the coupling between the near-surface layer and the outer layer was found to be weak (Poulos et al., 2002a). Two layers of turbulent kinetic energy (TKE), one above and the other below a local minimum of TKE, were identified by Banta et al. (2007) and Cuxart and Jiménez (2007). Such a two-layer configuration of TKE was also found in a recent DNS of the stratified Ekman boundary layer by Gohari and Sarkar (2018).

The so-called Ekman boundary layer (EBL) is a simplified example of the ABL, whereby a boundary layer in a rotating reference frame develops under unidirectional horizontal flow in geostrophic balance (Coriolis acceleration is equal and opposite to the pressure gradient, both being orthogonal to the flow). The stable EBL is a canonical problem for studying the stabilization of the ABL. DNS studies of the stable EBL have imposed buoyancy with a constant temperature boundary condition (Ansorge and Mellado, 2014; Shah and Bou-Zeid, 2014; Deusebio et al., 2014) or with a constant cooling flux (Gohari and Sarkar, 2017, 2018); these studies were performed with a smooth bottom boundary. The boundary-layer response to stability in these studies spanned various regimes of turbulence, depending on the relative strength of the stability: initial decrease of turbulence and even collapse of turbulence to a laminar state; recovery to continuous turbulence; recovery to global intermittency where turbulent near-surface patches co-exist with laminar flow; and, finally, episodes of complete turbulence collapse followed by recovery to spatially intermittent turbulence.

None of the Ekman layer DNS have considered surface roughness, which is often a feature of the ABL. This motivates the present research that addresses how the destabilizing effect of surface roughness competes with the stabilizing effect of surface cooling in the EBL. The simulation results are related to meteorological characteristics that are distinctive features of the stable ABL: low-level jets (Smedman et al., 1993; Cuxart et al., 2000; Banta et al., 2002), collapse of surface-layer turbulence (Banta et al., 2007), local turbulence peaks at locations above the surface layer (Mahrt, 1985; Smedman et al., 1993; Banta et al., 2007), and unsteadiness of turbulence statistics (Banta, 2008; Sun et al., 2012; Pichugina et al., 2008). These characteristics

not only change the atmospheric dispersion of tracers and pollutants as has been well-documented in the past but also, as discussed in recent work, strongly influence acoustic propagation in the nocturnal boundary layer (Talmadge et al., 2008) with this influence being modified by hilly terrain (Damiens et al., 2018).

Chapter 2

Formulation and Numerical Method

In the study of the stratified EBL, several important physical parameters arise: the geostrophic wind U_∞, the Coriolis frequency f, the turbulent Ekman layer thickness δ_*, and the friction Reynolds number Re_*. We will explain the importance of each parameter in DNS studies performed throughout this research.

2.1 Governing equations

Usually, the density varies little across the lowest part of the atmosphere. Nevertheless, density fluctuations give rise to buoyancy forces that cannot be ignored in the momentum balance. To develop dynamical equations for application to the ABL, we make an important simplification known as the Boussinesq approximation. In this approximation, density is replaced by a constant mean value, ρ_0, everywhere except in the buoyancy term of the vertical momentum equation. The governing equations for the conservation of momentum under the Boussinesq approximation and potential temperature in a rotating reference frame are

$$\frac{\partial u_i}{\partial t} + \frac{\partial (u_i u_j)}{\partial x_j} = -\frac{\partial p}{\partial x_i} + \nu \nabla^2 u_i + \delta_{i3} \beta g \theta + f \varepsilon_{ij3} (u_j - U_\infty \delta_{j1}), \tag{2.1}$$

$$\frac{\partial \theta}{\partial t} + \frac{\partial (\theta u_j)}{\partial x_j} = \alpha \nabla^2 \theta. \tag{2.2}$$

Here t is time, x_j is the spatial coordinate in the j direction, u_j is the velocity component in that direction, p is the pressure deviation from the the mean pressure imposed by geostrophic and hydrostatic balance, δ_{i3} is the Kronecker delta, ε_{ij3} is the alternating unit tensor, ν is the molecular viscosity, β is the thermal expansion coefficient for air, g is the gravitational acceleration, f is the Coriolis parameter, α is the thermal diffusivity, and θ is the deviation of potential temperature from its constant reference value. The kinematic pressure, p, is computed by solving the Poisson equation that results from imposing zero velocity divergence at each time-step. The boundary conditions are no-slip and impermeability at the surface ($u_i = 0$), periodicity in the horizontal directions and stress-free ($\partial u_i / \partial z = 0$) with a Rayleigh damping to minimize the spurious reflection of gravity waves.

It can be shown that nondimensional Reynolds number and Prandtl number defined as,

$$Re_D = \frac{U_\infty D}{\nu}, \quad D = \sqrt{2\nu / f}, \quad Pr = \frac{\nu}{\alpha}, \tag{2.3}$$

are the only parameters controlling the dynamics of a neutral Ekman flow at steady-state, when the statistics have been adequately decorrelated from their initial condition (Spalart, 1988). Although the laminar Ekman-layer depth, D, is not a proper length scale describing the momentum transport in a turbulent Ekman flow, Re_D provides a universal comparison point among different Ekman flow studies. For a turbulent Ekman flow, it is proper to use the turbulent Ekman layer thickness, $\delta_N = u_* / f$, where u_* is the friction velocity which is defined below and subscript N denotes neutral conditions. The friction velocity and the friction Reynolds number (Re_*) are computed as

$$
\begin{aligned}
u_*^2 &= \nu\sqrt{\left(\frac{\partial\langle u\rangle}{\partial z}\right)^2+\left(\frac{\partial\langle v\rangle}{\partial z}\right)^2}\Big|_{z=0}, \\
Re_* &= \frac{u_*\delta_N}{\nu}.
\end{aligned} \tag{2.4}
$$

Hereafter, $\langle . \rangle$ denotes the Reynolds average, which is computed as a horizontal $x-y$ average when the flow statistics are evolving in time, and with an additional time average over an inertial period when the flow is quasi-steady. It is important to note that u_* and δ_N are functions of Reynolds number and are not known prior to simulation in Ekman layer studies. Denoted by superscript $+$, statistics normalized with the viscous scale (ν/u_*) are chosen to describe behavior in the near-surface region. Normalization of statistics, denoted by superscript $-$, by the boundary layer height (Ekman layer thickness δ_N) is also used.

2.2 Numerical method

The governing equations (2.1) and (2.2) are written in generalized curvilinear coordinates (ξ, η) as described by Gayen and Sarkar (2011). The equations are solved using mixed finite-difference/spectral discretization. It is a non-staggered grid system with grid lines aligning with the physical boundary and velocity and pressure defined at the cell center. Derivatives in the spanwise direction are treated with a pseudo-spectral method and derivatives in the vertical and streamwise directions are computed with second-order finite differences. An explicit low-storage third-order Runge-Kutta-Wray (RKW3) method is used for the advective terms while the viscous terms are treated implicitly with the alternating direction implicit (ADI) method. A multigrid Poisson solver is employed for the pressure. Variable time stepping with a fixed CFL number can be used. Periodicity is imposed in the spanwise direction on velocity, temperature θ and pressure, p. The computational domain can include a Rayleigh damping or a "sponge" layer

at the left and right or top boundaries. It can also have Neumann, Dirichlet, periodic or mixed boundary conditions. At the bottom boundary, grid orthogonality is ensured to accurately impose the condition of zero (or another prescribed value) normal heat flux and zero normal pressure gradient. In order to reduce the simulation runtime, it is common to distribute the data among the processes through domain decomposition by designing a parallel algorithm. Since this code uses pseudo-spectral method (only in the Y direction), an FFT is often executed inside the RKW3 substep to transform the velocity field from physical to Fourier space and vice-versa.

Chapter 3

Direct Numerical Simulation of stratified Ekman layer over a periodic rough surface

Stratified turbulent channel flow, a canonical problem to investigate buoyancy effects in wall-bounded flows, has received much attention (Garg et al., 2000; Armenio and Sarkar, 2002; Nieuwstadt, 2005; Flores and Riley, 2011; Garcia-Villalba and del Alamo, 2011; He and Basu, 2015). Armenio and Sarkar (2002) show initial collapse of turbulence in stratified channel flow followed by resurgence of turbulence. They find an outer layer with suppressed turbulence and wavy motion where the gradient Richardson number (Ri_g defined by Eq. 3.4) is larger than 0.2, and an inner layer with active turbulence where Ri_g decreases from 0.2 to a small value at the wall. Garcia-Villalba and del Alamo (2011), in their large-domain simulations, find global intermittency with laminar patches interspersed within turbulence when the stratification is strong. The surface cooling flux can be used to define the Obukhov length (L, defined later by Eq. 3.2), and its value (L^+, defined later by Eq. 3.3) relative to the viscous scale is an important measure of the strength of buoyancy. Flores and Riley (2011) propose a criterion for turbulence collapse based on L^+ decreasing to 100 during the initial transient. This occurred in their stratified channel with initial $L^+ = 683$.

Coleman et al. (1990); Ansorge and Mellado (2014); Shah and Bou-Zeid (2014); Deusebio et al. (2014) studied the stratified Ekman layer using DNS with a constant temperature imposed at the wall. In this problem, the surface buoyancy flux decreases with time although Ri_b is constant. Intriguing spatial intermittency was observed by Ansorge and Mellado (2014) in their DNS study of a stably stratified Ekman layer. Similar to Nieuwstadt (2005) and Flores and Riley (2011), initial turbulent collapse followed by recovery was observed when the surface temperature of a neutral Ekman layer was suddenly dropped to impose the prescribed value of stability, Ri_b. The spatial characteristics of intermittent turbulence were then analyzed in detail during this transient process. In neutrally stratified Ekman layers, Deusebio et al. (2014) found large-scale roll structures with one dominant frequency that matched the convective frequency of the low-level jet (LLJ). They also found that these counter-rotating streamwise vortices influence the near-wall structures by pushing or lifting fluid close to the wall. Shah and Bou-Zeid (2014), from analysis of the TKE budget, show that the reduction of turbulence levels in the stratified EBL is primarily due to the inhibition of shear production rather than the buoyant TKE destruction. Interestingly, this feature of buoyancy-induced reduction of turbulence production, which is key to the suppression of turbulence by density stratification is a generic feature of stratified shear flows and has been found by us in uniform shear flow (Jacobitz et al., 1997) and later in the shear layer (Brucker and Sarkar, 2007) and the stratified wake (Brucker and Sarkar, 2010). The decrease in turbulence production with increasing stratification is an indirect effect of buoyancy that decreases the correlation coefficient between streamwise and vertical velocity fluctuations. Gohari and Sarkar (2017) performed DNS of the Ekman layer with a constant buoyancy flux, and found differences of this constant-flux stability case with respect to previous cases with constant-temperature stability: the low-level jet is stronger, there are recurring episodes of collapse and rebirth of turbulence during the transient, and the TKE profile has local peaks at two vertical locations.

Recently, Gohari and Sarkar (2018) conducted DNS of a smooth-surface EBL that is

subject to a finite-time (approximately, one inertial period) cooling flux. They found that initial $L^+_{cri} = Lu^*/\nu \lesssim 700$ provides a cooling flux that is sufficiently strong to cause the initial collapse of turbulence independent of Reynolds number, Re_*, where L is the Obukhov length scale and u^* is the friction velocity. The turbulence collapse criterion for stratified Ekman flow is considered based on the normalized Obukhov length scale (Obukhov, 1971), L^+, and has similar values as inferred from the observational study of Banta et al. (2007) and the DNS of Flores and Riley (2011). The final state, for a fixed L^+ and a fixed cooling flux, was found to depend on Re_*, because an increase in initial Re_* (under the constraint of fixed L^+) is equivalent to an increase in Ri_b. In particular, an EBL with a final stability of $Ri_b \geq 2$ relaminarized.

To better understand the competing effects of surface roughness and cooling flux, we performed DNS of stably stratified turbulent Ekman layers where a cooling flux is imposed over finite time similar to Gohari and Sarkar (2018), but over rough surfaces too in contrast to the smooth-surface EBL simulations of Gohari and Sarkar (2018). The work is organized as follows. Section 3.1 describes the governing equations and the problem setup. Section 3.2 describes the l results of the simulations through the evolution of mean and turbulence statistics. Section 3.3 describes the flow structures by iso-surface visualizations and elucidates the role of coherent structures by a triple decomposition. Finally, Section 3.4 contains the discussion and conclusions.

3.1 Formulation

3.1.1 Surface roughness

The roughness takes the form of periodic two-dimensional bumps whose non-dimensional amplitude and aspect ratio are changed among cases. The rough surface, $\eta(x)$, which is generated by defining a harmonic function, $f(x) = -h\cos(2\pi x/\lambda)$, with wavelength λ and amplitude h,

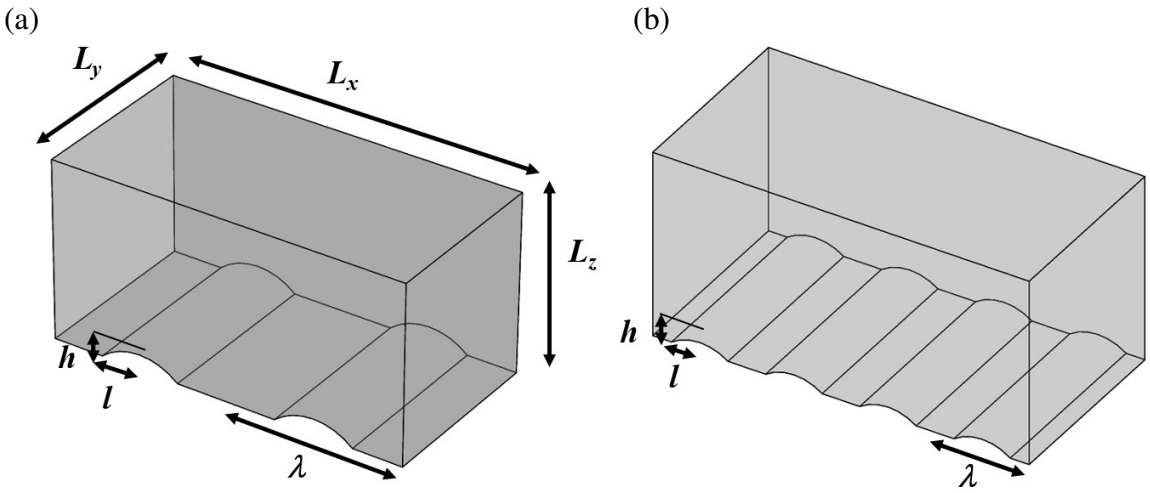

Figure 3.1: Schematic of the computational domain and surface roughness: (a) 2Bump and (b) 4Bump. L_x, L_y and L_z are the domain size in the streamwise, spanwise and vertical direction, respectively. $\lambda = L_x/N_b$, where N_b is the number of bumps, is the wavelength of the harmonic function that generates the bump. l=λ/4 is the half-length of the bump.

including only the positive ($z > 0$) portions of $f(x)$,

$$\eta(x) = \begin{cases} f(x) & \text{if } f(x) = -h\cos(2\pi x/\lambda) > 0, \\ 0 & \text{otherwise.} \end{cases} \tag{3.1}$$

A schematic of the roughness (figure 3.1) shows the surface has bumps but, unlike a surface wave, it has no troughs. This choice is motivated by the example of a layer thickness but has also gentle slope ($h/\lambda << 1$), so that, in the strong effect that substantially changes the flow with respect to its smooth-bottom The influence of roughness is found to extend up to the region ($Ri_g > 0.1$) where buoyancy alters the mean flow and turbulent stresses. The roughness has a small height so that, in the unstratified cases, it's effect is insignificant. In the stratified cases, as will be shown and explained, the same roughness height has a strong effect that substantially changes the flow with respect to its smooth-bottom counterpart.

The roughness amplitude, $h^+ = 15$, is kept constant, and the wavelength of the roughness is changed as follows: $\lambda = L_x/N_b$, where N_b is the number of bumps and the L_x is the streamwise

domain size. The aspect ratio of each bump is l/h where $l = \lambda/4$ is the half-length of the bump.

3.1.2 Buoyancy

Buoyancy is imposed by a surface flux, whose strength is quantified by the Obukhov length,

$$L = -\frac{u_*^3}{\kappa(\beta g q_0)}, \tag{3.2}$$

where κ is the von-Kármán constant and $q_0 = -\alpha\partial_z\theta|_{z=0}$ is the applied surface cooling flux. L provides an estimate of the height at which the buoyancy flux and turbulent energy production by mean shear are balanced. Using inner-layer scaling, the normalized Obukhov length becomes

$$L^+ = \frac{Lu_*}{\nu} = -\frac{u_*^4}{\kappa\nu(\beta g q_0)}. \tag{3.3}$$

The gradient Richardson number, a function of z and t in this flow, is defined by

$$Ri_g = \frac{N^2}{S^2}, \tag{3.4}$$

where $N^2 = g\beta\partial\langle\theta\rangle/\partial z$ is the squared buoyancy frequency and $S^2 = (\partial\langle u\rangle/\partial z)^2 + (\partial\langle v\rangle/\partial z)^2$ is the squared mean of the vertical shear. Large local values of Ri_g imply suppression of shear production of turbulence, and $Ri_g = 0.25$ is a stability boundary for the stratified shear layer. The non-dimensional inverse Obukhov length scale can also be interpreted in terms of Ri_g at the surface,

$$Ri_{g,s} = \frac{N^2}{S^2} = \frac{\beta g\partial_z\langle\theta_0\rangle}{u_*^4/\nu^2} = (\kappa L^+)^{-1}, \tag{3.5}$$

where $Pr = 1$ has been assumed. An alternative normalization of L is based on outer-layer coordinates,

$$L^- = \frac{L}{\delta_N}, \tag{3.6}$$

Table 3.1: Physical and numerical parameters used in the present Direct Numerical Simulations(DNS).

Case	Re_*	h^+	l^+	L_x/δ_N	L_y/δ_N	L_z/δ_N	$N_x \times N_y \times N_z$	Δx^+,Δy^+,Δz^+_{min}
Flat_N	697	-	-	4.09	2.05	2.05	$321 \times 256 \times 129$	8.46, 5.29, 0.98
Flat_S	**697**	-	-	4.09	2.05	2.05	$321 \times 256 \times 129$	8.46, 5.29, 0.98
2Bump_N	672	15	350	4.11	2.06	2.06	$481 \times 256 \times 129$	5.61, 5.26, 0.73
2Bump_S	**672**	15	350	4.11	2.06	2.06	$481 \times 256 \times 129$	5.61, 5.26, 0.73
4Bump_N	668	15	175	4.16	2.08	2.08	$481 \times 256 \times 129$	5.55, 5.20, 0.71
4Bump_S	**668**	15	175	4.16	2.08	2.08	$481 \times 256 \times 129$	5.55, 5.20, 0.71

*N_x, N_y, and N_z are the number of grid points in the streamwise, spanwise, and vertical direction respectively. The case label in column 1 ends with *N* (neutral case) or *S* (stable case), and starts with the number of bumps in the rough cases. In the stable cases, a surface buoyancy flux, chosen to obtain a target $L^+ \approx 700$, is applied for a finite time of $fT \approx 6$ and then the surface temperature is held constant. Note that δ_N is a measured parameter calculated from averages over the last $ft = 2$ of the neutrally stratified simulation at each Reynolds number.

where $\delta_N = u_*/f$ is the boundary-layer scale. The neutral EBL has a boundary-layer height of approximately $0.5\delta_N$. Since u_* is a time-dependent function in the stratified DNS cases, so are L, L^+ and L^-.

The bulk Richardson number, an overall stability measure of the flow, is defined as

$$Ri_b = \beta g \delta_N \frac{\langle \Delta\theta_0 \rangle}{U_\infty^2}, \tag{3.7}$$

where $\Delta\theta_0 = \theta_\infty - \theta_0$ is the difference between the temperature above the boundary layer and the surface temperature. In the present study the surface temperature (θ_0) is a time-dependent variable during the time interval, T, over which finite-time constant-flux stability is imposed. The value of Ri_b is also initially dependent on time but it becomes constant at the end of the time interval, T.

3.1.3 Numerical details

The governing equations (2.1) and (2.2) are numerically advanced in time using a combination of the low-storage third-order Runge-Kutta (RKW3) and mixed spectral-physical spatial discretization. The equations are written in generalized coordinates and the grid conforms to the bottom wall as described by Gayen and Sarkar (2011). Spatial discretization and derivative calculations in the spanwise direction are performed using Fourier transforms, and the derivatives in the streamwise and vertical directions are computed using a second-order central difference scheme. The nonlinear advection terms are dealiased with the 2/3 rule and a sharp-cutoff filter. The kinematic pressure, p, is computed by solving the Poisson equation that results from imposing zero velocity divergence at each time step. The boundary conditions for the velocity are no-slip and impermeability ($u_i = 0$) at the surface, periodicity in the horizontal directions and stress free ($\partial u_i/\partial z = 0$) at the upper boundary. The temperature gradient is fixed at the bottom surface to impose the desired cooling flux. A sponge region with Rayleigh damping is applied to u_i and θ to minimize the spurious reflection of gravity waves in the upper boundary ($z = L_z$). The in-house solver, which has been developed for environmental flows, has been applied to the Ekman boundary layer (Gohari and Sarkar, 2018) as well as complex geometries including stratified oscillating flow over a slope (Gayen and Sarkar, 2011) and a triangular ridge (Rapaka et al., 2013; Jalali et al., 2014).

A cooling flux, as determined by L^+, is imposed in the neutral cases too. The difference with the stratified series is that temperature is treated as a passive scalar in the neutral series with no feedback to the momentum equations. All of the rough and smooth-bottom stratified cases are initiated with a fully-developed velocity field taken from the corresponding neutral case. The passive-scalar temperature field from the neutral case is reset to a uniform background value so that each stratified case starts with zero temperature variation and stratification is allowed to build up in response to the applied surface buoyancy flux.

Parameters used in this DNS study are summarized in table 3.1. A fixed value of buoyancy

flux, corresponding to $L^+ \approx 700$, is applied for a time interval of $fT = 6$ in the stable cases. Note that the computational domain is enlarged to twice the streamwise domain of Gohari and Sarkar (2018), in order to better accomodate long streamwise structures. The resolution is $\Delta x^+ \approx 8.5$ in the streamwise direction for the flat bottom case and $\Delta y^+ \approx 5.2$ in the spanwise direction, similar to other DNS of wall-bounded flows. For the rough cases, the resolution in the streamwise direction is increased to $\Delta x^+ \approx 5.6$. In the vertical direction, ten grid points span $0 < z^+ \leq 10$ with a non-dimensional grid spacing $\Delta z^+_{min} \leq 1$.

The roughness height is kept constant at a small value of $h^+ = 15$ which corresponds to the transitionally-rough regime. The roughness takes the form of a periodic array of two-dimensional, spanwise-uniform elements whose surface elevation is given by Eq. (3.1). The roughness amplitude, $h^+ = 15$, is kept constant, and the wavelength of the roughness (λ) is changed. Note that $\lambda = L_x/N_b$, where N_b is the number of bumps and L_x is the streamwise domain size. In the simulations L_x is kept fixed and λ is changed by changing N_b. Doubling N_b decreases the element half-length ($l = \lambda/4$) by a factor of 2 and doubles the slope. The coverage of the bottom by the roughness elements is 50% of the wall area, independent of the number of bumps. The slope of each bump, given by h/l, is small and changes from 0.042 to 0.084 when N_b is doubled from 2 to 4. Another measure is the maximum slope, hk, where $k = 2\pi/\lambda$ is the wavenumber, changes from 0.06 to 0.12. We find that the flow does not separate at these values of slope. It is worth noting that the slope utilized here is below the critical slope for separation reported in the literature on a sinusoidal wavy surface where Gong et al. (1996); Sullivan et al. (2000) quote $hk > 0.3$ for flow separation, and Zilker et al. (1977) state that there is incipient separation at $2h/\lambda = 0.05$ and there are large separated regions at $2h/\lambda = 0.125$ and 0.20.

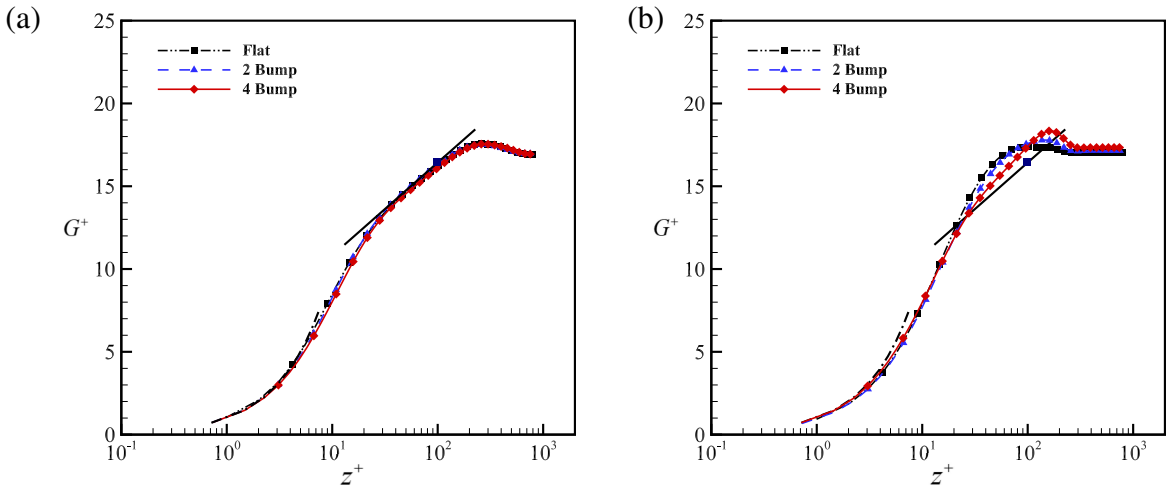

Figure 3.2: Mean velocity profiles: (a) neutral, and (b) stratified. Flat (- ▫ -), 2-bump (- △ -), and 4-bump (—◇—) cases are compared. The logarithmic law with $\kappa = 0.41$ and $B = 5.3$ is also shown. The statistics are averaged during one inertial time $ft \approx 2\pi$.

3.2 Results

The effect of the small-amplitude bumps on the velocity and temperature profiles in z is found to be insignificant under neutral conditions in contrast to the substantial effect under stratified conditions. This primary result is elaborated and explained in this section.

3.2.1 Overall structure of the boundary layer

Figure 3.2 shows the magnitude of normalized mean velocity, represented by $G^+ = \sqrt{\langle u \rangle^2 + \langle v \rangle^2}$, as a function of normalized vertical distance from the wall. The average is performed in streamwise and spanwise directions as well as in time. The solid line represents a log-law profile with the Von Karman constant κ=0.41 and B = 5.3. Profiles of the velocity in the unstratified (Figure 3.2a) bump cases are practically indistinguishable from the flat case at least until the end of the log law. The velocity in all cases obeys a linear profile from the wall until $z^+ \sim 5$, the boundary of the viscous sublayer. The viscous sublayer is followed by the buffer layer,

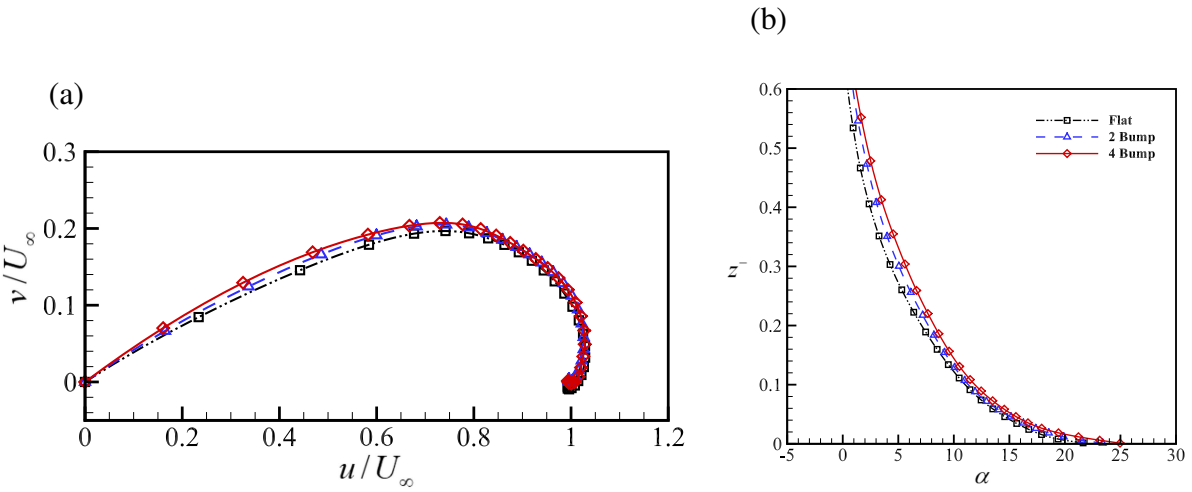

Figure 3.3: (a) Mean velocity hodograph showing the Ekman spiral and (b) the veering angle ($\alpha = \tan^{-1}(\langle v\rangle/\langle u\rangle)$) for flat: - -▫- - , 2-bump: - -△- - , 4-bump: —◇— in the unstratified results. The statistics are averaged during one inertial time $ft \approx 2\pi$.

$5 < z^+ < 30$, where advection gradually becomes important in the dynamics. Beyond $z^+ = 30$, there is an approach to the log law until $z^+ \approx 100$ (small square in Figure 3.2a), that corresponds to $z^- \approx 0.15$, where this deviates from the log-law. In the stratified cases (Figure 3.2b), the mean velocity profile is altered by buoyancy. There is an increase of momentum, corresponding to a low-level jet (LLJ), in what used to be the log-law region in the smooth-bottom case. The LLJ peak is located further away from the wall as the number of bumps increases. It is worth noting that, for the 4-bump case, the G^+ profile between $z^+ = 30$ and 100 moves closer to the log law.

Figure 3.3 shows mean velocity hodographs. representing (a) the Ekman spiral and (b) the veering angle (α) defined by $\alpha = \tan^{-1}(\langle v\rangle/\langle u\rangle)$ as a function of distance from the wall. The magnitude of veering angle is proportional to the number of bumps implying a reduction in a combination of lateral pressure gradient and surface drag required to balance the Coriolis acceleration.

The mean velocity is also examined using inner-layer coordinates. A least-squares fit to the vertical variation of $G = (\langle u\rangle^2 + \langle v\rangle^2)^{1/2}$ is performed to obtain the following profile in

semi-logarithmic coordinates:

$$G^+ = \frac{1}{\kappa}\ln z^+ + B \equiv \frac{1}{\kappa}\ln\frac{z^+}{{z_0}^+} \equiv \frac{1}{\kappa}\ln\frac{z}{z_0}\,, \tag{3.8}$$

where ${z_0}^+ = e^{-\kappa B}$. The values of $(\kappa, {z_0}^+)$ are (0.44, 0.0759), (0.43, 0.0814) and (0.40, 0.1187) in the Flat, 2Bump and 4Bump cases, respectively, and the profiles are as shown in figure 3.4. Sullivan et al. (2000) in their DNS of Couette flow found that, for a stationary bottom wall, ${z_0}^+ = 0.17$ in the flat-bottom case and ${z_0}^+ = 0.27$ for a wavy-bottom wall with $ak = 0.1$. Both cases exhibited $\kappa = 0.41$.

Monin-Obukhov(MO) similarity theory, often used to interpret ABL data, is utilized to assess the mean velocity and temperature profiles obtained here. Simulation data are used to compute stability functions (Φ_m and Φ_h) associated with MO similarity theory:

$$\Phi_m = \kappa z\frac{\sqrt{(\frac{\partial\langle u\rangle}{\partial z}(z))^2 + (\frac{\partial\langle v\rangle}{\partial z}(z))^2}}{u_*(z)} \quad , \quad \Phi_h = -\kappa z\frac{\frac{\partial\langle\theta\rangle}{\partial z}(z)}{\theta_*(z)}\,, \tag{3.9}$$

where $u_*(z)$ and $\theta_*(z)$ are the local scales for velocity and temperature fluctuations, as per local similarity theory (Nieuwstadt, 1984):

$$u_*(z)^2 = \nu\sqrt{\left(\frac{\partial\langle u\rangle}{\partial z}(z)\right)^2 + \left(\frac{\partial\langle v\rangle}{\partial z}(z)\right)^2} + \sqrt{\langle u'w'\rangle^2 + \langle v'w'\rangle^2}, \tag{3.10}$$

$$\theta_*(z)u_*(z) = \alpha\frac{\partial\langle\theta\rangle}{\partial z}(z) + \langle\theta'w'\rangle, \tag{3.11}$$

$$L_L(z) = -\frac{u_*(z)^3}{\kappa(\beta g q_0)}. \tag{3.12}$$

In the unstratified cases, Φ_h is computed using passive-scalar statistics (buoyancy term in the momentum equation is set to zero) and the computed value of L_L is to be understood as a notional value that allows comparison of profiles with the stratified cases.

Figure 3.5 shows normalized mean gradients (the so-called stability functions) for unstrat-

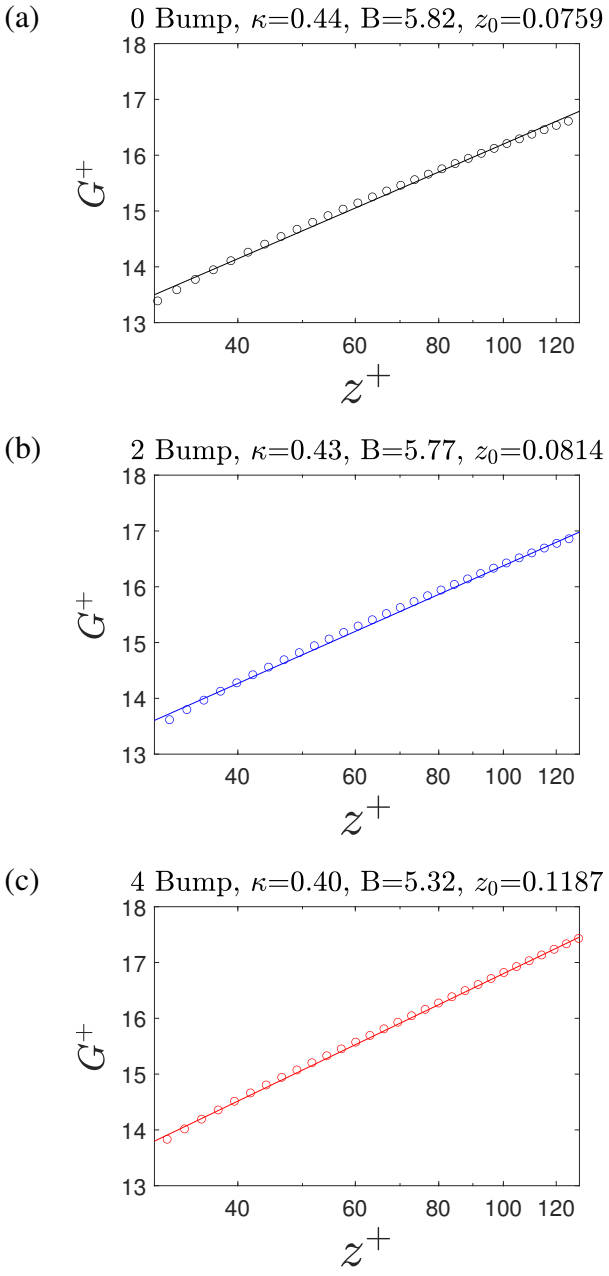

Figure 3.4: The mean velocity magnitude plotted in semi-logarithmic coordinates: (a) Flat $\kappa = 0.44$, $B = 5.82$, $z_0 = 0.0759$, (b) 2Bump $\kappa = 0.43$, $B = 5.77$, $z_0 = 0.0814$ and (c) 4Bump $\kappa = 0.40$, $B = 5.32$, $z_0 = 0.1187$.

ified (a,b) and stratified (c,d) Ekman layers. For the unstratified cases, $\Phi_m(z) = 1$ is expected in the log-law region and, correspondingly, $\Phi_m(z)$ takes values near unity over an extended region (Figure 3.5(a)). Very near the bottom and in the roughness sublayer, $\Phi_m(z)$ increases with increasing z. According to MO theory, Φ_m and Φ_h are constant and close to unity when $z/L_L << 1$; here L_L is the local Obukhov length. When $z/L_L \geq O(1)$, the turbulent length scale becomes limited by the local Obukhov length and $\Phi_m(z)$ increases with z. As shown in figure 3.5(c,d), there is a region, $0.02 < z/L_L < 0.1$, where Φ_m is approximately constant but greater than unity, followed by an increase of Φ_m as a function of increasing z/L_L . The function $\Phi_h(z)$ also increases with increasing z/L_L and exhibits a slope that is larger than that of $\Phi_m(z)$. Thus, the effect of buoyancy on heat transport is stronger than on momentum transport, i.e., the turbulent Prandtl number becomes larger than 1 in the stratified region of the boundary layer. The dependence of the stability functions on z/L_L in the present work is similar to that reported in previous studies, e.g., the LES of Basu and Porté-Agel (2006). It is worth noting that, in the surface layer and among the stratified cases, the 4Bump case shows behavior closest to the passive-scalar counterpart.

Figure 3.6 shows the horizontal mean velocity ($\sqrt{\langle u\rangle^2 + \langle v\rangle^2}/U_\infty$) profile of the EBL in the top row and the normalized potential temperature ($u_{*_N}(\theta - \theta_\infty)/q_0$) in the bottom row for both neutral (left column) and stratified (right column) cases. The statistics are obtained by averaging over the horizontal x-y plane and an average over one inertial period ($ft \approx 2\pi$). The temperature is treated as a passive scalar in the neutral cases. The velocity in the neutral flat-bottom case compares well with previous results (Shingai and Kawamura, 2004; Shah and Bou-Zeid, 2014; Ansorge and Mellado, 2014) at comparable *Re* as discussed by Gohari and Sarkar (2018).

Ansorge and Mellado (2014), Shah and Bou-Zeid (2014), and Deusebio et al. (2014) studied stably stratified Ekman boundary layers with a constant-temperature stability which means the temperature differences across the boundary are fixed. In contrast, Flores and Riley (2011) and Gohari and Sarkar (2017) studied stably stratified Ekman boundary layers when a constant cooling flux, $q_0 = -\beta\partial_z\langle\theta_0\rangle$ with θ_0 being the surface-temperature, was imposed at the

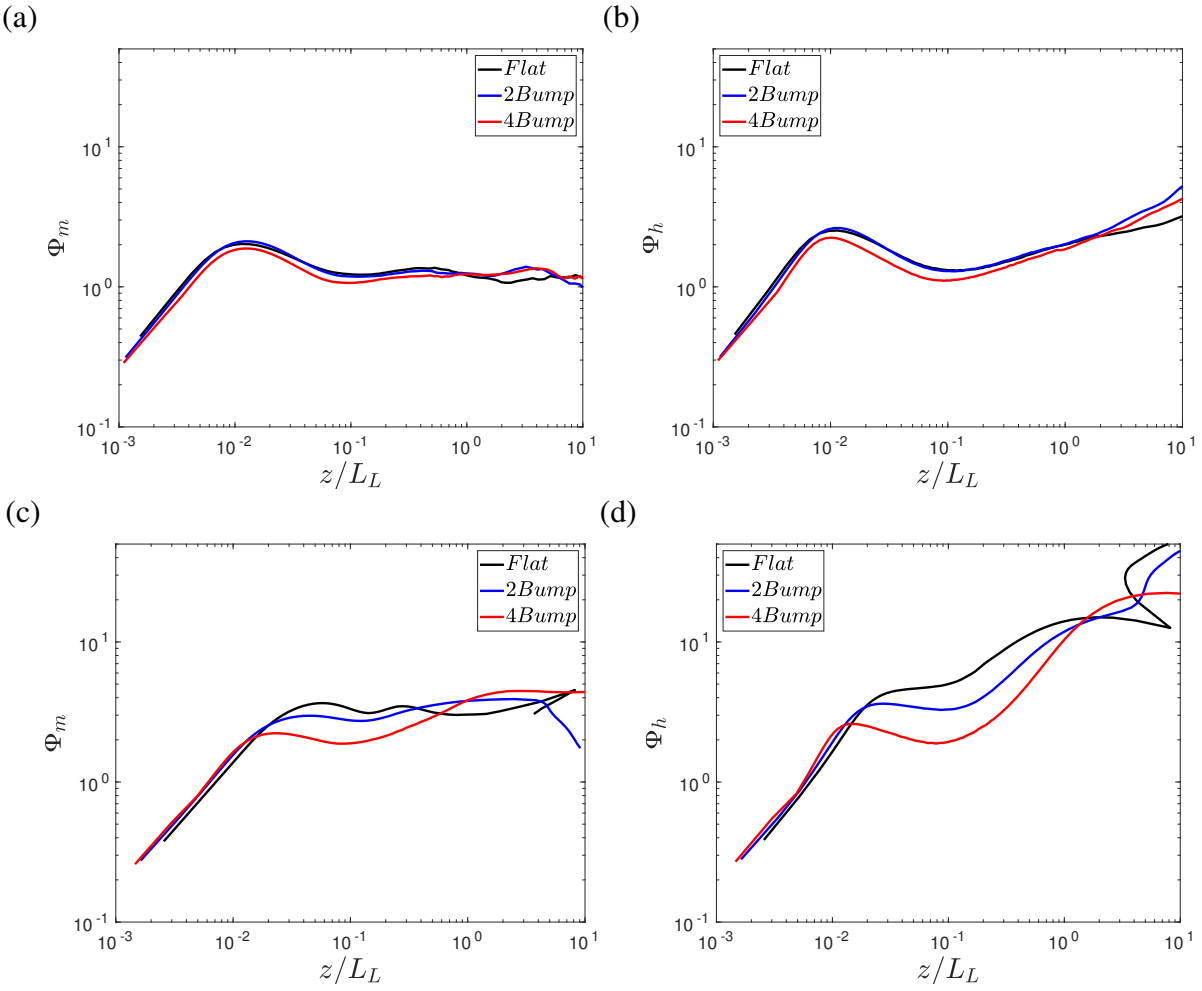

Figure 3.5: Normalized gradients (Φ_m and Φ_h defined by Eq. 3.9) of velocity (a,c) and temperature (b,d). Passive-scalar, unstratified cases are shown in the top row (a,b) and stratified cases in the bottom row (c,d).

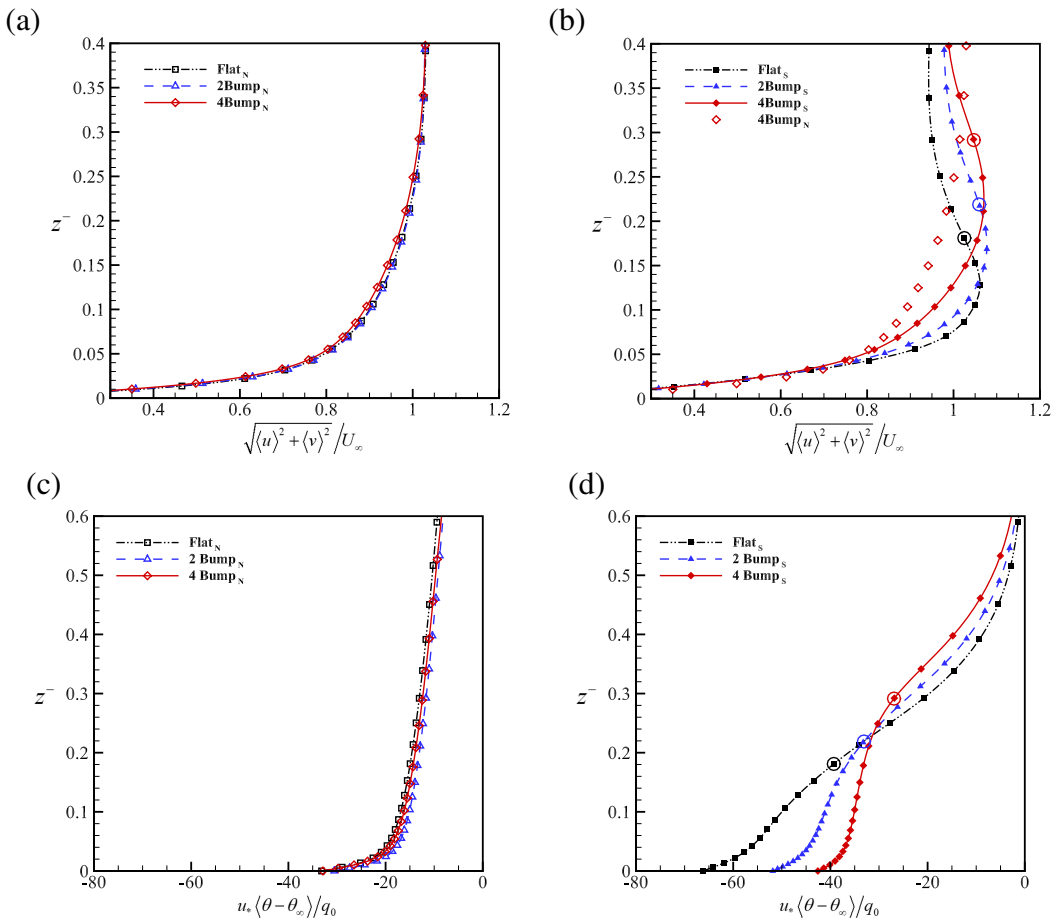

Figure 3.6: Mean velocity ($\sqrt{\langle u\rangle^2+\langle v\rangle^2}/U_\infty$) profiles: (a) neutral and (b) stratified cases. Potential temperature ($u_{*_N}(\theta-\theta_\infty)/q_0$) profiles: (c) neutral cases where θ is treated as a passive scalar, and (d) stratified cases. The large unfilled circle (right column) marks the time-evolving boundary-layer thickness ($z=\delta_t$), defined by Eq. (3.14).

surface. Thus, the nominal surface buoyancy flux (defined as $B_s = \beta g q_0$) was fixed in time. In this study, we use constant cooling flux for a finite time ($ft \approx 6$) to model the radiative cooling after the sunset.

The horizontal wind speed exhibits little difference among the neutral (figure 3.6(a)) flat and rough cases. Since the slope of the bump is gentle ($hk = 0.06$ and 0.12), the flow does not separate and the change in wall drag (shear stress plus form drag) is small. It is worth noting that DNS of turbulent flow over a sinusoidal wavy wall with $hk = 0.1$ in Couette flow (Sullivan et al., 2000) and channel flow (De Angelis et al., 1997) does not show flow separation. The stratified cases also do not exhibit flow separation; however, the mean velocity profiles (figure 3.6(b)) show a strong influence of roughness on the features of the LLJ that forms in the boundary layer. Each stratified case has a super-geostrophic velocity, commonly referred to as the LLJ. The formation of the LLJ is a distinctive feature of the stable ABL (Beare et al. (2006)) associated with the reduction of turbulent momentum flux by buoyancy. In the roughness layer at the surface, the bumps counteract the buoyancy-induced reduction of the momentum fluxes. Thus, the peak of the LLJ moves upward and the LLJ profile broadens. In the stratified 4Bump case (filled diamonds in figure 3.6(b)), the wind-speed profile in the region between the surface and $z^- = 0.1$ is close to the neutral case (open diamonds) while, in contrast, the 2Bump and Flat cases exhibit a significant deviation from the neutral case.

The present DNS results show a LLJ with a nose at $z \approx 0.1\delta_N$, with a maximum super-geostrophic overshoot of $u/u_\infty - 1 \approx 10\%$. DNS with stronger stability conducted by Gohari and Sarkar (2017) showed cases with LLJ at $z \approx 0.05\delta_N$ and $u/u_\infty - 1 \approx 50\%$. Considering typical values of $u_* \approx 0.3$ m/s and $f = 10^{-4}$ s^{-1} in the DNS-derived scaling gives a LLJ nose height of 150 m to 300 m in the stable ABL. This estimate of LLJ properties is consistent with several stable ABL studies: (i) Banta et al. (2007) reported LLJ nose height at approximately 150-300 m with velocity overshoot of 20-60%; (ii) Beare et al. (2006) reported LLJ nose height at approximately 150-180 m with an overshoot of 25% in LES studies; (iii) Banta et al. (2002) reported LLJ nose

height at approximately 100-200 m with a velocity overshoot of 10-70%; iv) Talmadge et al. (2008) reported observations of LLJ nose height at approximately 125 m in an ABL with strong ground cooling (see figure 4 in Talmadge et al. (2008)) ; v) Wilson et al. (2003) studied sound propagation in a stable nocturnal boundary layer which had a deep temperature inversion and LLJ at approximately 160m, and was observed during CASES-99 (Poulos et al., 2002b). It is worth noting that sloping terrain that leads to drainage flows also contributes to the LLJ structure (Mahrt, 1999).

In the neutral EBL (figure 3.6(a)) the effect of the surface roughness on the mean temperature is relatively small, similar to that on the velocity. However, in the stratified boundary layer (figure 3.6(b)) the bumps have a significant effect on the temperature distribution. The strong near-surface inversion of the Flat case is substantially weakened in the 4Bump case; the near-surface temperature field is more mixed, and its profile moves towards that of the neutral case. Thus, in spite of employing the identical value of surface cooling flux (q_0) in the three stratified cases, the surface temperature in the 4Bump case does not decrease as much as in the other stratified cases.

Figure 3.7 shows the overall influence of the bumps on the flow evolution. The integrated TKE, obtained by a horizontal x-y average to compute $\langle u_i' u_i' \rangle$ followed by integration in the vertical, is defined as

$$E = \int e \, dz = \frac{1}{2} \int_0^{L_z} \langle u_i' u_i' \rangle \, dz. \tag{3.13}$$

In all cases, TKE initially decreases during a period of turbulence collapse when the flow transitions from neutral to stable. For the Flat case, turbulence collapses with a timescale of L/u_* in agreement with Flores and Riley (2011). The collapse is followed by a recovery of TKE in each case. The turbulence recovery is consistent with DNS results of the stable EBL (Shah and Bou-Zeid, 2014; Ansorge and Mellado, 2014; Gohari and Sarkar, 2018). The value of u_* decreases by about 10-15 % during the initial transient before recovering to approximately its initial value. In an analysis of the CASES-99 data, Banta et al. (2007) reported a 6 hr collapse

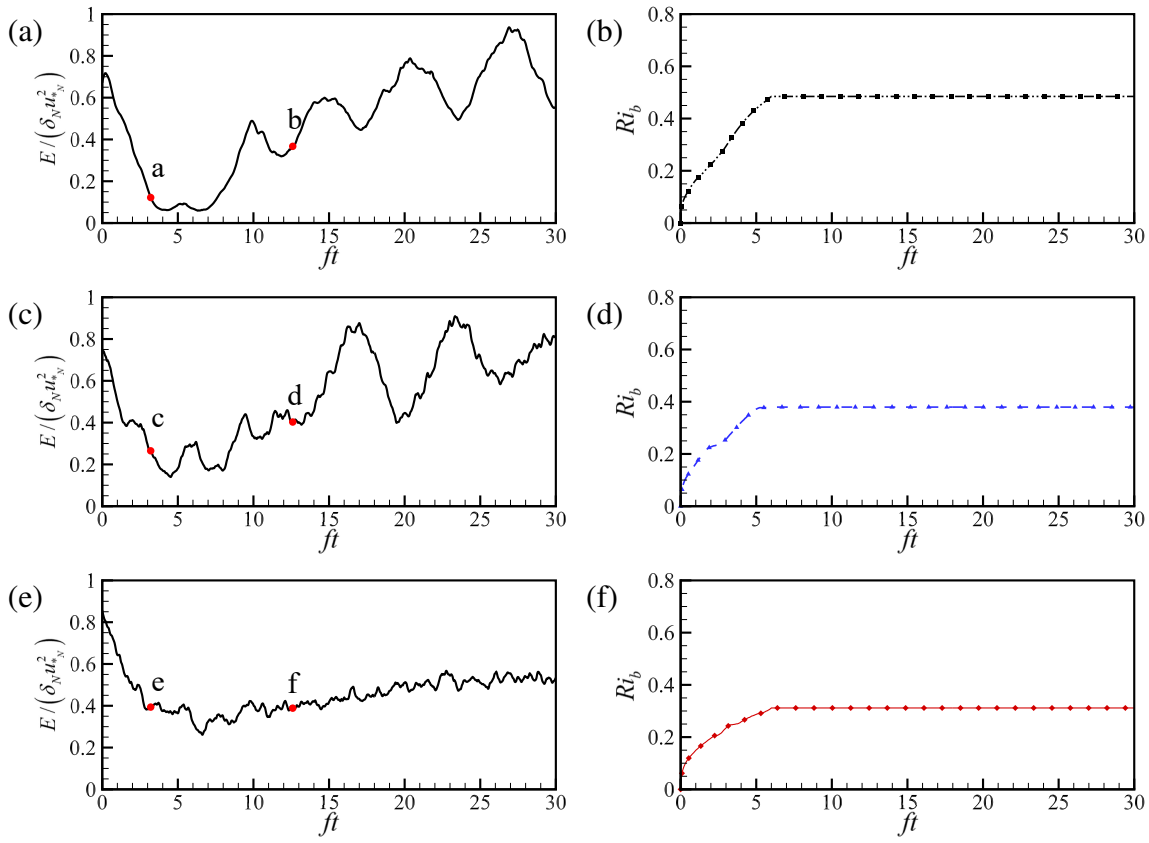

Figure 3.7: Overall behavior of the stratified cases at $Re_* \approx 700$: (a,b) Flat cases, (c,d) 2Bump case and (e,f) 4Bump cases. Left column shows integrated TKE ($E/(\delta_N u_{*_N}^2)$) and right column shows bulk Richardson number (Ri_b). Points a-f (left column) mark the times of (a-f) in figure 3.10.

time period which corresponds to a nondimensional time of $ft \approx 1.98$, which is similar to the DNS collapse time scale.

The TKE evolution after collapse exhibits significant differences among cases. In figure 3.7(a,c) for the Flat and 2Bump cases, TKE exhibits a large-amplitude inertial oscillation with period, $ft \approx 2\pi$. For the 4Bump case (figure 3.7(e)), the periodic modulation of TKE is not observed, but TKE exhibits a gradual increase (on average) and seems to reach a plateau beyond $ft \approx 25$. We will discuss reasons for the difference in TKE evolution later.

Figure 3.7 (c) shows the time series of TKE for the 2Bump case. Since turbulence is mechanically produced by the surface roughness, there is a balance between the stabilizing buoyancy flux and production of TKE. The competing effect between the two will be discussed in section 3.2.4. In spite of the production of the turbulence generated by geometry, TKE decreases when the flow transitions from neutral to stratified flow. The friction velocity decreases in the process of the transition and recovers after the rebirth of turbulence. In contrast, in the 4-bump case shown in figure 3.7 (e), TKE is reduced in the initial period of decay. Turbulence does not completely collapse and temporal intermittency is eliminated. In the 4Bump case, the shear production of the TKE is larger than the stabilizing buoyancy flux, so the collapse is not followed by a recovery period.

Figures 3.7 (b, d, f) show the bulk Richardson number defined as 3.7. We apply the same buoyancy flux for all cases; however, the final Ri_b is different among the three cases. The final value of Ri_b for Flat, 2Bump and 4Bump cases is 0.485, 0.379, and 0.312, respectively. Thus, the modification of the flow by the roughness elements is sufficiently strong in the 4Bumps case, despite the small bump height and the gentle slope of the bump, to significantly decrease Ri_b. The decrease in Ri_b suggests that the buoyancy effect in the 4Bump case on turbulence is weaker, as will be demonstrated by quantification of turbulent fluxes.

The vertical profile of local gradient Richardson number, Ri_g defined by Eq. (3.4), is a measure of the strength of static stability relative to shear instability, and is depicted in figure 3.8.

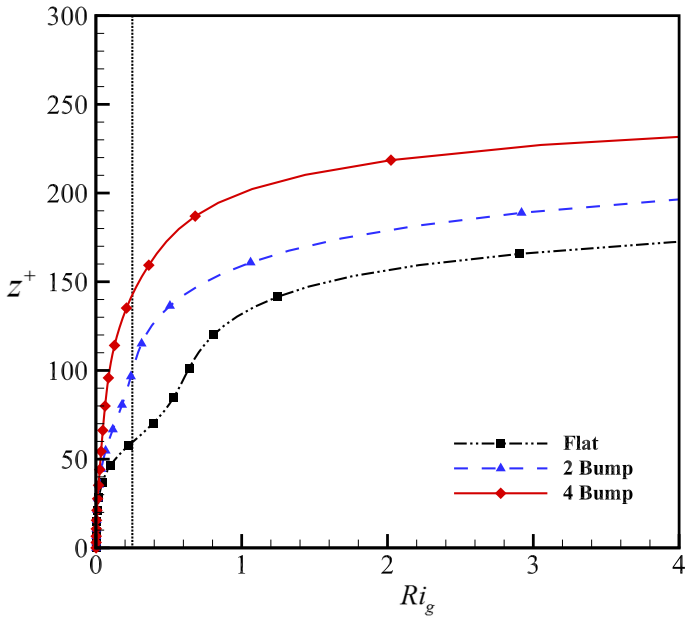

Figure 3.8: Profiles of gradient Richardson number for flat: -□-, 2-bump: -△-, 4-bump: —◇— in the stratified cases. The statistics are averaged during one inertial time $ft \approx 2\pi$.

In the near-surface region, Ri_g decreases substantially with increasing number of bumps. Thus, the behavior of both Ri_b and $Ri_g(z)$ suggest that the chosen roughness elements relax the stabilizing effect of buoyancy. The vertical location where Ri_g crosses the critical value of 0.25 increases with the number of bumps so that the subcritical ($Ri_g < 0.25$) region of the Ri_g profile expands significantly. The subcritical region that starts at the bottom reaches up to $z^- \approx 0.2$ in the 4-bump case instead of $z^- \approx 0.075$ in the flat case. The implication is that roughness changes the stability of the near-bottom flow to make it more vulnerable to shear instability.

The contour of local gradient Richardson number, Ri_g defined by Eq. (3.4), is a measure of the height-dependent strength of static stability relative to shear instability, and is depicted in figure 3.9. There is a region extending up from the wall which is subcritical ($Ri_g < 0.25$). The height at which Ri_g crosses the critical value of 0.25 increases with the number of bumps so that the subcritical region of the Ri_g profile expands significantly. The subcritical region that

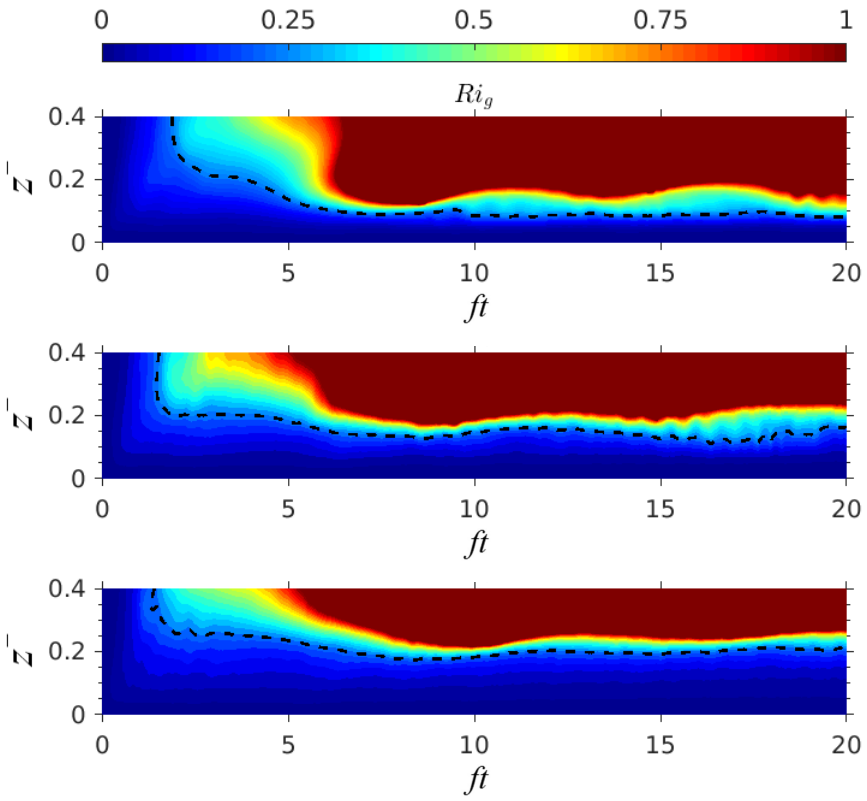

Figure 3.9: Contours of gradient Richardson number (Ri_g) for Flat (top), 2Bump (middle) and 4Bump (bottom) cases. The black dashed line shows $Ri_g = 0.25$.

starts at the bottom reaches up to $z^- \approx 0.2$ in the 4Bump case instead of $z^- \approx 0.075$ in the Flat case. The implication is that roughness changes the stability of the near-bottom flow to make it more vulnerable to shear instability. Thus, the behavior of both Ri_b and $Ri_g(z)$ suggest that the roughness elements, albeit small, substantially mitigate the stabilizing effect of buoyancy.

In figure 3.10 instantaneous vertical vorticity contours for the three stratified cases at different times ($ft \approx \pi$ in the left column and $ft \approx 4\pi$ in the right column) are shown on a horizontal plane close to the wall ($z^+ \approx 16$) and near the crest of the bumps. These times correspond to points (a-f) on the TKE profiles shown in the left column of figure 3.7 and also to panels (a-f) in figure 3.10. Comparison of the points demarcated as b, d and f on the time histories in figure 3.7 show that, at $ft \approx 4\pi$, the integrated TKE is the same for 2Bump and 4Bump cases and is slightly smaller in the Flat case. However, on comparison of figures 3.10 (b), (d) and (f), we find that the near-wall structures are substantially different, reinforcing the fact that an overall statistical measure of turbulence does *not necessarily* reveal the full picture of the flow state. In particular, with an increasing number of bumps, near-wall turbulence is less patchy and more continuous at $ft = 4\pi$, corresponding to a state of continuous turbulence without global intermittency (Nieuwstadt, 1984). This is true even at the earlier time of $ft = \pi$ during the initial adjustment of the boundary layer to buoyancy when the TKE drops.

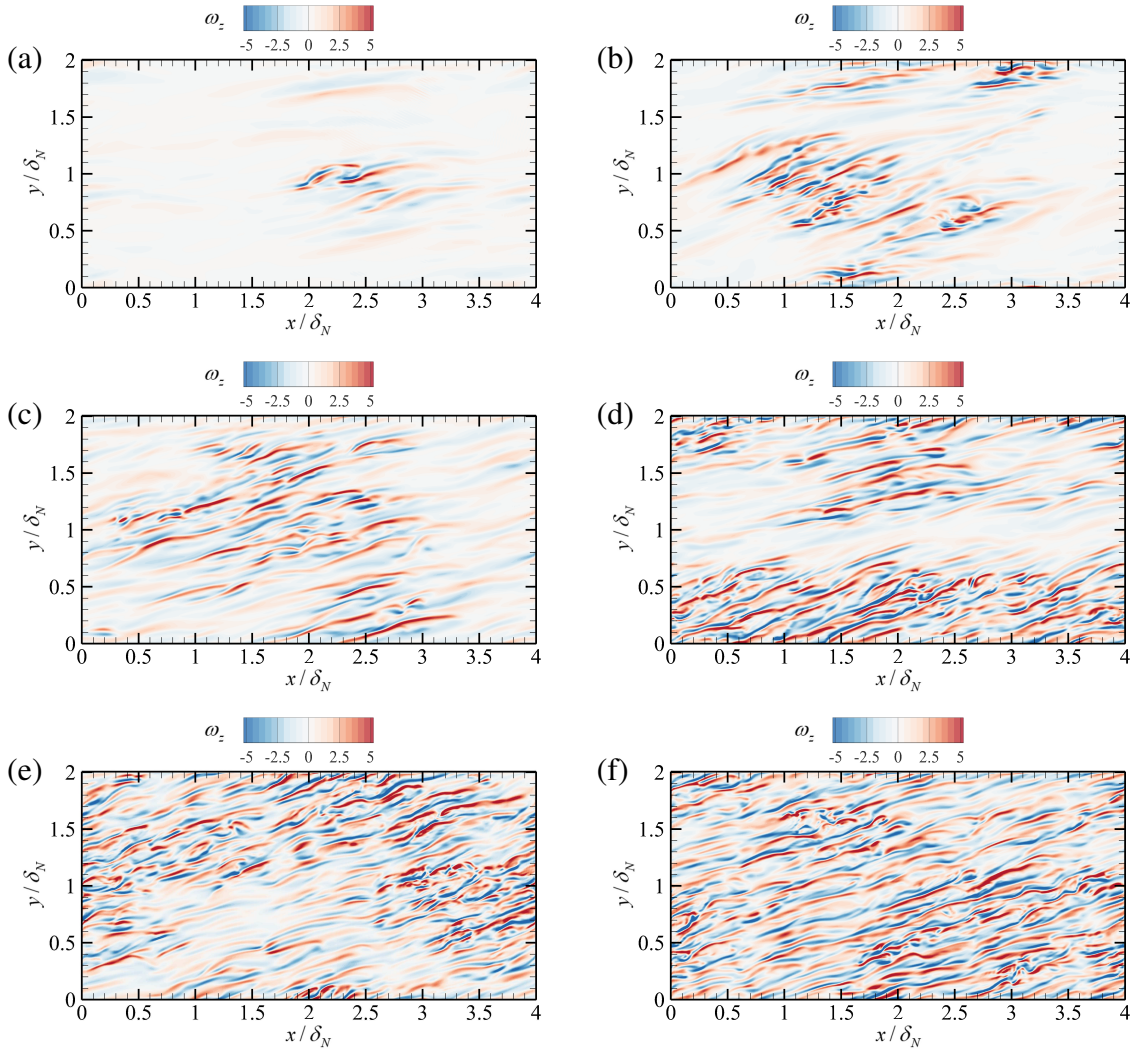

Figure 3.10: Vertical vorticity (normalized with u_{*N}/z) contour at $z^+ \approx 16$ in the stratified cases: (a,b) Flat, (c,d) 2Bump and (e,f) 4Bump. Left column at $ft \approx \pi$ and right column at $ft \approx 4\pi$.

3.2.2 Boundary layer thickness

Previous studies have chosen different metrics to quantify the thickness of the stratified boundary layers, including but not limited to the height of the capping inversion layer (Melgarejo and Deardorff, 1974; André and Mahrt, 1982), the height at which the low-level jet velocity is maximum (Blackadar, 1957; Shapiro and Fedorovich, 2010; Van de Wiel et al., 2010), and the height at which turbulent stress reduces to some fraction of its surface value (Zilitinkevich, 1972; Businger and Arya, 1975; André and Mahrt, 1982; Kosović and Curry, 2000). Although each of these definitions has a suitable use, the one defined based on the location where turbulent stress vanishes is chosen here as an average measure of the interface between turbulent and non-turbulent layers. We define the height by locating the position (denoted by z_p) where the horizontal Reynolds shear stress is reduced to 5 % of u_*^2, and then linearly extrapolating to the location at which it would vanish if the stress profile was linear. Thus, a time-evolving value of the stratified boundary layer thickness is defined as

$$\delta_t = \frac{z_p}{0.95} \quad ; \quad \text{at } z = z_p,\ \sqrt{\langle u'w' \rangle^2 + \langle v'w' \rangle^2}/u_*^2 = 0.05\,. \tag{3.14}$$

Subsequently, a modified bulk Richardson number, based on the local (in time) boundary-layer thickness, is defined as

$$Ri_{b,t} = \beta g \delta_t \frac{\langle \Delta\theta_0 \rangle}{U_\infty^2}\,. \tag{3.15}$$

Figure 3.11 (a) shows the time evolution of δ_t for the stratified cases. In the Flat case, the EBL thickness decreases sharply during the initial collapse of turbulence. Although small relative to the initial neutral boundary layer height, the reach of the roughness bumps becomes comparable to the reduced value of δ_t during turbulence collapse. Therefore, the roughness elements are able to sufficiently perturb the thin, collapsing boundary layer to partially arrest turbulence collapse. The modified bulk Richardson number ($Ri_{b,t}$) is shown in figure 3.11 (b). The previously shown Ri_b, based on the neutral boundary-layer scale (δ_N), is also shown for ease

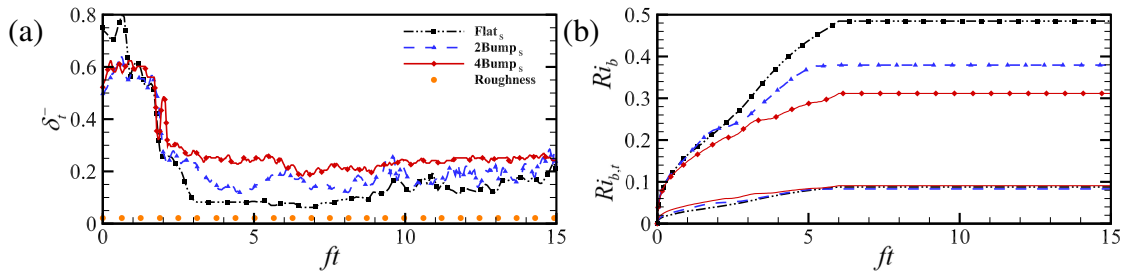

Figure 3.11: Time evolution of bulk quantities is contrasted among the different rough stratified cases: (a) local (in time) boundary-layer thickness and (b) bulk Richardson number (Ri_b) for Flat - ■ - , 2Bump - ▲ - , and 4Bump —◆— , and modified bulk Richardson number ($Ri_{b,t}$) for Flat - · - · - , 2Bump - - - - , and 4Bump —— . The roughness element height is also shown in (a).

of comparison. For the 4Bump case, the non-steady values of $Ri_{b,t}$ are initially higher when the flow goes through turbulence collapse, however the final values are similar. Thus, the *overall* strength of stratification as measured by $Ri_{b,t}$ does not change among cases. It is the wall-normal distribution of temperature and velocity which is affected by roughness. The invariance of $Ri_{b,t}$ among cases implies that $\delta_t \propto \langle \Delta\theta_0 \rangle^{-1}$. Evidently, the introduction of surface bumps decreases the net amount of surface cooling (shown by the decrease of Ri_b) and, concurrently, increases the boundary-layer thickness to maintain $Ri_{b,t}$. It is worth noting that, in previous DNS of the stable flat-bottom case with constant temperature boundary condition that imposes Ri_b, the vertical extent of the Reynolds shear stress profiles also exhibits a similar trend of δ_t increasing with decreasing Ri_b. For example, it can be inferred from figure 13(c) of Shah and Bou-Zeid (2014), which shows the Reynolds shear stress for various stability levels, that δ_t is approximately inversely proportional to Ri_b.

3.2.3 Turbulent fluxes

Roughness enhances turbulent fluxes and, furthermore, the increase is substantially stronger in the stratified situation relative to its unstratified counterpart. Figure 3.12 (a,b) shows profiles of the turbulent momentum flux ($\sqrt{\langle u'w' \rangle^2 + \langle v'w' \rangle^2}/u_{*N}^2$), which are obtained by hori-

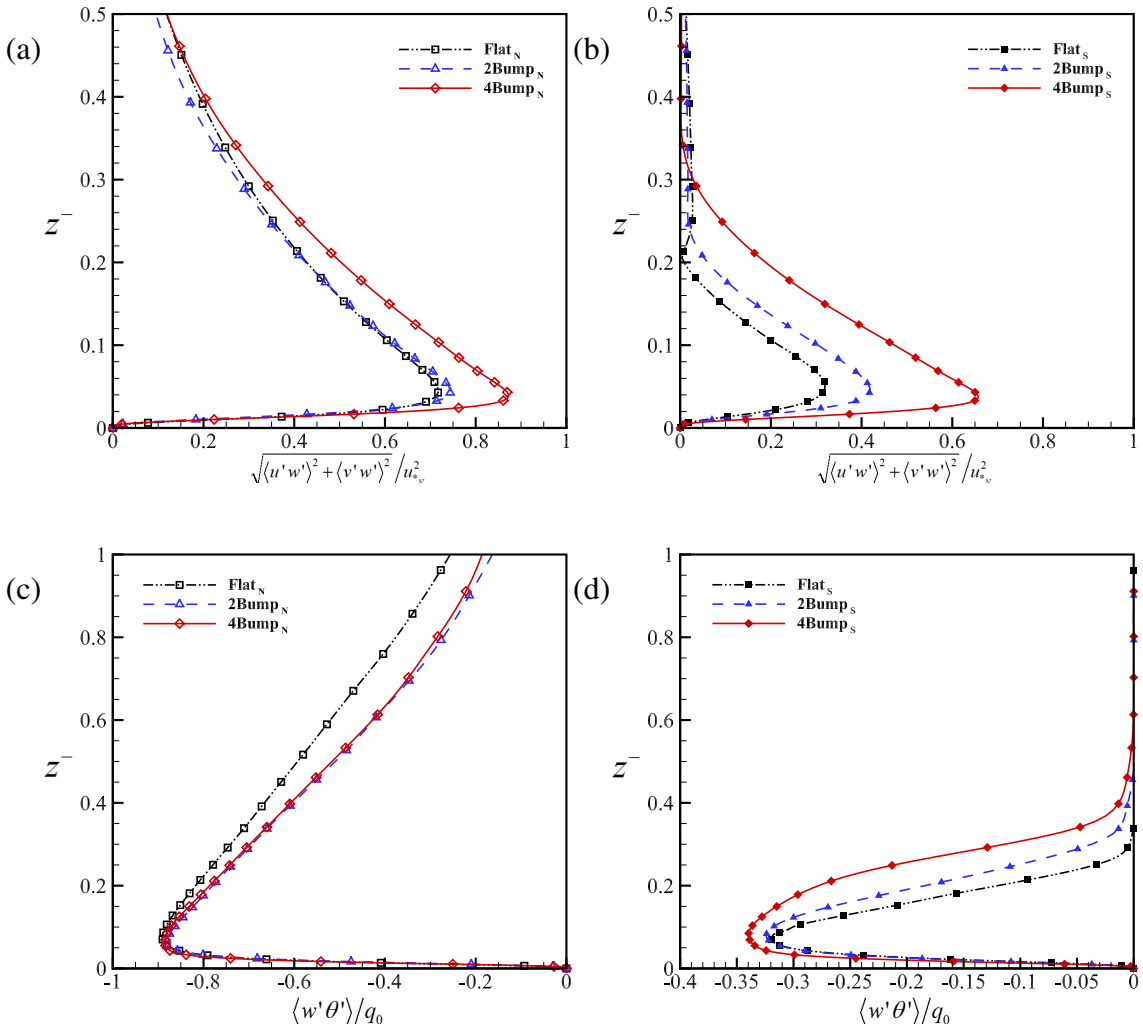

Figure 3.12: The effect of surface bumps on turbulent fluxes: (a,b) turbulent momentum flux ($\sqrt{\langle u'w'\rangle^2+\langle v'w'\rangle^2}/u_{*N}^2$) profiles and (c,d) buoyancy flux ($\langle w'\theta'\rangle)/q_0$) profiles. Neutral situation shown in (a,c), and stratified counterpart in (b,d).

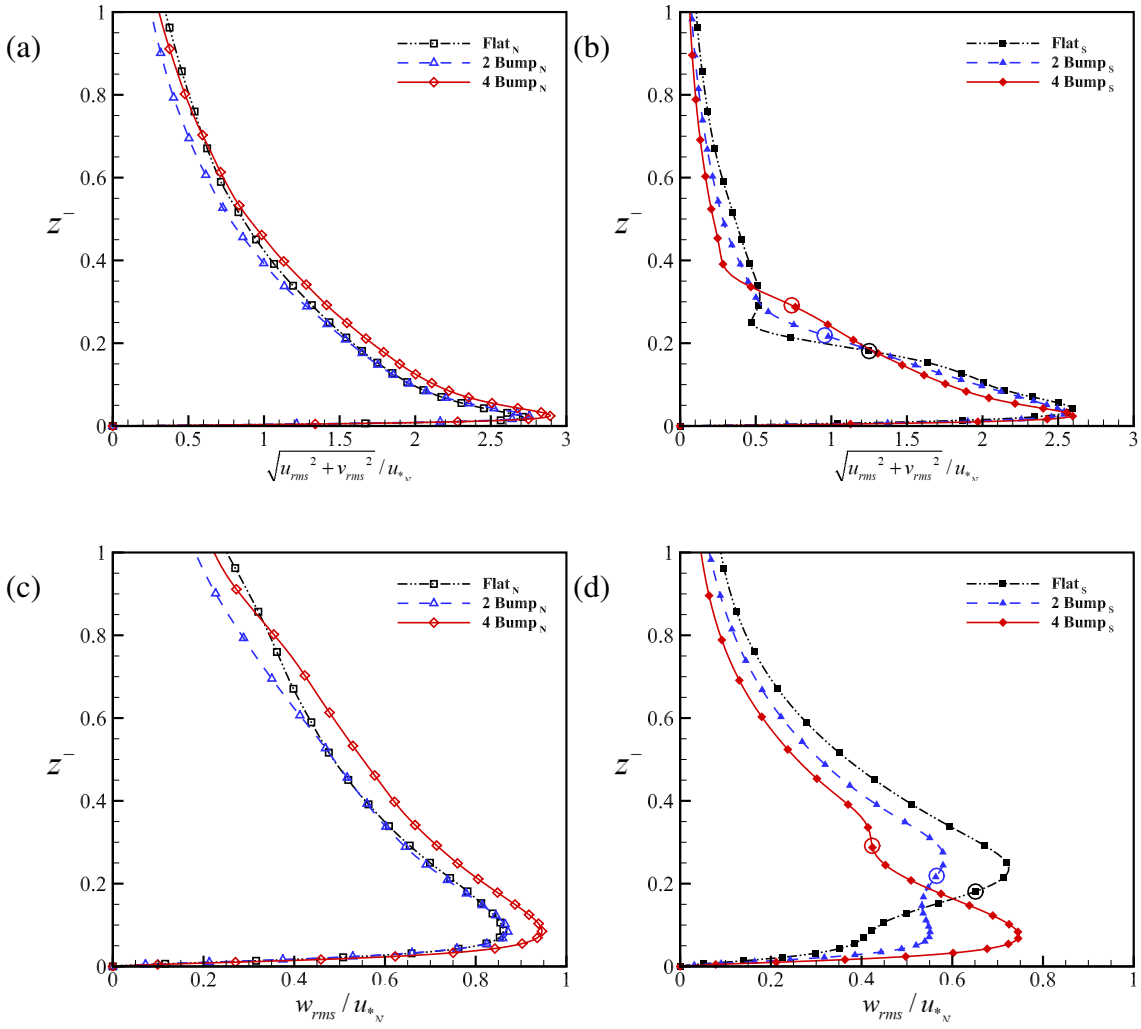

Figure 3.13: Profiles of velocity fluctuations contrasted between neutral (a,c) and stratified (b,d) conditions: (a,b) horizontal velocity fluctuations ($\sqrt{u_{rms}^2 + v_{rms}^2}$) and (c,d) vertical velocity fluctuations (w_{rms}). Open circle (right column) profile shows $z = \delta_t$.

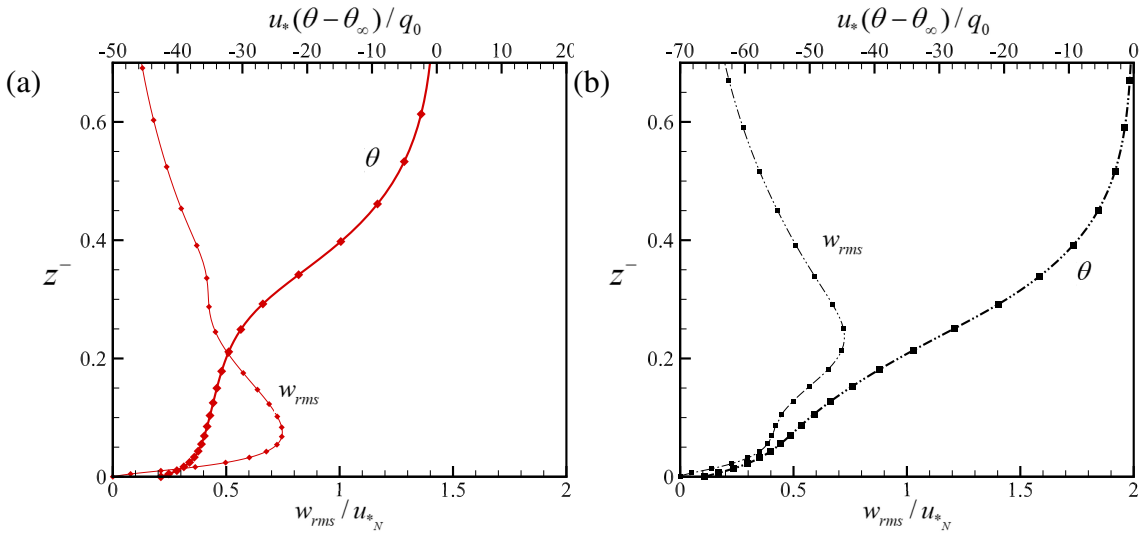

Figure 3.14: Comparison of rough and smooth-bottom cases in the context of Mahrt (1998) classification of the stable ABL. Potential temperature (θ) and vertical r.m.s. (w_{rms}) profiles: (a) 4Bump (—◆—) case, and (b) Flat (- -■- -) case. Normalization with u_{*N} and q_0.

zontal x-y averaging and a time average over $ft \approx 2\pi$. In the neutral EBL (figure 3.12(a)), the increase with respect to the flat case is negligible for the 2Bump case and moderate for the 4Bump case. The increase is substantially more in the stratified cases (figure 3.12(b)), e.g. the peak value in the 4Bump case is twice that in the flat case. Surface cooling suppresses the turbulent momentum flux as revealed by comparison of figure 3.12(a) with (b). However, surface roughness is able to counteract the suppression over a significant portion of the initial neutral boundary layer. The flux profiles in the stratified rough cases have a larger vertical extent than the stratified Flat case, consistent with the increase of the boundary-layer thickness (δ_t) induced by the bumps.

Buoyancy flux, $\langle w'\theta' \rangle$, in the stratified cases (figure 3.12(d)) is considerably suppressed relative to the corresponding unstratified cases (figure 3.12(c)), regardless of the number of bumps. After its peak, the magnitude of $\langle w'\theta' \rangle$ drops sharply with increasing height relative to the unstratified cases. The drop is less sharp in the presence of roughness. Thus, between z^- of 0.15 and 0.3 in figure 3.12(d), the value of $\langle w'\theta' \rangle$ is substantially larger in the 4Bump case (filled red diamonds) relative to the Flat case (filled black squares).

Roughness preferentially enhances vertical fluctuations in the stratified EBL. Figure 3.13

depicts the effect of roughness on the amplitude of horizontal ($u_{h,rms} = \sqrt{u_{rms}^2 + v_{rms}^2}$) and vertical ($w_{rms} = \sqrt{\langle w'w' \rangle}$) fluctuations. The presence of surface roughness leads to a mild increase of both $u_{h,rms}$ and w_{rms} above the bumps in the neutral cases (left column). Under stratification, the surface roughness effect on w_{rms} is dramatic. In the near-surface region ($z^- < 0.15$) the 4Bump case has substantially larger w_{rms} relative to the Flat case, as seen in figure 3.13(d). This increase of vertical transport is key to the roughness-induced increase of TKE, as will be evident later in section 3.2.4 where the TKE budget is discussed. It is worth noting that the increase of near surface w_{rms} in the 4Bump stratified case is also manifested in the finding, illustrated by figure 3.10(f), that the 4Bump case has continuous near-surface turbulence in contrast to the local intermittency (localized turbulence patches distributed in an almost-quiescent background) of the Flat case in figure 3.10(b). The location of the EBL boundary ($z = \delta_t$), based on the turbulent momentum flux, is shown on each profile in figure 3.13. The r.m.s. fluctuation profiles have significantly larger vertical spread than δ_t which is based on the Reynolds shear stress.

Mahrt (1998), based on observational data, presents idealizations of the stratified boundary layer that we assess in figure 3.14 using the present simulation data. The very stable boundary layer (the right subfigure of figure 1 in Mahrt (1998)) is conceptualized by the author as follows: a w_{rms} profile that has weak near-surface values with the peak occurring at an elevated location, and a θ profile that exhibits a strong surface inversion layer. The Flat case (figure 3.14(b)) shows a strong near-surface inversion and an elevated peak of w_{rms} (associated with the shear of the LLJ), in good agreement with the idealization of a very stable boundary layer. On the other hand, the 4Bump stratified case (figure 3.14(a)) has a presentation that is more akin to the so-called weakly stable boundary layer (the left subfigure of figure 1 in Mahrt (1998)) that does not have an elevated peak of w_{rms} and has a weak surface inversion layer.

3.2.4 Turbulent kinetic energy budget

The TKE budget is analysed to better understand the mechanisms underlying turbulence collapse and rebirth. At statistical steady state, the Reynolds-averaged turbulent kinetic energy budget can be written as

$$\begin{aligned}\frac{\partial e}{\partial t} &= -\langle u_j\rangle\frac{\partial e}{\partial x_j} - \frac{1}{2}\frac{\partial\langle u_i' u_i' u_j'\rangle}{\partial x_j} - \frac{\partial\langle u_i' p'\rangle}{\partial x_i} + \delta_{i3}\beta g\langle u_i'\theta'\rangle \\ &\quad -\langle u_i' u_j'\rangle\frac{\partial\langle u_i\rangle}{\partial x_j} + \nu\frac{\partial^2 e}{\partial x_j^2} - \nu\left\langle\frac{\partial u_i'}{\partial x_j}\frac{\partial u_i'}{\partial x_j}\right\rangle,\end{aligned} \tag{3.16}$$

where turbulent kinetic energy $e = \frac{1}{2}\langle u_i' u_i'\rangle$, pressure transport rate $P_T = -\partial\langle u_i' p'\rangle/\partial x_i$, turbulent transport $T_T = -\frac{1}{2}\partial\langle u_i' u_i' u_j'\rangle/\partial x_j$, shear production rate $P = -\langle u_i' u_j'\rangle\partial\langle u_i\rangle/\partial x_j$, buoyancy flux $B = \delta_{i3}\beta g\langle u_i'\theta'\rangle$, viscous diffusion rate $\nu_D = \nu\partial^2 e/\partial x_j^2$ and viscous dissipation rate $\varepsilon = \nu\langle\partial u_i'/\partial x_j\,\partial u_i'/\partial x_j\rangle$. It is worth noting that the buoyancy flux (B) is negligible in comparison to the other terms in the TKE balance. The smallness of B in the stratified boundary-layer TKE budget is consistent with other studies of the EBL, e.g., Shah and Bou-Zeid (2014) and Gohari and Sarkar (2018), who find that B is negligible in the TKE balance and that the direct impact of stability on the flow is not through TKE destruction by buoyancy, but rather through the inhibition of shear production. The balance, calculated as the sum of all the terms on the right-hand side of Eq. (3.16), has been obtained as a function of time. In the 4Bump case the sum is less than 1% of the dominant term. In the flat and, to a lesser extent in the 2Bump case, the instantaneous sum is oscillatory owing to the inertial oscillations in TKE. The amplitude of these oscillations can be as large as 15% but the time average over an inertial period is again less than 1% of the dominant term.

Turbulent kinetic energy budget terms are shown in figure 3.15 for Flat (top row), 2Bump (middle row), and 4Bump (bottom row) cases at $ft = 0$ (left column), $ft \approx \pi$ (middle column)

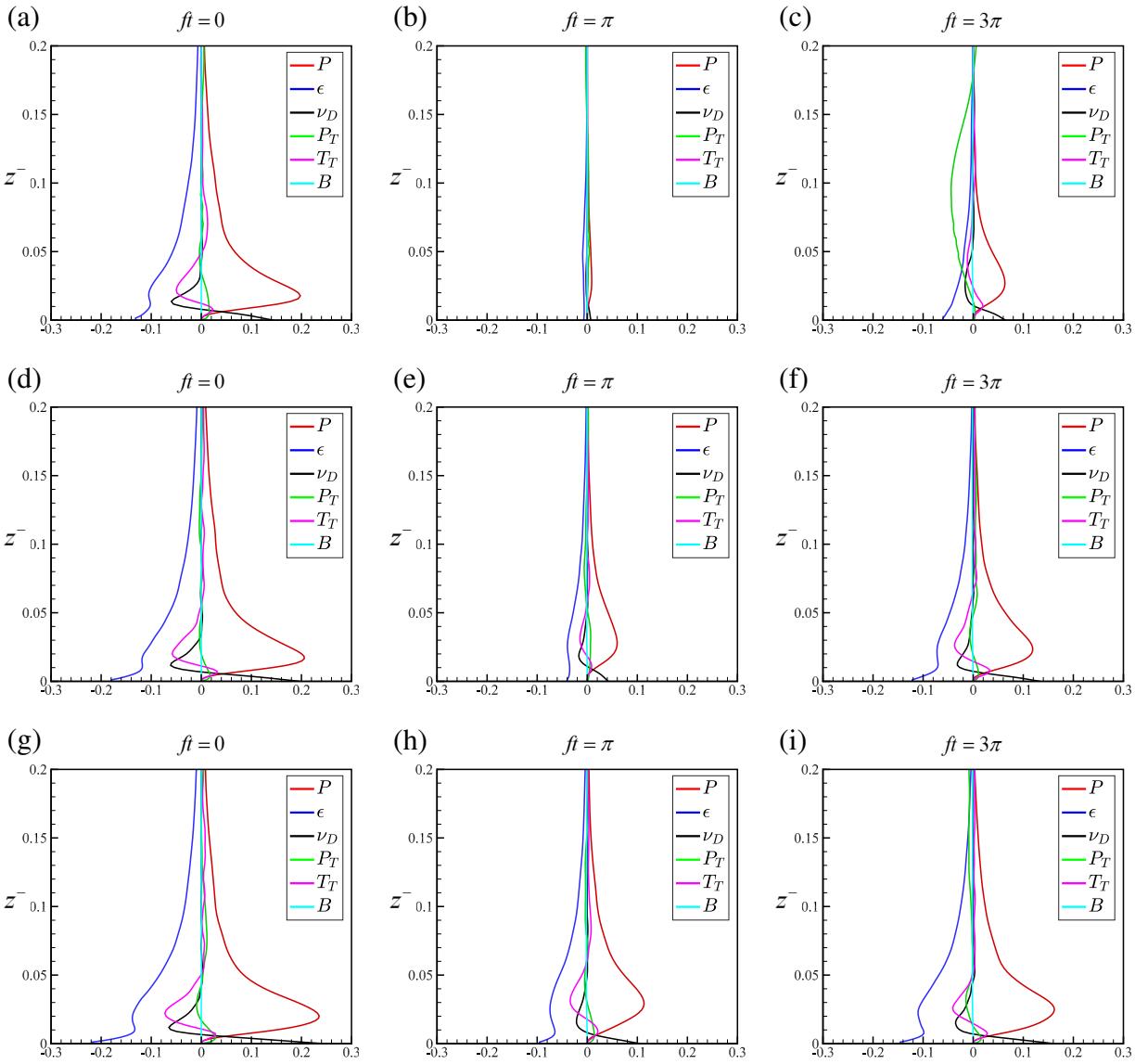

Figure 3.15: Turbulent kinetic energy budgets for Flat (a-c), 2Bump (d-f) and 4Bump (g-i) cases at different times: $ft = 0$ (left column), $ft \approx \pi$ (c,f,i) (middle) and $ft \approx 3\pi$ (right). Normalization with $u_{*_N}^4/\nu$.

during the initial turbulence collapse, and $ft \approx 3\pi$ (right column) after turbulence recovery. At $ft = 0$ which corresponds to the neutral EBL, the TKE budget terms are similar among the three cases. The peak of TKE production (P) is in the buffer layer. After the imposition of constant-flux stability, there is a drop of P. For the Flat case (figure 3.15(b)), P becomes negligible at $ft \approx \pi$. The restriction of TKE production in the surface layer by the imposed stable surface cooling flux leads to turbulence collapse (Ansorge and Mellado, 2014; Shah and Bou-Zeid, 2014). In the Flat case, Gohari and Sarkar (2017) showed that turbulence recovery is promoted by pressure transport (P_T) that carries outer-layer fluctuation energy into the lower flank (with subcritical Ri_g) of the near-surface LLJ. The pressure transport is important during the recovery in the Flat case (green line in figure 3.15(c)), but not so in the cases with roughness (figure 3.15(f) and (i)). For the 2Bump case in figure 3.15(e), the magnitude of the shear production is reduced, but nevertheless, roughness ensures that $|P| > 0$. The production of mechanical turbulence enhances the subsequent recovery of the EBL to a turbulent state. For the 4Bump case in figure 3.15(h), the reduction of shear production by buoyancy is even weaker than the 2Bump case. It is evident from figure 3.15 that the surface roughness aids TKE generation to keep the flow from turbulence collapse. For the same reason, near-surface turbulence is continuous in the 4Bump case after recovery rather than being locally intermittent as in the Flat case. The reduction of P by buoyancy is related to the significant damping of vertical turbulent motions which in turn reduces the momentum fluxes ($\langle u'w' \rangle$ and $\langle v'w' \rangle$), especially in the Flat case, as seen by comparing figure 3.12(b) with figure 3.12(a). This reduction is mitigated in the rough cases because the surface bumps promote vertical transport.

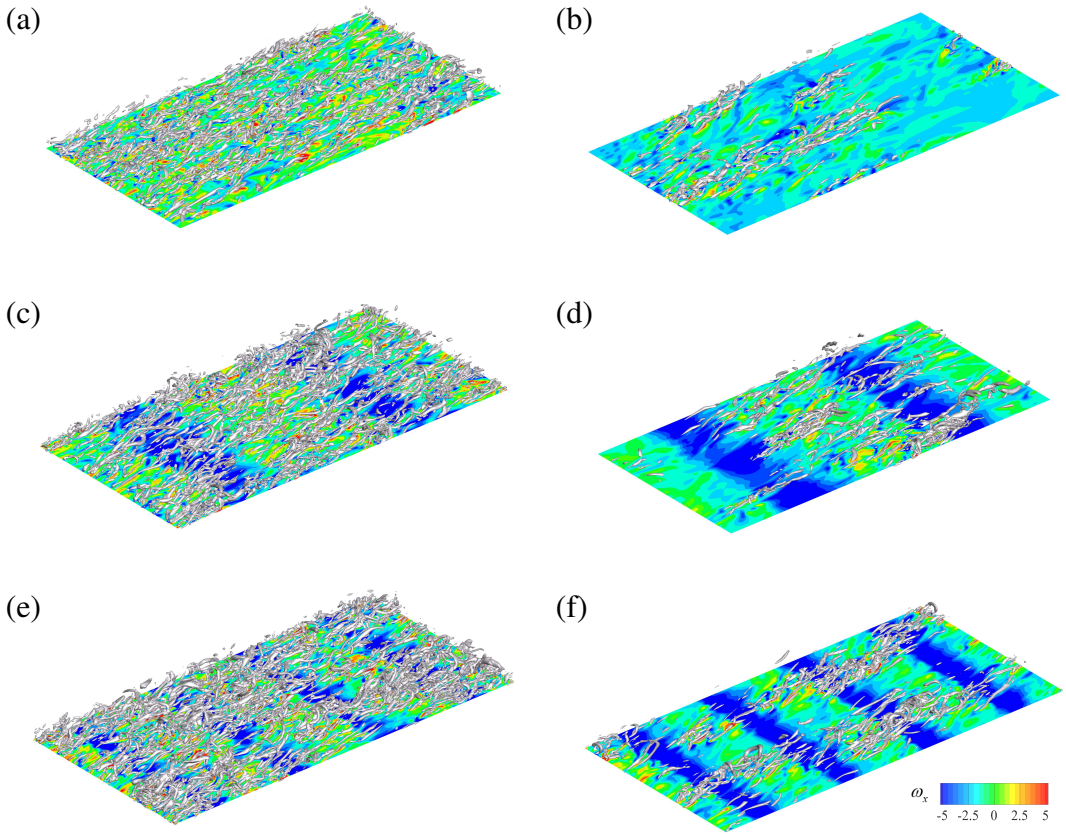

Figure 3.16: Coherent structures deduced by a λ_2 isosurface are superposed on streamwise vorticity on a horizontal plane at $z^+ \approx 16$ (at the crest of the bumps) and contrasted between neutral (left column) and stratified (right column) cases. (a,c,e) are the neutral Flat, 2Bump and 4Bump cases, respectively, while (b,d,f) are the corresponding stratified cases. The snapshots are taken at $ft \approx 6$ when the TKE is approximately at its minimum. Vorticity is normalized with u_{*N}/z. Isosurface of $\lambda_2 = -3.125(u_{*N}/z)^2$ is shown.

3.3 Flow structures

3.3.1 Coherent structures

The roughness elements introduce coherence into the flow vorticity and velocity. Figure 3.16 shows a λ_2 isosurface superposed on the streamwise vorticity (ω_x) contour on a near-surface horizontal plane. The quantity, λ_2, is the intermediate eigenvalue of the symmetric tensor, $S_{ik}S_{kj} + \Omega_{ik}\Omega_{kj}$, where S_{ij} and Ω_{ij} are the symmetric and antisymmetric components of the velocity gradient tensor, $\partial u_i/\partial x_j$. The unstratified flow (left column) exhibits coherent packets of hairpin vortices. The near-wall structures are inclined with a veering angle with respect to the outer geostrophic velocity which points in the x-direction. The signature of the bumps is seen in the coherent strips of ω_x on the displayed horizontal plane. The snapshots are shown at $ft \approx 6$ when the TKE in the stratified cases is approximately at its minimum. At this time, the coherent structures in the stratified EBL (right column of figure 3.16) are suppressed relative to neutral conditions. Nevertheless, the roughness elements are able to sustain some of the unsteady flow structures as can be seen by comparing the 4Bump case (figure 3.16(f)) with the Flat case (figure 3.16(b)).

3.3.2 Dispersive effects of roughness

The roughness elements introduces a variability in the flow relative to the horizontal average. This variability leads to a so-called dispersive component of velocity which brings about fluxes of momentum and heat, and is extracted as follows. First, the field variables are decomposed into a time-averaged mean and a fluctuating component. Thus, the velocity on a given horizontal plane (fixed z) is split into

$$u_i(x,y,t) \;=\; \bar{u}_i(x,y) + u_i''(x,y,t)\,, \tag{3.17}$$

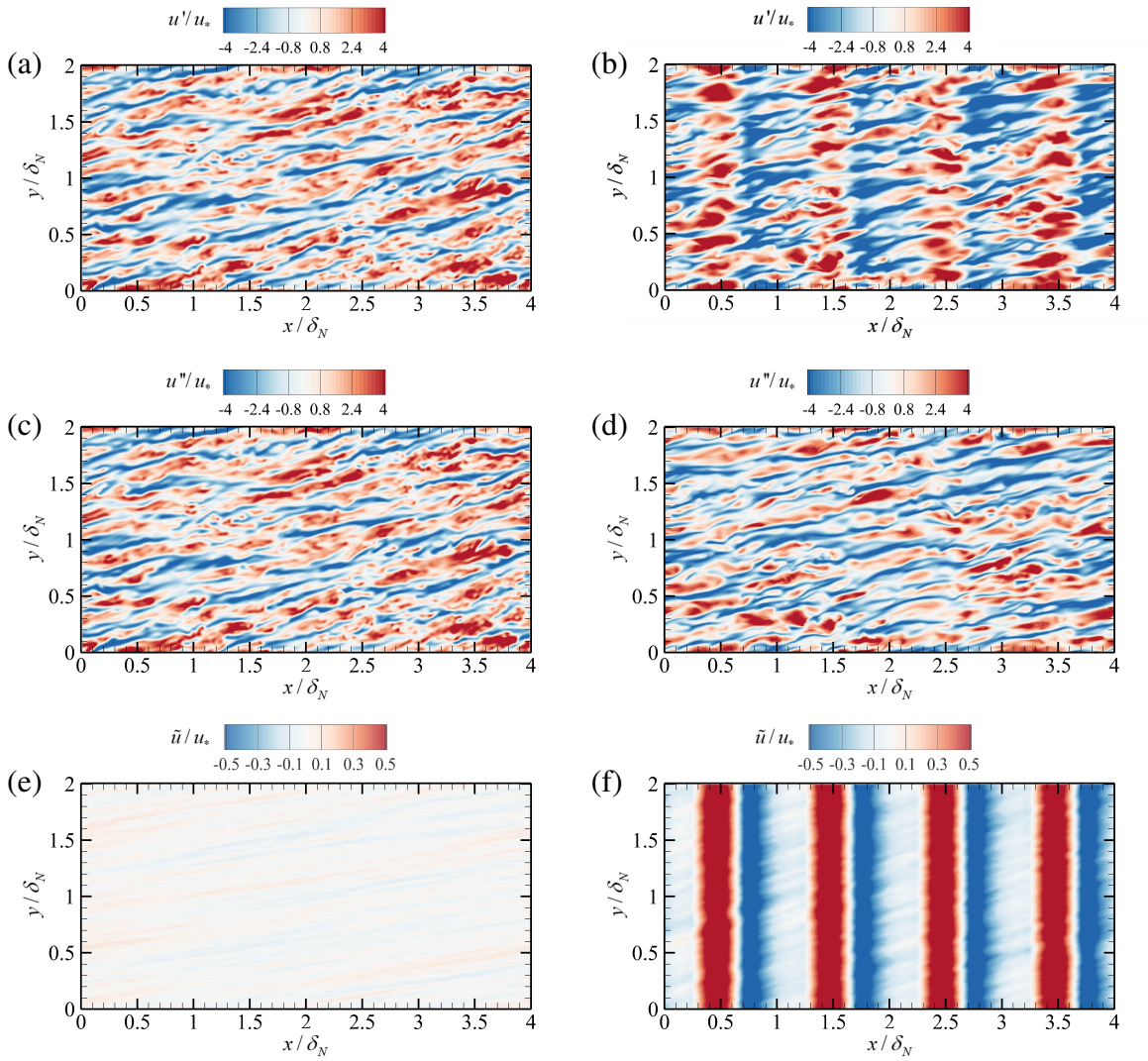

Figure 3.17: A triple decomposition of the velocity in the neutral EBL, shown at $z^+ \approx 16$, the crest of the roughness bumps: (a,b) Reynolds fluctuations (u'/u_*), (c,d) incoherent velocity fluctuations (u''/u_*) and (e,f) coherent components ($\tilde{u}/u_*$). Left column (a,c,e) corresponds to Flat and right column (b,d,f) to 4Bump. The neutral value (u_{*N}) of wall stress is used for normalization in this and subsequent figures with components from the triple decomposition.

where $\bar{u}_i$ is the time-averaged mean and $u_i^{''}$ is the fluctuation about the time-averaged mean. The two dimensional (2-D) periodic roughness in the present problem imposes a spatial organization on the time-averaged field that can be extracted by applying a further streamwise spatial average, denoted by $\langle\rangle_x$, to the time average ($\bar{u}_i$). Thus, Eq. (3.17) becomes

$$\begin{aligned} u_i(x,y,t) &= \langle\bar{u}_i\rangle_x(y) + \tilde{u}_i(x,y) + u_i^{''}(x,y,t) \\ &= \langle\bar{u}_i\rangle_x(y) + u_i^{'}(x,y,t)\,. \end{aligned} \tag{3.18}$$

This decomposition identifies $\tilde{u}_i(x,y)$ as the spatially coherent part of the time-averaged flow, e.g. Finnigan (2000); Sullivan et al. (2000); Poggi et al. (2004); Li and Bou-Zeid (2019). Physically, $\tilde{u}_i(x,y)$ in the present problem is the time-mean velocity associated with the roughness bumps. Because of the streamwise periodicity and statistical steadiness, the composite (t and x) average, $\langle\bar{u}_i\rangle_x(y)$, is taken to be the Reynolds average and the fluctuation, $u_i^{'}$, is the Reynolds fluctuation. As elaborated in this section, the $u_i^{'}$ field contains a time-independent part ($\tilde{u}_i(x,y)$) associated with the 2-D roughness elements which leads to a dispersive component of the Reynolds stress and an 'incoherent' part ($u_i^{''}(x,y,t)$). The triple decomposition (Reynolds and Hussain, 1972) splits the velocity into a time-average, a time-coherent (often a wave-like field at a specific temporal frequency) component, and an incoherent turbulent component. The first line of Eq. (3.18) is analogous to their triple decomposition as it extracts the space-coherent component introduced by the periodic roughness.

For completeness, the mathematical definition of the averages and the fluctuations are given below for the velocity on a horizontal plane at constant z:

$$\bar{u}_i(x,y) = \frac{1}{T}\int_t^{t+T} u_i(x,y,t')dt'\,, \tag{3.19}$$

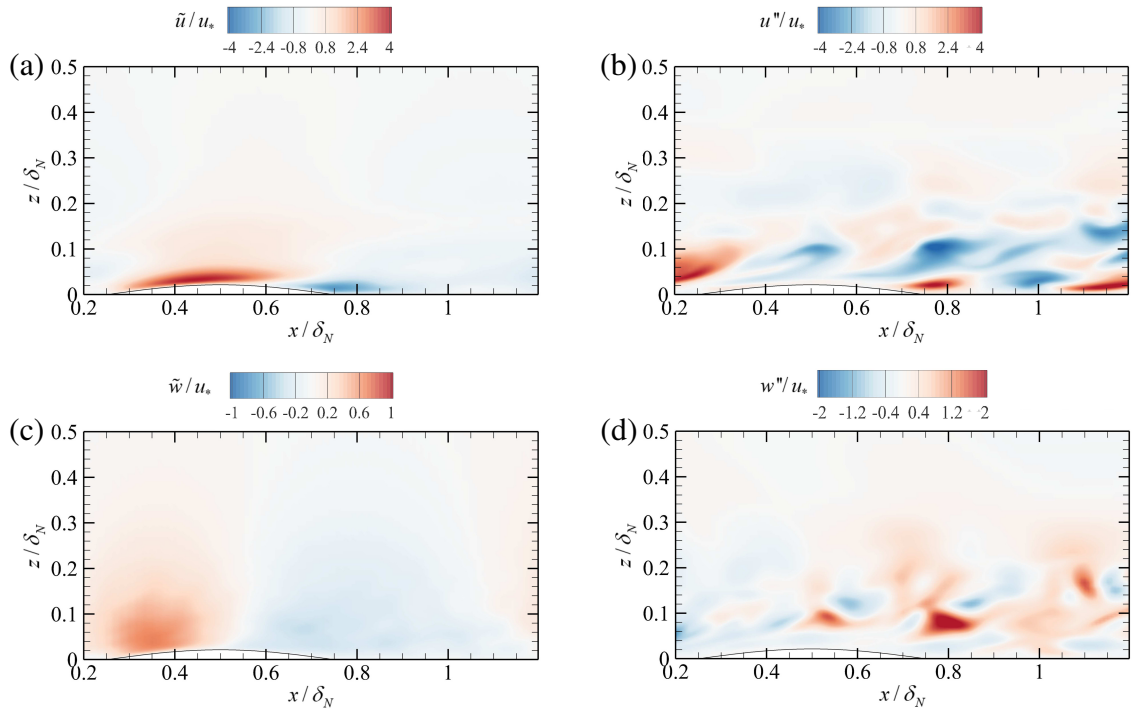

Figure 3.18: Vertical-plane snapshot of instantaneous velocity in the 4Bump unstratified case after the flow has reached a quasi-steady state: (a) $\tilde{u}/u_*$, (b) u''/u_*, (c) $\tilde{w}/u_*$, and (d) w''/u_*. Flow is shown in the vicinity of a single bump.

$$\langle u_i \rangle_x(y,t) = \frac{1}{L_x}\int_0^{L_x} u_i(x,y,t)dx\,, \tag{3.20}$$

$$\tilde{u}_i(x,y) = \bar{u}_i(x,y) - \langle \bar{u}_i \rangle_x(y)\,, \tag{3.21}$$

$$u_i^{'}(x,y,t) = u_i(x,y,t) - \langle \bar{u}_i \rangle_x(y)\,, \tag{3.22}$$

$$u_i^{''}(x,y,t) = u_i(x,y,t) - \bar{u}_i(x,y)\,. \tag{3.23}$$

Figure 3.17 shows the consequences of the decomposition of streamwise velocity (u) in the neutral EBL. The neutral value (u_{*N}) of friction velocity is used to normalize velocity in figures 3.17-3.21. Upon comparison of figure 3.17(a) and (c), it is evident that the Reynolds fluctuations ($u^{'}$) and the incoherent velocity fluctuations ($u^{''}$) are similar in the unstratified Flat case and $\tilde{u} = 0$. However, in the 4Bump case, the $u^{'}$ field (figure 3.17(b)) is different from the incoherent $u^{''}$ field (figure 3.17(d)). The $u^{'}$ field contains a spatially organized component,

which is introduced by the bumps. This coherent component ($\tilde{u}_i$), isolated by applying the triple decomposition, appears as four distinctive strips associated with the four surface bumps in figure 3.17(f). The region of positive u which is forward of a surface bump combines with the rearward negative u to form a strip associated with the roughness. The imprint of the 2-D bumps, extracted through $\tilde{u}$, is unequivocal.

The influence of the bumps extends upward from the roughness elements into the flow as illustrated by figure 3.18. The vertical coherent component ($\tilde{w}$ in figure 3.18(c)) takes values of $O(u_*)$ up to $z^- = 0.1$ which is about 3 times the roughness height. When the boundary-layer thickness (δ_t) decreases during the initial transient as the EBL adjusts to the imposed cooling flux, the vertical reach of the bump-induced flow is no longer small compared to δ_t. For example, during the initial turbulence collapse in the Flat case, the boundary layer thins to $\delta_t^- \approx 0.1$ (Figure 3.11 (a)). The vertical extent of the roughness-induced perturbation to the flow is sufficient to mitigate the turbulence collapse and δ_t^- does not become smaller than 0.2 in the 4Bump case.

The dispersive effect of the roughness is an important contributor to the Reynolds shear stress as is demonstrated by figure 3.19 . Let $M = \sqrt{\langle u'w'\rangle^2 + \langle v'w'\rangle^2}$ denote the turbulent momentum flux obtained after Reynolds averaging. Since the Reynolds fluctuation can be decomposed as $u' = \tilde{u} + u''$, it follows that

$$M = M_{coh} + M_{inc} + M_{cross}, \tag{3.24}$$

where the coherent (M_{coh}) and incoherent (M_{inc}) components are given by

$$M_{coh} = \sqrt{\langle \tilde{u}\tilde{w}\rangle^2 + \langle \tilde{v}\tilde{w}\rangle^2}, \quad M_{inc} = \sqrt{\langle u''w''\rangle^2 + \langle v''w''\rangle^2}, \tag{3.25}$$

and the cross-term is

$$M_{cross} = \sqrt{\langle \tilde{u}w'' + u''\tilde{w}\rangle^2 + \langle \tilde{v}w'' + v''\tilde{w}\rangle^2}. \tag{3.26}$$

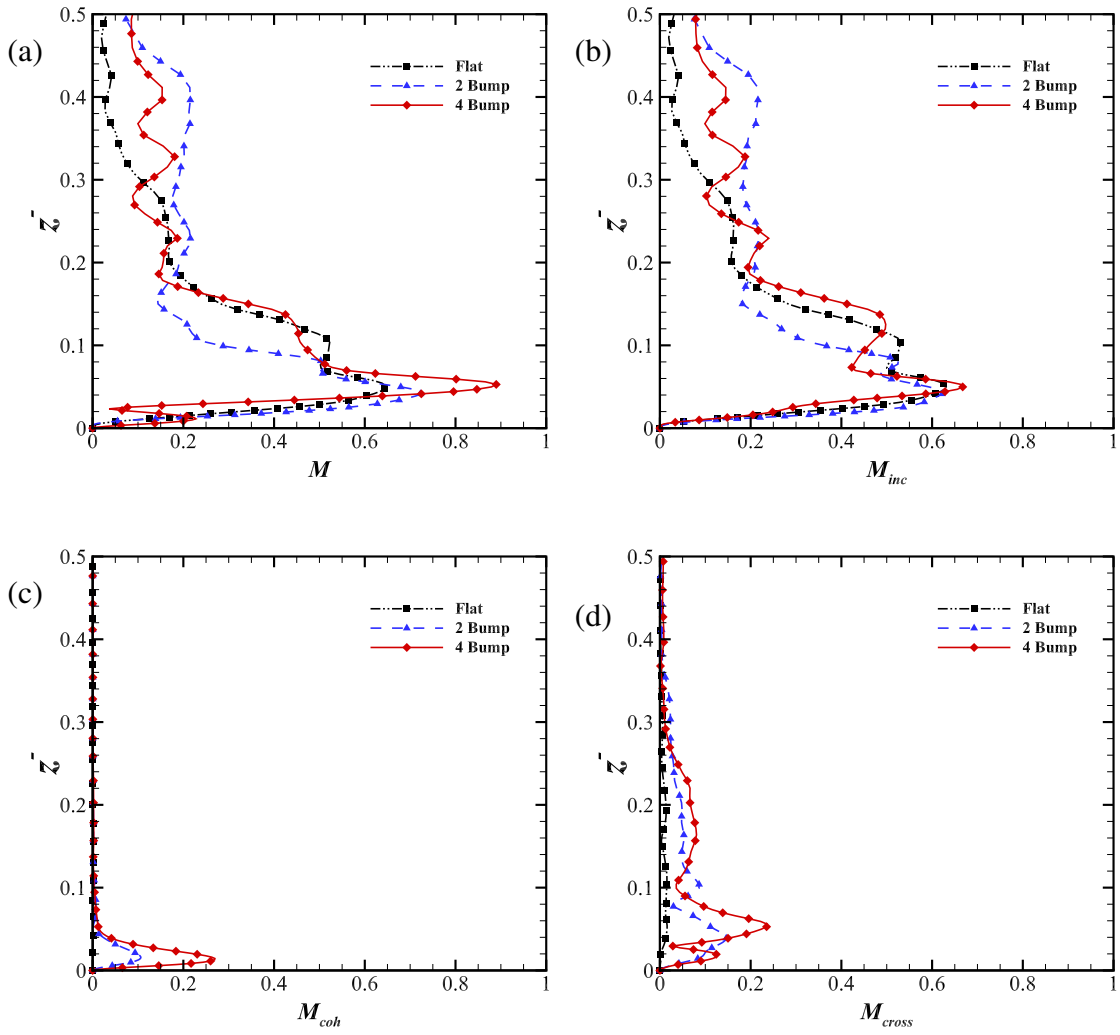

Figure 3.19: Decomposition of the turbulent momentum flux in the unstratified EBL: (a) $M = \sqrt{\langle u'w' \rangle^2 + \langle v'w' \rangle^2}$, (b) $M_{inc} = \sqrt{\langle u''w'' \rangle^2 + \langle v''w'' \rangle^2}$, (c)$M_{coh} = \sqrt{\langle \tilde{u}\tilde{w} \rangle^2 + \langle \tilde{v}\tilde{w} \rangle^2}$ and (d) $M_{cross} = \sqrt{\langle \tilde{u}w'' + u''\tilde{w} \rangle^2 + \langle \tilde{v}w'' + v''\tilde{w} \rangle^2}$.

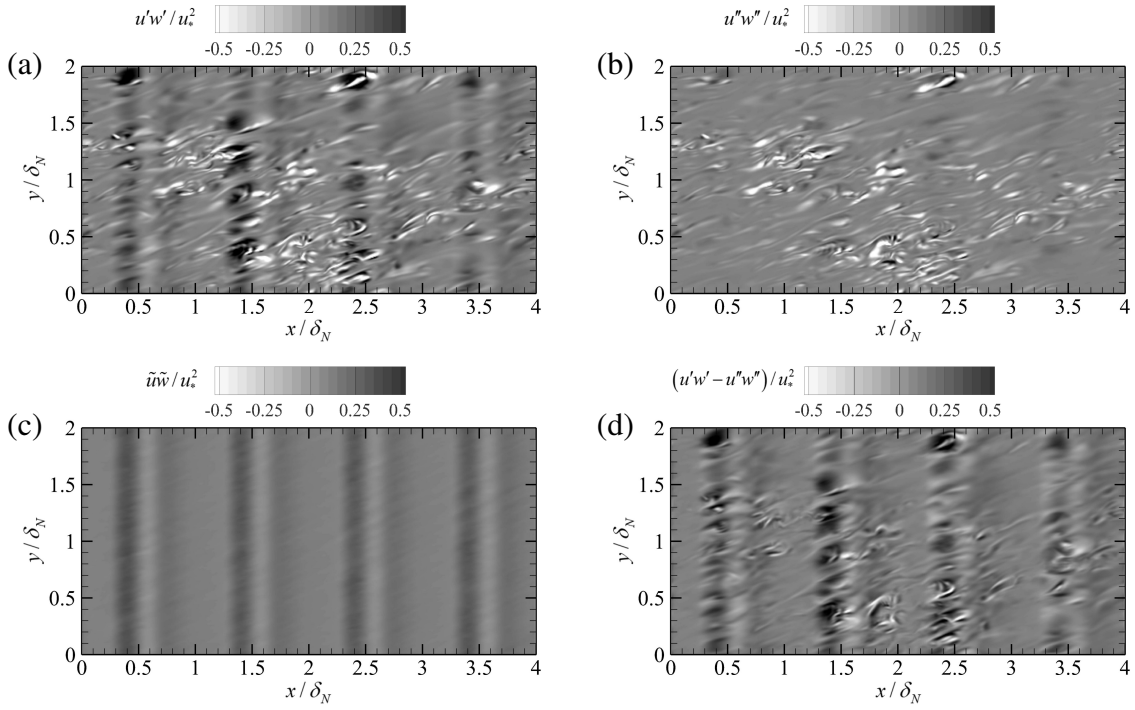

Figure 3.20: Instantaneous Reynolds shear stress and its components in the stratified 4Bump case at $ft \approx 3$ on horizontal plane at the crest of the bump ($z^+ \approx 16$): (a)$u'w'/{u_*}^2$, (b) $u''w''/{u_*}^2$, (c) $\tilde{u}\tilde{w}/{u_*}^2$, (d) $(u'w'-u''w'')/{u_*}^2$. The required time averages ($\bar{u}$ and $\bar{w}$) are computed using the evolution during $3 < ft < 6$. The neutral value (u_{*N}) of wall stress is used for normalization.

In figure 3.19(a), 4Bump has a higher peak value of M relative to the flat case. The incoherent part (figure 3.19(b)) has similar values for the peak, independent of surface roughness. The difference in M among cases arises from the coherent part (figure 3.19(c)) and also the cross-term (figure 3.19(d)). Both, coherent and cross-terms, are negligible in the Flat case, and their values in the surface layer increase with increasing number of bumps.

The preceding discussion shows that the presence of surface bumps substantially modifies the instantaneous velocity and the turbulent momentum fluxes by introducing a dispersive component. In the stratified cases the dispersive component remains substantial and, furthermore, its importance to the turbulence energetics is increased since the incoherent part is suppressed by buoyancy. The instantaneous Reynolds shear stress ($u'w'$) carries contributions from $(\tilde{u},\tilde{w})$ alone, (u'',w'') alone, and their cross-correlations, as illustrated for the 4Bump stratified case. The initial

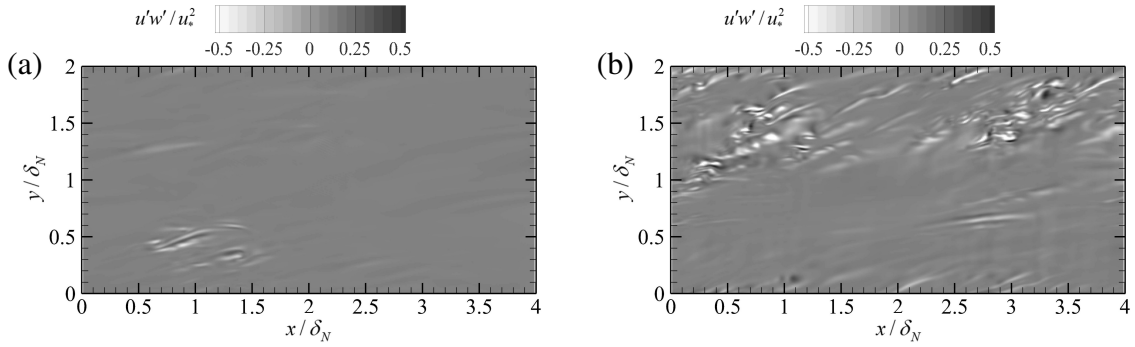

Figure 3.21: $u'w'/{u_*}^2$ on the horizontal plane, $z^+ \approx 16$, in the stratified Flat case: (a) $ft \approx 3$ during the initial transient, and (b) $ft \approx 17$ at late time. The neutral value (u_{*N}) of wall stress is used for normalization.

turbulence collapse ends when $ft \approx 3$ has elapsed after imposing the surface cooling flux. The instantaneous Reynolds shear stress ($u'w'$ in figure 3.20(a)) at $ft \approx 3$ shows the presence of the 2-D coherent bumps which is comingled with the incoherent fluctuation ($u''w''$ in figure 3.20(b)). The dispersive component ($u'w' - u''w''$ in Figure 3.20 (d)) is substantial.

In the stratified cases, roughness enhances the turbulent fluxes relative to the flat case by not only introducing coherent ($\tilde{u}\tilde{w}$) and dispersive ($u'w' - u''w''$) components into the shear stress but also by significantly changing the incoherent component ($u''w''$) relative to the flat case. Figure 3.21 shows the Reynolds shear stress (same as the incoherent component in the flat case) at early and late times in the flat, stratified case. Direct comparison of figure 3.20(b) with figure 3.21(a) shows that, at the early time of $ft \approx 3$, the 4Bump case has significant near-wall Reynolds shear stress in contrast to the negligible level in the Flat case. Later in time, $u'w'$ recovers somewhat in the Flat case (figure 3.21(b)) although it is spatially sparse relative to the rough case.

Iso-surface of λ_2 is depicted in 3.22 for the unstratified cases and in 3.23 for the stratified cases. The iso-surface is colored with magnitude of streamwise vorticity. It is clear from the visualization that the surface roughness in the form of bump in the present study is related to the number density of vortical structures. The number density, though not quantitatively measured,

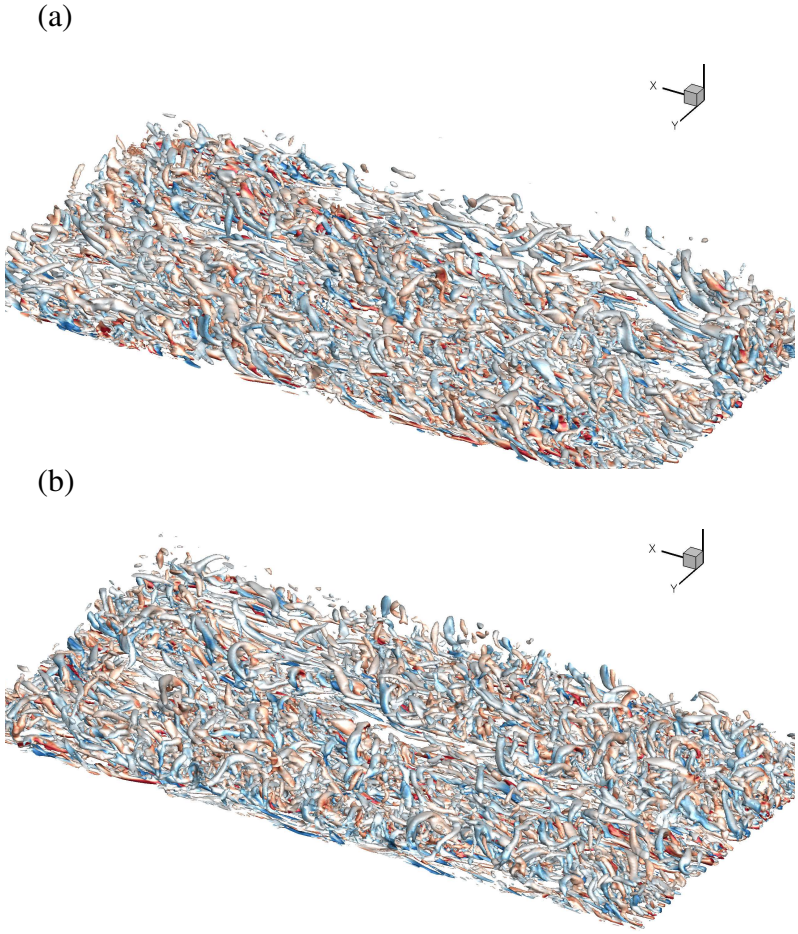

Figure 3.22: Isometric view of the vortical structures near the surface, iso-surface of $\lambda_2 = -3.125(u_{*N}/z)^2$ for unstratified case coloured with streamwise vorticity. (a) Flat case, (b) 4Bump case

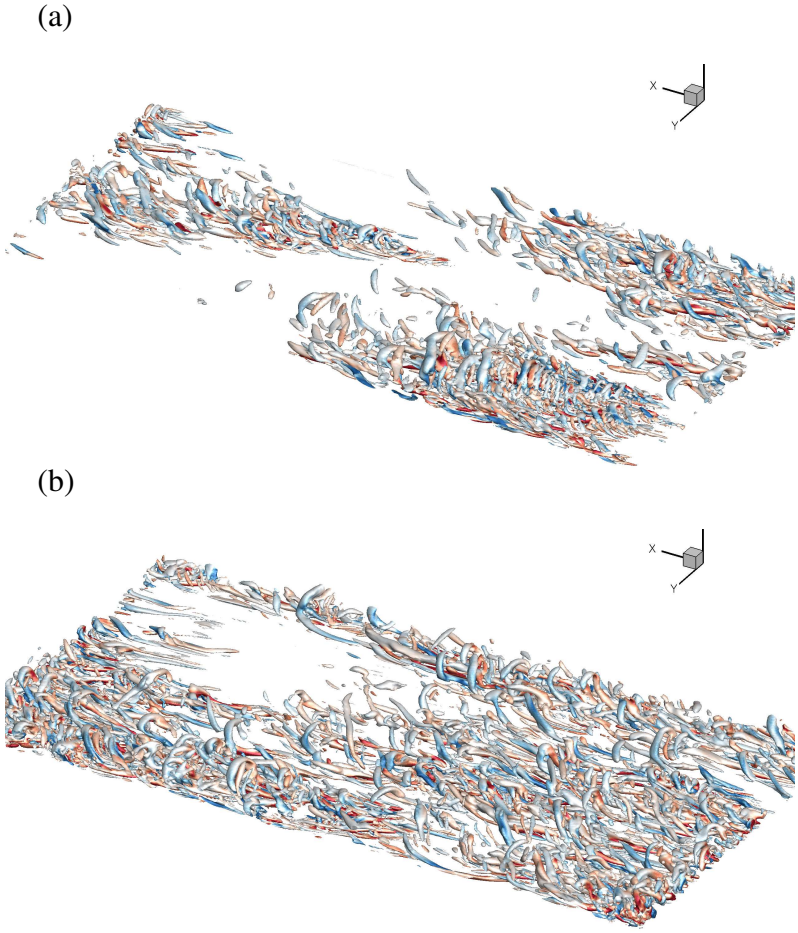

Figure 3.23: Isometric view of the vortical structures near the surface, iso-surface of $\lambda_2 = -3.125(u_{*N}/z)^2$ for stratified case colored with streamwise vorticity. (a) Flat case, (b) 4Bump case

is directionally proportional to the number of bumps. This corresponds to the increase in the production of the turbulent kinetic energy especially near the wall as in figure 3.15. One can clearly observe the veering angle in the flat surface case and with slight obscured with bumps. The orientation of these structures are not random and do not orient themselves along the veering direction. The number density of vortical structures is smaller under stratification for case by case comparison. This is not surprising that the stratification suppresses vertical motion, reduces Reynolds stresses associated with vertical motion, leading to reduction of production. Consequently, the rate of turbulent kinetic energy cascading to smaller scales is reduced which is associated with the mechanism in the energy transfer, vortex stretching.

3.4 Conclusion

The mechanism of turbulence collapse and rebirth is investigated in detail with the analysis of turbulent fluxes. The inhibition of surface-layer shear production, associated with the buoyancy-induced reduction of the turbulent momentum flux, is the reason for turbulence collapse as was found by Ansorge and Mellado (2014); Shah and Bou-Zeid (2014). The positive buoyancy flux in the TKE budget is not the reason. Collapse is followed by turbulence recovery in both flat and rough cases. Notably, the mechanism of turbulence recovery in the rough cases is different from that in the Flat case. In the Flat case, a strong LLJ is formed at the end of turbulence collapse and, as found by Gohari and Sarkar (2017), pressure transport of fluctuations from the outer layer into the sheared lower flank of the LLJ triggers locally intermittent turbulence as the fluctuations interact with the enhanced shear of the LLJ. In contrast, we find in the 4Bump stratified case that the enhanced vertical (w) velocity in the near-surface roughness layer counteracts the buoyancy-induced reduction of turbulent momentum flux. Unlike the Flat case, shear production of TKE does not decay to a negligible value in the rough cases during the initial collapse of turbulence.

The roughness elements introduce a spatial organization into the flow. A triple decomposition is employed to isolate the coherent component. The roughness-associated dispersive component (total minus the incoherent part) of the Reynolds stress is found to be substantial in both unstratified and stratified cases. Since the incoherent component is strongly suppressed by buoyancy, the dispersive component becomes more important to the turbulence dynamics in the stratified cases. Additionally, in the stratified cases, the incoherent component is enhanced with respect to the Flat case.

The present small-amplitude bumps of $h^+ = 15$ correspond to a transitionally rough regime, have a gentle slope which does not lead to flow separation, and have a small effect on the flow in the neutral EBL. However, since the layer of boundary-associated turbulence thins during the initial collapse, the bump height becomes sufficient for the influence of roughness to reach

into an appreciable portion of the boundary layer so as to modify the shear and stratification in the boundary layer. In particular, the near-bottom region of subcritical Ri_g becomes substantially thicker in the rough cases and, correspondingly, the buoyancy-induced suppression of turbulent fluxes in the surface layer is mitigated. Thus, roughness modifies the boundary layer from a very stable regime in the Flat case to a stable regime.

For a sufficiently large cooling flux, larger than the value considered here, it is possible that the rough boundary layer reverts back to a very stable regime. In future work, we will systematically vary the cooling heat flux and roughness element height to further understand the role of roughness in counteracting the effect of stable stratification. It will also be desirable to extend simulations in future work to higher Re and a fully rough regime. Another future direction is the consideration of more complex geometry, e.g., three-dimensional obstacles and multiscale roughness.

Chapter 3, in full, is a reprint of the material as it appears in "Journal of Fluid Mechanics" Sungwon Lee, S.M. Iman Gohari, Sutanu Sarkar, Cambridge-Press, vol.902, 2020. The dissertation author was the primary investigator and author of this paper.

Chapter 4

Global modes and large-scale structures in an Ekman boundary layer

The goal of this work in collaboration with Jose Ortiz-Tarin, a colleague in the CFD lab, is to characterize the turbulent structures and large-scale motions in a stratified Ekman layer over a flat surface. These motions carry around 30-50% of the Reynolds shear stress and between 40-65% of the turbulent kinetic energy (TKE) (Balakumar and Adrian, 2007) in wall-bounded flows and despite their importance they have received scarce attention in the context of stratified Ekman boundary layers. In channels (Del Alamo et al., 2004) and pipes (Baltzer et al., 2013), their dynamics and scaling laws have been analyzed extensively, and their impact on the inner (Jiménez et al., 2004) and outer layers (Del Alamo et al., 2004) of the boundary layer has been described. In stratified channels, Flores and Riley (2011) investigated the signature of these structures through the spatial distribution of wall shear while Garcia-Villalba and Del Alamo (2011) described the suppression of vertical global modes by stratification. The novelty of this work lies in the inclusion of Coriolis acceleration to the aforementioned analysis. In geostrophic balance, a Ekman boundary layer develops a non-zero mean spanwise velocity which influences the establishment of large-scale structures. Below the buffer layer, Jiménez et al. (2004) distinguished between two

types of structures: long and narrow ones which are nearly independent of the outer flow and wide structures which extend to the outer flow and are influenced by it. We expect the latter to be affected by Ekman veering. In the outer flow, Del Alamo et al. (2004) derived a scaling for the ridge of the two-dimensional spectra of streamwise fluctuations based on the assumption that the lateral deviation of fluid elements was mostly caused by eddy diffusivity. Whether that scaling also holds in a boundary layer with a vertically varying mean lateral velocity is to be investigated. Deusebio et al. (2014) suggested the existence of transverse rolls in the EBL that were convected with the low-level jet. The presence of this rolls, their origin and their influence on the energy distribution across scales is investigated in the present work.

Figure 4.1 shows the streamwise velocity fluctuations, u'/u_*, spanwise velocity fluctuations, v'/u_*, vertical velocity fluctuations, w'/u_* and vertical vorticity (ω_z) contour on horizontal plane at $z^+ \approx 16$ for unstratified case in large domain. The grid resolution is same with previous chapter 3 and this domain size is chosen to fit the large scale structures identified by Del Alamo et al. (2004). Figure 4.2 shows the zoom-in view of figure 4.1. The flow structures are almost identical with small domain simulation results in figure 3.17 (a) and other results (not shown here).

4.1 Introduction

The interaction between the surface of the Earth and the atmosphere is critical to most human activities. It controls the evolution of weather and climate patterns as well as the dispersion of contaminants. Despite the significant amount of work on the atmospheric boundary layer (ABL), the role that underlying mechanisms like stratification, Coriolis acceleration, topography, or the transport of material, play in this interaction is still poorly understood. These effects are commonly studied separately, under strong simplifying assumptions, or combined, using complex parametrized models. The present work employs an Ekman boundary layer (EBL) as a canonical

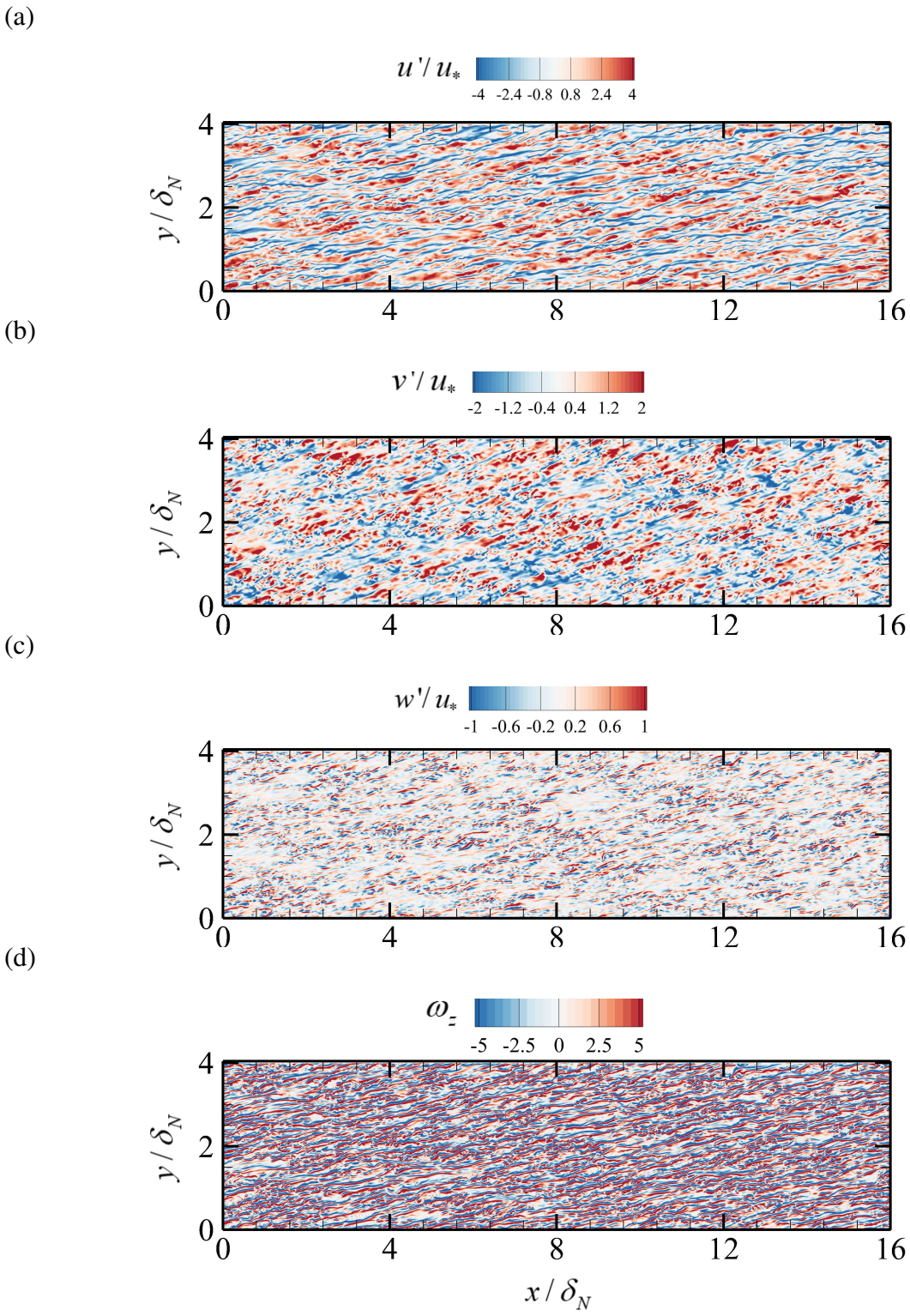

Figure 4.1: (a) Streamwise velocity fluctuations, u'/u_*, (b) spanwise velocity fluctuations, v'/u_*, (c) vertical velocity fluctuations, w'/u_* (d) vertical vorticity (ω_z) contour on horizontal plane at $z^+ \approx 16$ for unstratified case in large domain.

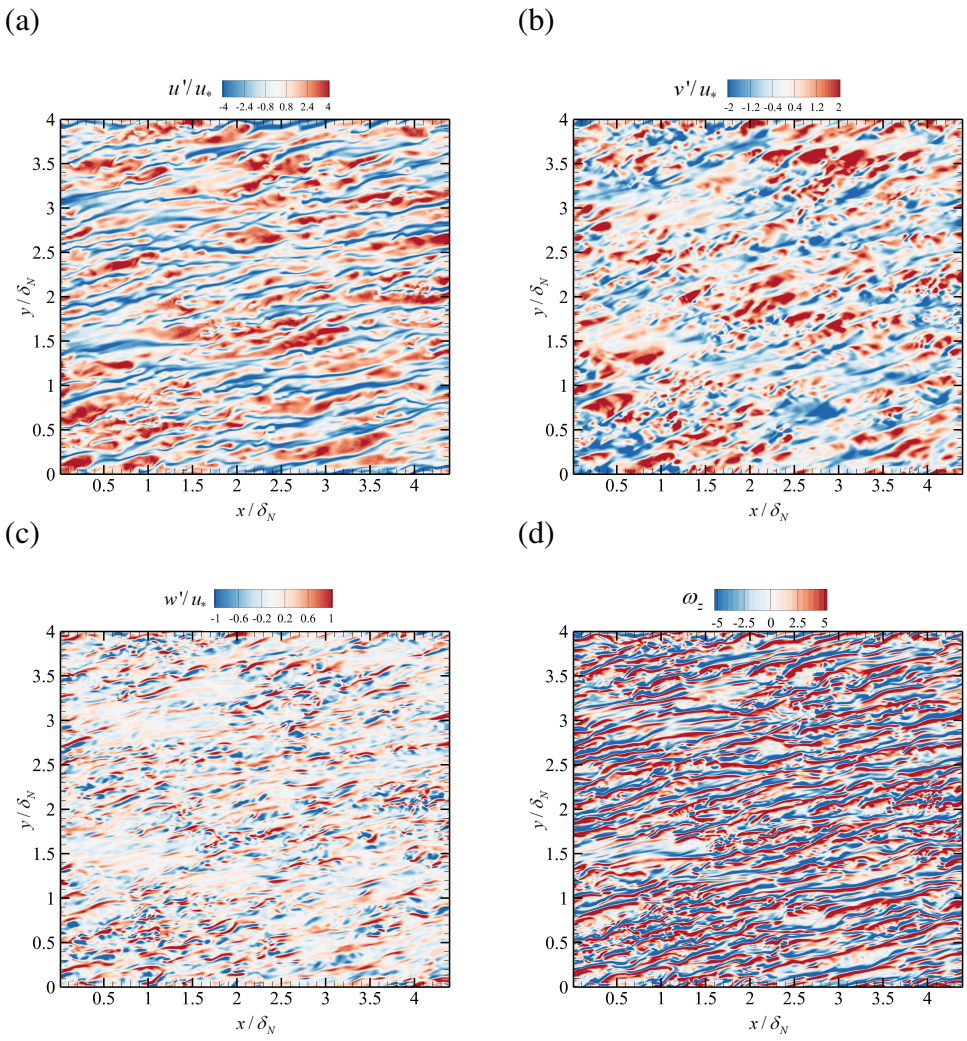

Figure 4.2: zoom in contour (a) Streamwise velocity fluctuations, u'/u_*, (b) spanwise velocity fluctuations, v'/u_*, (c) vertical velocity fluctuations, w'/u_* (d) vertical vorticity (ω_z) contour on horizontal plane at $z^+ \approx 16$ for unstratified case in large domain. For ease of comparison of these plots with similar plots in the previous chapter, we revert to z and y for vertical and spanwise directions, respectively.

flow to study the effect of Earth's rotation on the wall turbulence generated on the surface of the ABL. An EBL is generated in a rotating reference frame when the Coriolis force balances a lateral pressure gradient. This equilibrium, commonly referred as geostrophic balance, is broken near the wall due to the effect of viscous forces and leads to the sideways veering of the flow. The veering angle of the flow depends on the height generating a "spiral-like" mean velocity profile. This mean velocity profile is different from the one observed in non-rotating boundary layers and can lead to different types of instabilities and to a different self-sustaining cycle of the near wall turbulence.

Whereas most of the ABL work is focused on the scaling of turbulent fluxes for modeling purposes, studies on the EBL have been primarily concerned with the effects of rotation and stratification on turbulent motions. Albeit being a simplified version of the ABL, the EBL allows to translate insights from other turbulent canonical flows like the channel flow to the study of the atmosphere. Previous computational works on turbulent EBL include the seminal work of Coleman et al. (1990) who derived a correlation for the friction velocity as a function of the latitude and the Reynolds number, and the recent works of Deusebio et al. (2014), Ansorge and Mellado (2014), Flores and Riley (2018) and Gohari and Sarkar (2018). Motivated by observations in the nocturnal boundary layer, these studies are mainly focused on the effect that stable stratification plays on the intermittency of turbulence and collapse/recovery of turbulence. Here, intermittency takes the form of global (also called spatial) intermittency, which refers to patchy turbulence in an otherwise quiescent flow.

The rest of the paper is organized as follows. First, the formulation of the problem and the simulation setup are described in section 2. Then, sections 3 and 4 analyze the main velocity structures in the turbulent EBL using flow visualization and spectral energy distributions, respectively. In section 5 the observed structures are analyzed from the point of view of linear stability. Conclusions are presented in section 6.

4.2 Problem formulation and simulation setup

The Navier-Stokes equations are solved in a direct numerical simulation. The conservation of momentum including the effect of Coriolis acceleration reads

$$\frac{\partial u_i}{\partial t} + \frac{\partial (u_i u_j)}{\partial x_j} = -\frac{\partial p}{\partial x_i} + f\varepsilon_{ij3}(u_j - U_\infty \delta_{j1}) + \nu \nabla^2 u_i, \tag{4.1}$$

where f is the Coriolis parameter, δ_{j1} is the Kronecker delta, and ε_{ij3} is the Levi-Civita symbol. The flow outside the boundary layer is in geostrophic balance, meaning that the Coriolis force balances the lateral pressure gradient. In equation 4.1, U_∞ is the geostrophic wind speed and p is the deviation of the kinematic pressure from the geostrophic balance that enforces the solenoid condition $\partial u_i/\partial x_i = 0$. The x direction in the coordinate system is aligned with the geostrophic wind. Different from the other chapters, we adopt the notation of the engineering literature here, i.e. y is wall-normal (vertical) and z is spanwise. In index notation they read $x_i = (x_1, x_2, x_3)$, respectively. The corresponding velocity components are $u_i = (u_1, u_2, u_3) = (u, v, w)$. The bottom boundary condition is no-slip ($u_i = 0$), and the inlet-outlet and lateral boundaries are periodic. The upper boundary is stress-free ($\partial u_i/\partial y = 0$). The governing parameters of the steady-state EBL are $\{f, \nu, U_\infty\}$ which lead to the definition of the laminar boundary layer height $D = \sqrt{2\nu/f}$ and the Reynolds number $Re_D = U_\infty D/\nu$. Alternatively, a large scale Rossby number equivalent to Re_D might be defined as $Ro_D = U/fD$. Since the present work is concerned with a turbulent EBL, it is more appropriate to define the turbulent boundary layer height $\delta = u_*/f$, where u_* is the friction velocity defined by $u_*^2 = \nu \frac{\partial U_i}{\partial y}\Big|_{y=0}$. This new characteristic height leads to the definition of the friction Reynolds number $Re_* = u_*\delta/\nu$ and the turbulent Rossby number $Ro_* = u_*\delta/f = 1$. Note that u_i' is the fluctuation velocity defined as $u_i' = u_i - U_i$, where $U_i = \langle u_i \rangle$ is the mean velocity averaged over horizontal homogeneous planes. The definition of the friction velocity u_* also leads to the introduction of the near-wall scaling $\{\nu/u_*, u_*\}$, denoted by the superscript $+$ and the outer scaling $\{\delta, U_\infty\}$, denoted by the superscript $-$.

Table 4.1: Direct Numerical Simulation (DNS) parameters for large domain. (16 δ_N x 4 δ_N x 2 δ_N)

Case	Re_*	Initial L^+	L_x^+	L_y^+	L_z^+	$N_x \times N_y \times N_z$	Δx^+,Δy^+,Δz^+_{min}
Flat_{16d}	697	∞	11200	1400	2800	$1284 \times 129 \times 512$	8.6, 0.98, 5.29

*Physical and numerical parameters used in the simulations. N_x, N_y, and N_z are the number of nodes (grid points) in the streamwise, spanwise, and vertical direction respectively.

The solver employs a low storage, third-order Runge-Kutta method to advance in time. (Williamson, 1980) The spatial derivatives are computed with second-order central finite differences in the vertical direction and with a pseudo-spectral method (FFT) in the horizontal directions. The 2/3 rule is employed to avoid aliasing in the computation of the convective terms. More details of the numerical model can be found in Gohari and Sarkar (2018). The grid resolution is chosen based on previous works Garcia-Villalba and Del Alamo (2011); Gohari and Sarkar (2017), so that in the vertical direction $\Delta^+_{ymin} = 0.98$ and $\Delta^+_{ymax} = 18$. In the horizontal directions $\Delta^+_{zmax} = 5.29$ and $\Delta^+_{xmax} = 8.6$. The domain size is chosen so that the large scale structures identified by Del Alamo et al. (2004) fit the domain. The parameters of the simulation are shown in table 4.1.

4.3 Visualization

A three-dimensional snapshot of the flow is provided in figure 4.3 (c). The intense structures in the boundary layer are colored by height. The near wall structures (colored in blue) are aligned with the veering angle of the flow (i.e., clockwise) while the outer long structures (colored in red) have a different orientation. The tallest attached structures reach $y \approx 0.4\delta$ while Del Álamo (2005) found global modes reaching $y = h$ at a similar Reynolds number in a channel. In the channel, the half-height h is the characteristic length scale of the outer flow, a priori,

equivalent to δ in the EBL.

A detail of the structures near the wall is shown in figure 4.3 (a), where the vorticity streaks seem to align with the mean flow. Further from the wall, at $y^- = 0.2$, figure 4.3 (b) shows a contour of streamwise velocity fluctuations where the imprint of the inclined long rolls can be observed. Interestingly, the orientation of these rolls is not parallel to the local mean velocity, but seems to be closer to the direction of the shear (dotted line in figure 4.3 (b)). It should be noted that, in the near-wall region, the difference between the direction of the mean flow and the direction of the shear is small, and it is difficult to determine if the near-wall streaks align better with one or the other.

To compare the dynamics of the EBL with previous findings in turbulent channels is necessary to compare their mean velocity profiles. Figures 4.4 (a) and (b) show the total horizontal velocity ($G^+ = \sqrt{U^{+2} + V^{+2}}$) in a channel and in an EBL. Near the wall both profiles show a very similar behaviour, however, around $y^- \approx 0.4$ the velocity magnitude G^+ of the EBL stays constant. This region of constant velocity and no shear contrasts with the increase of velocity observed in the center of the channel. The lack of shear in the outer part of the EBL leads to zero turbulent production $P = \partial U_i / \partial x_j \langle u_i' u_j' \rangle$ above $y^- \approx 0.4$. Figures 4.4 (d) and (e) show the rapid decay of turbulent kinetic energy ($K = 1/2 \langle u_i' u_i' \rangle$) in the upper part of the EBL. This feature explains the limited height of the intense structures shown in figure 4.3.

4.4 Spectra

To investigate the effect of the veering angle in the distribution of energy across scales the present section compares the two-dimensional premultiplied energy spectra of the EBL with the $Re_\tau = 550$ channel of Del Alamo et al. (2004). The spectra are premultiplied with the wavenumber so that when visualized in logarithmic scale the volume under the surface corresponds with the energy content at those scales. Two heights have been chosen, $y^+ = 15$, corresponding to the

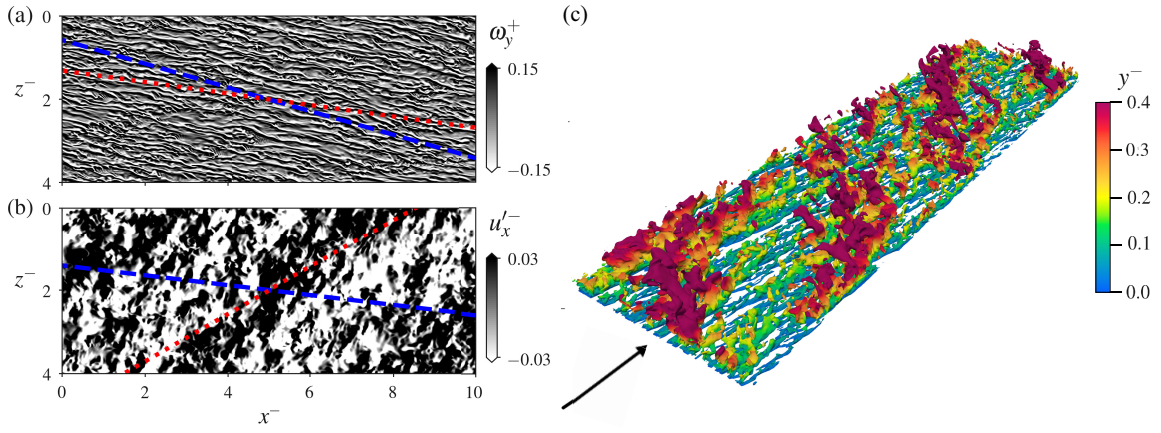

Figure 4.3: (a) Vertical vorticity plane at $y^+ = 15$ and (b) streamwise velocity fluctuations u_x' at $y^- = 0.2$. The dashed blue line (- - -) shows the angle of the mean flow and the dotted red line $(\cdots)$ the angle of the shear. (c) Intense structures in the EBL identified by isocontours of $u_x' = -u_*$ coloured by height. The arrow shows the outer flow direction.

location of the peak of turbulent kinetic energy and $y^- = 0.2$, a height in the outer layer where the energy content of the two flows is still comparable. Two considerations have to be taken into account when computing the energy spectra of the EBL. First, since the EBL is not reflection-invariant in the spanwise direction, unlike the channel, the distinction between positive and negative wavenumbers has to be done. The second consideration is that, since the flow is not aligned with the mesh direction the flow has to be rotated before taking the Fourier transform of the velocity components. To that end, before computing the spectra, the velocity components are projected into a new reference frame and the fields are interpolated into a new mesh aligned with the new directions. To align with the flow, a priori one should either align with the mean veering angle $\alpha = \arctan W/U$ or with the shear angle $\beta = \arctan \tau_{zy}/\tau_{xy}$ (Lozano-Durán and Bae, 2019), where $\tau_{ij} = \nu \partial U_i/\partial x_j - \langle u_i' u_j' \rangle$. Choosing the proper angle should lead to a distribution of energy between the positive and negative span-wise wavenumbers as even as possible. Through the paper, the direction along the shear is referred as shearwise (underscript s) and the corresponding orthogonal direction is transverse-shearwise (underscript t). The directions specified by the veering angle are referred as streamwise (underscript st) and spanwise (underscript sp).

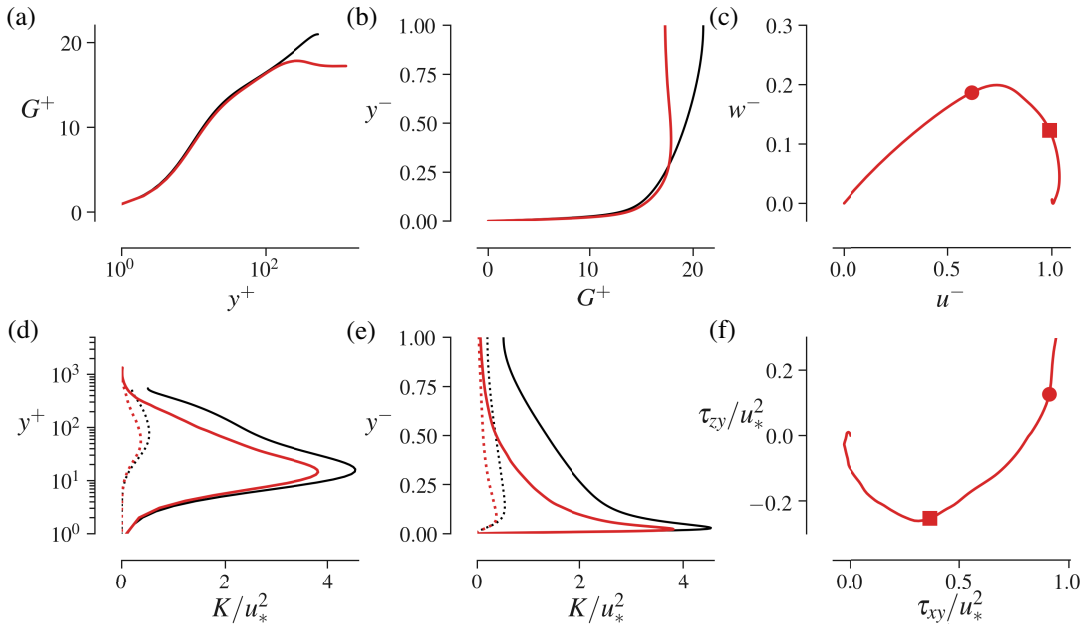

Figure 4.4: Red lines correspond to EBL and black lines to the channel flow of Del Alamo et al. (2004). (a,b) Vertical variation of the mean horizontal velocity (G) in inner (a) and outer scaling (b). (d,e) Vertical variation of the turbulent kinetic energy (K) in inner (d) and outer scaling (e). The height in outer scaling y^- is normalized with δ in the EBL and h in the channel. K_H (solid lines) and K_V (dashed lines) are the horizontal and vertical components of K. (c) Velocity profile showing the veering angle. (f) Evolution of the shear components. The circle ● marks the $y^+ = 15$ height and the square ■ corresponds to $y^- = 0.2$.

Figure 4.5 shows the energy spectra of the EBL at $y^+ = 15$ together with the channel flow spectra of Del Alamo et al. (2004). The horizontal directions are aligned with the angle of the shear at that height and the energy distribution among the positive and negative shear-transverse wavenumbers is shown as a percentage of the total kinetic energy. The straight solid line marks the location of isotropic structures $\lambda_t^+ = \lambda_s^+$ with same width than length. The dashed line marks the location of elongated structures that follow $\lambda_t^+ = 13\lambda_s^{+1/3}$. This power relation for the anisotropic structures was obtained from the Squires equation by assuming constant eddy diffusivity (Jiménez et al., 2004; Del Álamo, 2005; Del Alamo et al., 2004; Schmid and Henningson, 2001). The overall shape of the spectra and the location of the maxima match that of the channel. The spectrum of $\langle u_s' u_s' \rangle$ shows a shorter tail in the case of the EBL and the cross-shear component of Reynolds stresses $\langle u_t' u_t' \rangle$ shows a longer tail towards wide or transverse structures.

The excellent overlay of the channel and the EBL isolines in the short wavelength region can be readily explained by the viscous nature of the dynamics at those scales. They are independent of the flow driving mechanism or large-scale features. The energy distribution between positive and negative wavenumbers is even in the vertical velocity and shear-transverse velocity spectra but not in the shearwise. The spectra aligned with the mean flow (not shown) showed a more skewed energy distribution, on average the positive λ_{sp} had 1.8 times the energy of the negative wavelengths, suggesting that the shear angle marks better the principal directions in the near-wall region.

Figure 4.6 shows the energy spectra in the outer region of the EBL ($y^- = 0.2$). Here, the directions are taken to be given by the mean flow veering angle. In this case, neither the mean veering angle nor the shear angle provide a good estimate of the flow principal directions and the mean veering angle is chosen for illustration purposes. A singular value decomposition of the fluctuating velocity field can be used to obtain the axis that provides a symmetric energy distribution, however, every velocity component leads to a different principal direction. Regarding the maxima and the shape of the premultiplied spectra, at this height, the channel and the EBL show more differences than near the wall. A general feature is that the spectra of the EBL are more isotropic than those of the channel. Also, the energetic structures are shorter and wider, as can be seen in the shorter streamwise tail of figure 4.6 (a) and the energetic region in the wide structures of figure 4.6 (c).

4.5 Stability analysis

To characterize the influence of the Coriolis acceleration in the wall-turbulence self-sustaining cycle a linear stability analysis was performed linearizing the equations respect to the mean profiles of the EBL. Figure 5 shows the unstable region over the premultiplied energy spectra at $y^- = 0.2$. Since the stability analysis is performed along the geostrophic streamwise

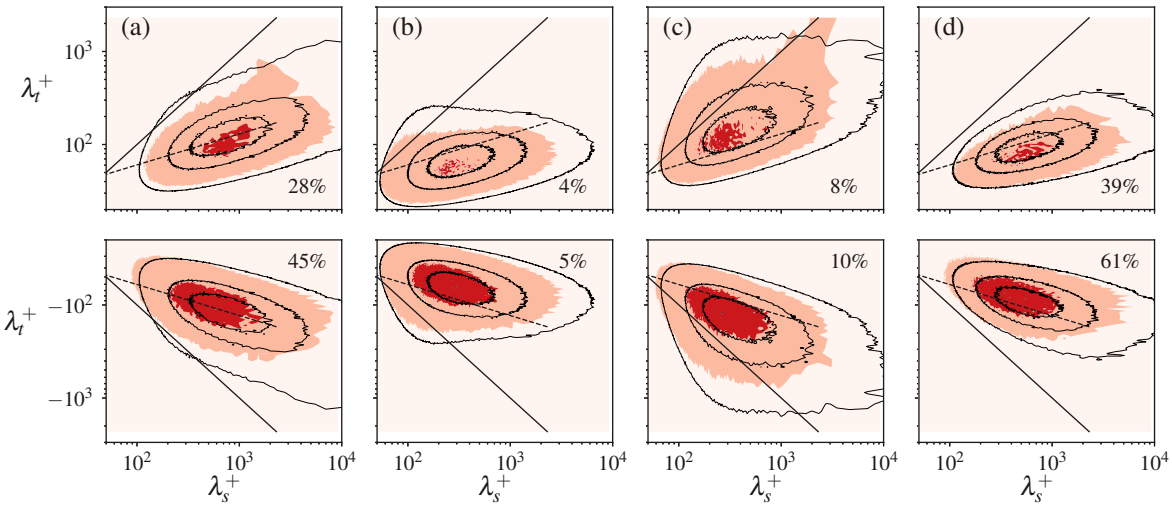

Figure 4.5: Premultiplied two-dimensional energy spectra of the EBL $k_s k_t E^{2D}(\lambda_s, \lambda_t)/u_*^2$ along the shearwise (k_s) and the shear-transverse (k_t) directions at $y^+ = 15$. The angle of the shear at that height is $\beta = 7.9°$. The shaded contours are 0.1 (salmon), 0.4 (red) and 0.7 (not visible) times the peak value of the channel spectra of (Del Alamo et al., 2004). The black isolines correspond the to the channel spectra also at 0.1, 0.4 and 0.7 of the peak value. Solid straight line $\lambda_t^+ = \lambda_s^+$. Dashed line $\lambda_t^+ = 13\lambda_s^{+1/3}$. (a) Shearwise velocity. (b) Vertical velocity. (c) Shear-transverse velocity. (d) Reynolds-stress cospectrum.

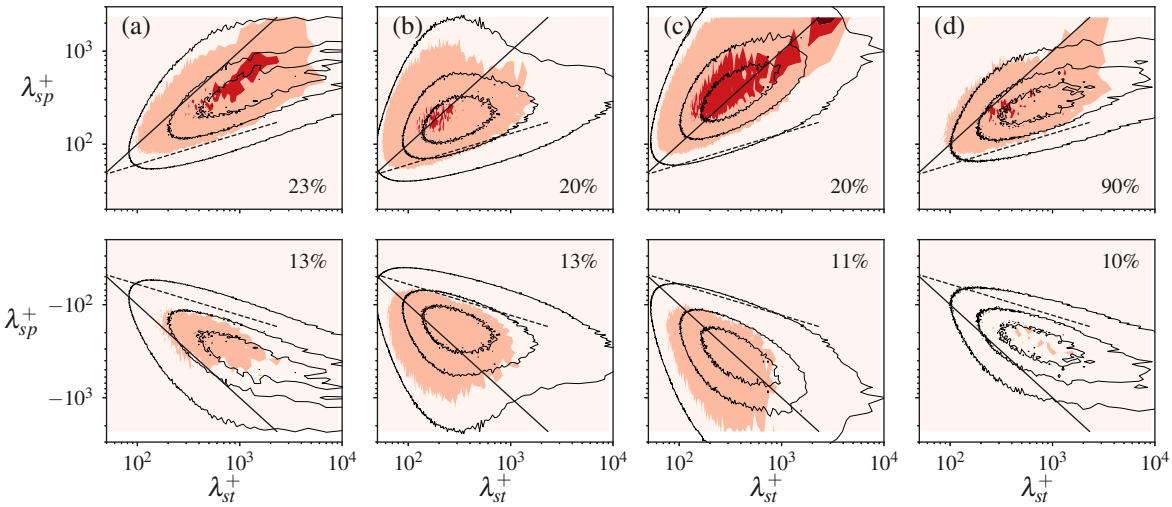

Figure 4.6: Premultiplied two-dimensional energy spectra $k_{st} k_{sp} E^{2D}(\lambda_{st}, \lambda_{sp})/u_*^2$ along the streamwise (k_{st}) and spanwise (k_{sp}) directions at $y^- = 0.2$. The veering angle at that height is $\alpha = 7°$. The shaded contours are 0.1 (salmon), 0.4 (red) and 0.7 (dark red) times the peak value of the channel spectra of (Del Alamo et al., 2004). The black isolines correspond to the channel spectra also at 0.1, 0.4 and 0.7 of the peak value. Solid straight line $\lambda_{sp}^+ = \lambda_{st}^+$. Dashed line $\lambda_{sp}^+ = 13\lambda_{st}^{+1/3}$. (a) Streamwise velocity. (b) Vertical velocity. (c) Spanwise velocity. (d) Reynolds-stress cospectrum.

and spanwise directions (x and z) the contributions of u'_x and u'_z are added and the spectrum of the total horizontal turbulent kinetic energy is shown. The stability analysis shows that, contrary to the channel, the EBL has a modal instability for $\lambda_x^+ > 400$, and different ranges of spanwise wavelengths for $k_z > 0$ and $k_z < 0$, with a wider range of unstable wavenumbers on the $k_z > 0$ plane. Indeed, the largest eigenvalues of $k_z > 0$ are approximately two times larger than those in $k_z < 0$, suggesting that the $k_z > 0$ plane is more unstable. Note that this is again a result of the asymmetry of the flow along the spanwise direction, due to the veering of the mean flow. The velocity structures associated to $k_z > 0$ wavenumbers are aligned to a direction that turns left with respect to the x-direction, while those associated to $k_z < 0$ wavenumbers turn right. See figure 5(c,d).

The analysis of the modes associated with the most unstable eigenvalue at each (k_x, k_z) shows that, in general, the unstable modes of the $k_z > 0$ plane correspond to attached velocity structures, like the one shown in figure 4.7 (c). These modes tend to have horizontal velocities reaching all the way to the wall, with a detached v-velocity structure, so that the maximum of both u and w is attained closer to the wall than the maximum of v. For sufficiently large wavelengths, the horizontal velocity component of the eigenvector tends to exhibit a flattened top, reminiscent of the oblique structures observed in figure 4.3 (c). In particular, the mode shown in figure 5(c) corresponds to $\lambda_x^+ = 4000$ and $\lambda_z^+ = 2000$. It corresponds to the largest structures observed in the energy spectrum of the horizontal velocities in figure 5(a), and agrees very well with the visualization of figure 4.3 (c).

The modes associated with the unstable region of the $k_z < 0$ plane are different. They usually correspond to wall-detached structures, with maximum velocities located around or above the mean velocity maximum. For example, figure 4.7 (d) shows the $k_z < 0$ counterpart of the mode shown in figure 4.7 (c). The differences between the modes are clear, with the one at $k_z < 0$ barely reaching wall distances below $y^+ \approx 500$. Interestingly, the spectrum of the horizontal velocities at $y^- = 0.2$ ($y^+ = 134$) shown in figure 4.7(a) also shows a energy peak at that wavelength,

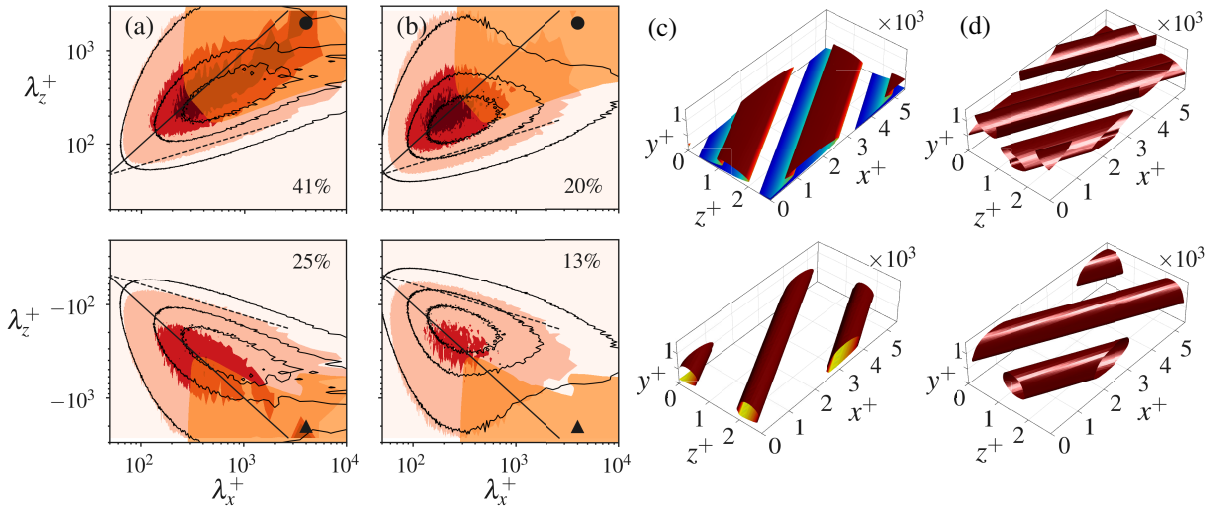

Figure 4.7: Stability map over the premultiplied two-dimensional energy spectra of EBL $k_x k_z E^{2D}(\lambda_x, \lambda_z)/u_*^2$ along the geostrophic streamwise (k_x) and spanwise (k_y) directions at $y^- = 0.2$. The shaded orange region corresponds to unstable wavenumbers. The shaded contours are 0.1 (salmon), 0.4 (red) and 0.7 (dark red) times the peak value of the channel spectra of (Del Alamo et al., 2004). The black isolines correspond to the channel spectra also at 0.1, 0.4 and 0.7 of the peak value. (a) Horizontal velocity. (b) Vertical velocity. (c) Upper: visualization of mode ● with isosurfaces of streamwise velocity. Lower: visualization of mode ● with isosurfaces of vertical velocity. (d) Upper: visualization of mode ▲ with isosurfaces of streamwise velocity. Lower: visualization of mode ▲ with isosurfaces of vertical velocity. The selected isosurface has $u, v = 0.5\max(v)$, and it is coloured by height following figure 4.3 (c).

suggesting that this mode leaves an imprint closer to the wall.

4.6 Conclusions

The influence of Coriolis acceleration in the large-scale dynamics of wall-turbulence has been studied with a direct numerical simulation of an Ekman boundary layer (EBL) at $Re_* = 697$. To elucidate the role of rotation, the present results have been compared to previous studies of channels at comparable Reynolds numbers (Del Alamo et al., 2004). The mean statistics of the EBL show that the turbulent kinetic energy (K) content is confined to a maximum height of $y^- \approx 0.4$ whereas in the channel, the content of turbulent kinetic energy spans its half height (h). This is consistent with the conventional practice of estimating the boundary-layer height as $\delta^- = 0.5$ in the EBL and h in channel flow. The largest structures in the turbulent EBL seem to be rollers of height $y^- \approx 0.4$ oriented at -45° from the geostrophic flow. The height, the orientation and the origin of these rollers is qualitatively different to the global modes of height h observed in turbulent channels.

In order to perform a quantitative comparison between the two flows, the premultiplied two-dimensional spectra of the velocity fluctuations of a turbulent channel have been compared with those of the EBL. In the outer region of the EBL ($y^- = 0.2$) the energy is distributed in wider and shorter structures than in the case of the channel. Near the wall ($y^+ = 15$), however, the energy content of the small and intermediates scales is the same in the channel and the EBL. This suggests that the near-wall or buffer-region dynamics are not affected by the veering of the mean velocity, which is consistent with the hypothesis of an autonomous cycle in the buffer region. To distribute the energy evenly among the positive and negative spanwise wavenumers two different frames are tested, the shear-oriented frame and a frame oriented with the veering angle of the mean flow. Near the wall the shear angle is a good estimate of the flow principal direction. However, further from the wall, neither the mean veering angle nor the shear angle are able to distribute the energy evenly.

Finally, a linear stability analysis has been performed using the mean profiles of the EBL.

Whereas the channel does not show any modal instability, the analysis of the EBL reveals a range of unstable modes, both for $k_z > 0$ and for $k_z < 0$. The former correspond to wall-attached structures, usually confined within the lower half of the EBL height δ. The latter generally correspond to unstable structures above the mean velocity maximum, although they have some signature in the energy spectrum within the turbulent part of the EBL. Interestingly, the velocity structures (i.e. the rollers) observed in the instantaneous visualizations seem to agree very well with these modes, showing that their origin is a modal instability of the mean velocity profile and not a transient growth instability like the one found in the channel flow (Schmid, 2007).

Chapter 4, in full, is a reprint of the material as it appears in "Journal of Physics: Conference Series" Jose L. Ortiz-Tarin, Sungwon Lee, Oscar Flores, Sutanu Sarkar, Institute of Physics, vol.1522, 2020. The dissertation author was one of the primary investigator and coauthor of this paper.

Chapter 5

Further effects of surface roughness in a stratified Ekman boundary layer

5.1 Introduction

In chapter 3, we found that, at the normalized Obukhov length scale $L^+ \approx 700$, the cooling flux is sufficient to cause the initial collapse of turbulence from its initial neutral-EBL state. In the previous simulation, we imposed a constant surface buoyancy flux for a finite time interval of $ft \approx 6$ for all cases. To further investigate the evolution of Ekman boundary layers at rough surfaces, we have conducted additional DNS at different values of cooling flux, different values of cooling time and different values for roughness height. We hypothesize that the final Ri_b may be sufficient to provide guidance on the overall state of the flow, e.g. weakly or strongly stable in the sense of Mahrt (1998). The weakly stable regime has continuous turbulence while the strongly stable regime exhibits globally intermittent or locally intermittent turbulence.

To provide a meaningful comparison, the simulations are performed as follows. For each case, we start from the simulation of the neutral Ekman flow until it reaches statistically steady state. The neutral flow field, which varies if the roughness element is changed, is used as the initial

condition for the stratified cases. Thus, the initialization is consistent with neutral conditions at sunset (Metzger et al., 2007; Flores and Riley, 2011), and is similar to the approach of several other studies (Ansorge and Mellado, 2014; Nieuwstadt, 1984; Flores and Riley, 2011; Shah and Bou-Zeid, 2014; Deusebio et al., 2014). The specified value of normalized Obukhov length scale determines the value of constant surface buoyancy flux, which is imposed for a finite time interval. The surface cools to a case-dependent temperature at the end of the interval and, subsequently, this value of surface temperature is held constant.

5.2 Results

5.2.1 Effect of the time duration of the applied surface buoyancy flux in the stratified Ekman boundary layer

We investigate the effect of changing the buoyancy-flux application time from its value of $ft = 2\pi$ in chapter 3 to $ft = \pi$. Table 5.1 summarizes the parameters of the new DNS conducted at $Re_* \approx 700$.

Table 5.1: DNS parameters* for the cases conducted with the different cooling time of $ft = \pi$. The subscript π on the label distinguishes each case from the corresponding case in the chapter 3 series.

Case	Re_*	Ri_b	Initial L^+	h^+	l^+	AR (l/h)	Cooling period	$N_x \times N_y \times N_z$	Δx^+,Δy^+,Δz^+_{min}
Flat$_\pi$	697	**0.284**	700	-	-	-	π	$321 \times 256 \times 129$	8.46, 5.29, 0.98
2Bump$_\pi$	672	**0.283**	700	15	350	23.3	π	$481 \times 256 \times 129$	5.61, 5.26, 0.73
4Bump$_\pi$	668	**0.235**	700	15	175	11.6	π	$481 \times 256 \times 129$	5.55, 5.20, 0.71

* N_x, N_y, and N_z are the number of nodes (grid points) in the streamwise, spanwise, and vertical direction, respectively. Here l is the half of the bump streamwise length and is related to λ (the roughness wave length) by λ=4l.

Figure 5.1 shows time evolution of integrated TKE and Ri_b for Flat (a-b), 2Bump (c-d)

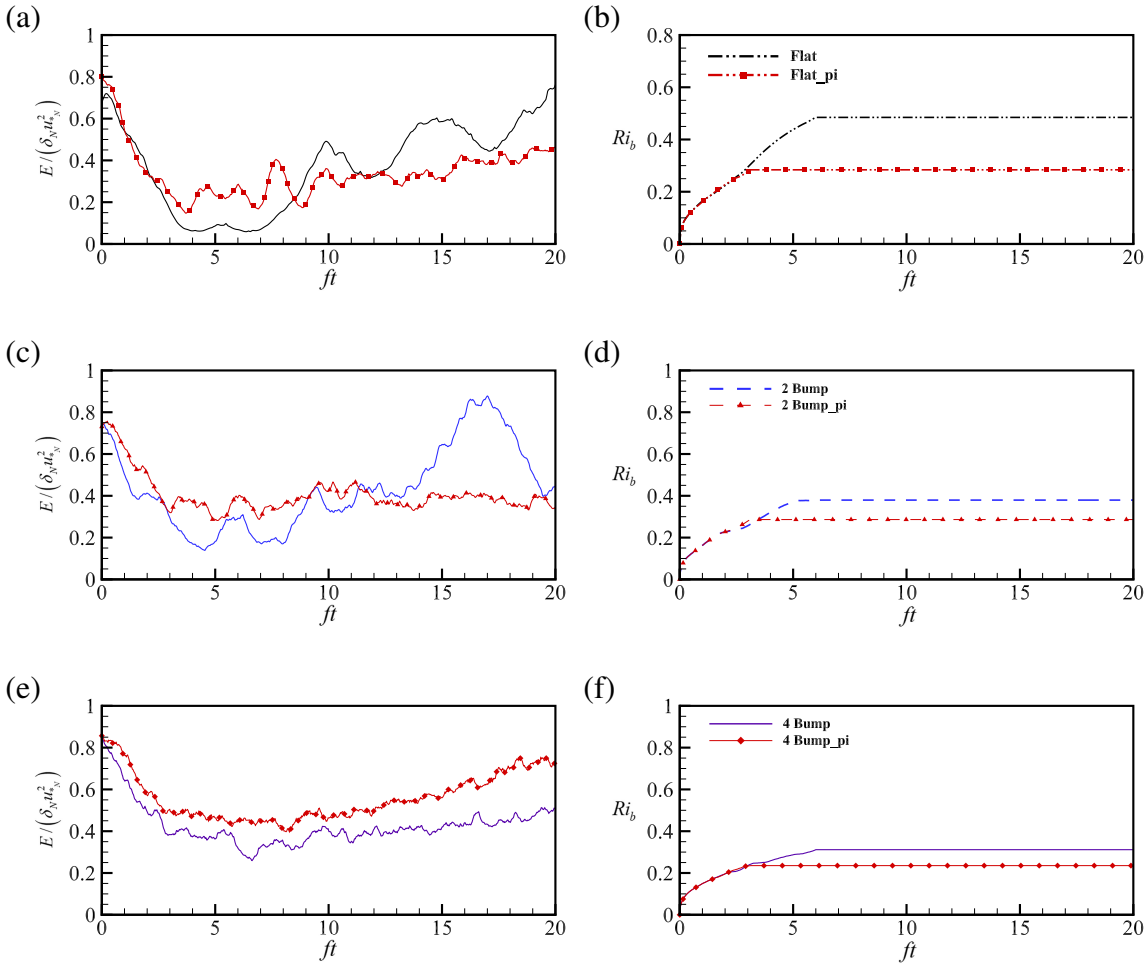

Figure 5.1: Time series of integrated turbulent kinetic energy ($E/(\delta_N u_{*_N}^2)$) and bulk Richardson number (Ri_b) for Flat (black) and Flat$_\pi$, (c-d) 2Bump (blue) and 2Bump$_\pi$, (e-f) 4Bump (purple) and 4Bump$_\pi$. Surface cooling period with π is shown in red line.

and 4Bump (e-f) cases, and contrasts results for the shorter cooling time of $ft = \pi$ (in red) with those obtained with $ft = 2\pi$. All cases have the same buoyancy flux corresponding to $L^+ \approx 700$. Because of the shorter shorter cooling time of $ft = \pi$, TKE does not drop as much. Thus, unlike the Flat case, TKE in the Flat_π case does not reduce to almost zero during the initial collapse. In the early stage (up to $ft = \pi$), the initial evolution of TKE is similar to the previous case; however, the later evolution of TKE is quite different. Flat and 2Bump cases show temporal intermittency with large-amplitude oscillations at the inertial period, $ft = 2\pi$. However, the temporal evolution of TKE in the Flat_π case is similar to the 4Bump case and the large-amplitude inertial modulation is removed. In other words, the behavior moves from a very stable boundary layer towards a weakly stable boundary layer. In the 2Bump_π case too, the temporal intermittency at late time, which was present in the 2Bump case, is removed. Roughness additionally augments the TKE as can be seen by comparing the 2Bump_π case with the Flat_π case.

Based on these results, we infer that the introduction of bumps has a similar effect as the reduction in cooling time. This can be understood by assessing the final Ri_b, an overall measure of the net amount of stabilization. The selection of the cooling time of $ft = \pi$ in the Flat_π case leads to a final $Ri_b = 0.284$ which is similar to the 4-Bump value of $Ri_b = 0.312$. Figure 5.1 (c-d) shows that the 2Bump_π case that has a final Ri_b of 0.283, much smaller than $Ri_b = 0.379$, the final value in the 2Bump case with the longer cooling time of $ft = 6$. Similar to the Flat_π case, the shorter cooling period in the 4Bump_π case is not sufficient to collapse the turbulence to a negligible level. The temporal evolution of TKE in the 4Bump_π case is qualitatively similar to the 4Bump case with both belonging to the weakly stable regime. Figure 5.1 (e-f) shows that the 4Bump_π case has a final Ri_b of 0.235, which is lower than the final $Ri_b = 0.311$ in the 4Bump case and, correspondingly, it has a somewhat higher TKE.

5.2.2 Effect of roughness height

We now move on to examine the effect of varying the roughness-element size without changing the geometry. The rough surface was defined by Eq.3.1, where h is the height of the roughness and λ is the wavelength of the roughness. Table 5.2 summarizes the parameters of DNS simulations where the roughness height and length are varied, keeping the *same value of steepness* or aspect ratio (l/h).

In the case of 2Bump_{30}, the height of the roughness element is doubled to $h^+ = 30$ and so is the the wavelength relative to the 4Bump_{15} case. Thus, although these two case have different roughness height, their aspect ratio is identical. It appears that the aspect ratio is a key controlling parameter since the TKE evolution (Figure 5.3 a) is similar between the two cases, and the final Ri_b (Figure 5.3 b) for 2Bump_{30} is 0.289, similar to the Ri_b of 0.312 for the 4Bump_{15} case. To prove this hypothesis, we simulate another case with the same l/h to demonstrate that the key parameter is the steepness of the surface roughness and not its height as long as the flow is in the transitionally rough regime. We confirm with another simulation of $8\text{Bump}_{7.5}$ that has the same aspect ratio of $l/h = 11.6$. Figure 5.3 shows the temporal evolution of turbulent kinetic energy and bulk Richardson number for 2Bump_{30}, 4Bump_{15} and $8\text{Bump}_{7.5}$ cases. As is clear from figure 5.3(a), the trend of the TKE is similar among the three cases and the final value of bulk Richardson number is also similar even though the roughness height is different. The final Ri_b for $8\text{Bump}_{7.5}$ is 0.334. From these results, we can infer that the final Ri_b is sufficient to provide guidance on the overall state of the flow. Figure 5.4 shows the streamwise vorticity contour on a horizontal plane at $z^+ \approx 16$ of 4Bump_{15} case and 2Bump_{30} case at $ft \approx 6$. The r.m.s. turbulence levels at $z^+ \approx 16$ are almost identical between the two cases. The vertical profiles of TKE are also similar although, in the outer layer, there are slight differences of the components of TKE between the two cases.

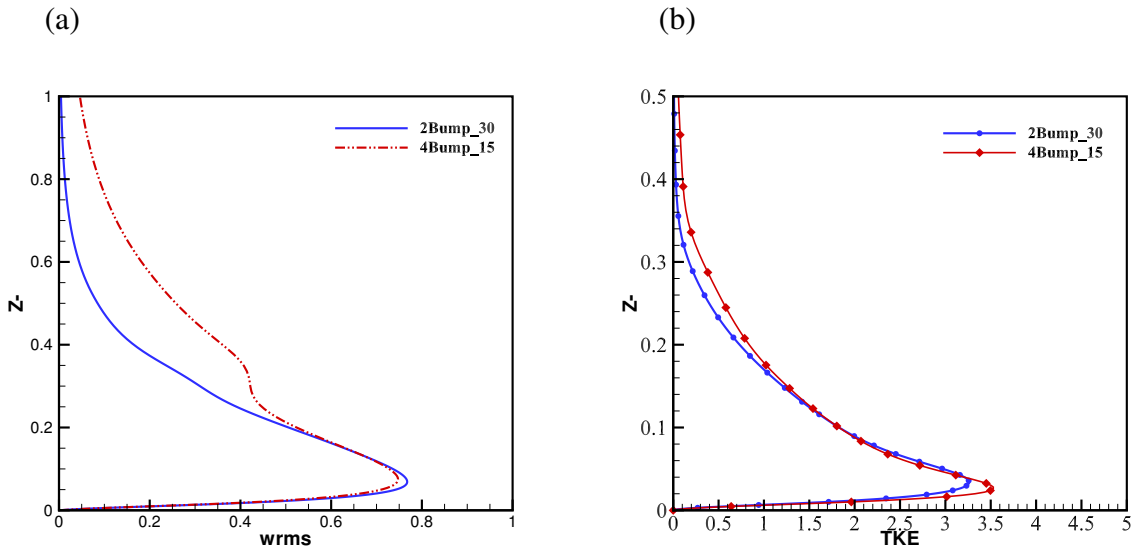

Figure 5.2: Time averaged profiles of velocity fluctuation statistics contrasted between 2Bump_{30} and 4Bump_{15} cases:(a) vertical velocity fluctuations, (w_{rms}) (b) turbulent kinetic energy profiles

Table 5.2: DNS parameters* for the series where the roughness height is varied with respect to chapter 3, keeping the aspect ratio (AR) constant. The subscript on the case label stands for the roughness height in wall units, h^+.

Case	Re_*	Ri_b	Initial L^+	h^+	l^+	AR (l/h)	$N_x \times N_y \times N_z$	Δx^+,Δy^+,Δz^+_{min}
2Bump_{30}	643	**0.289**	700	30	350	11.6	$481 \times 256 \times 193$	5.59, 5.24, 0.72
4Bump_{15}	668	**0.312**	700	15	175	11.6	$481 \times 256 \times 193$	5.55, 5.20, 0.71
$8\text{Bump}_{7.5}$	651	**0.334**	700	7.5	87.5	11.6	$481 \times 256 \times 193$	5.56, 5.21, 0.72

* N_x, N_y, and N_z are the number of nodes (grid points) in the streamwise, spanwise, and vertical direction, respectively. N_x, N_y, and N_z are the number of nodes (grid points) in the streamwise, spanwise, and vertical direction, respectively. Here l is the streamwise half-length of the bump and is related to λ (the roughness wave length) by λ=4l.

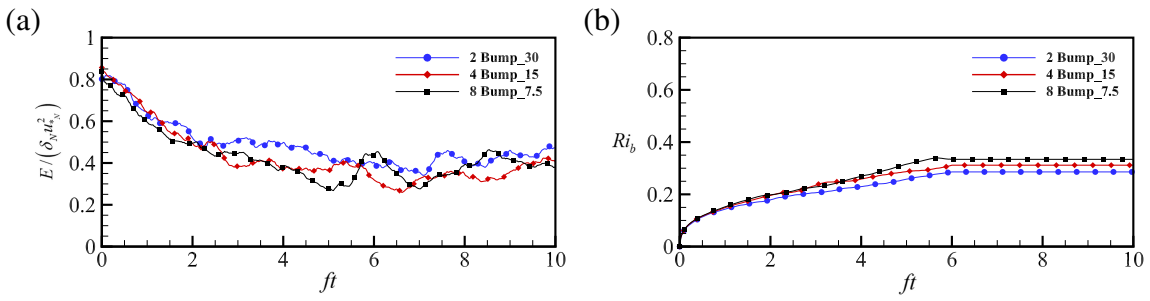

Figure 5.3: (a) Time series of integrated turbulent kinetic energy ($E/(\delta_N u_{*_N}^2)$) and (b) bulk Richardson number (Ri_b) for 2Bump$_{30}$ (blue), 4Bump$_{15}$ (red) and 8Bump$_{7.5}$ (black). The subscript number stand for the roughness height in wall unit, h^+.

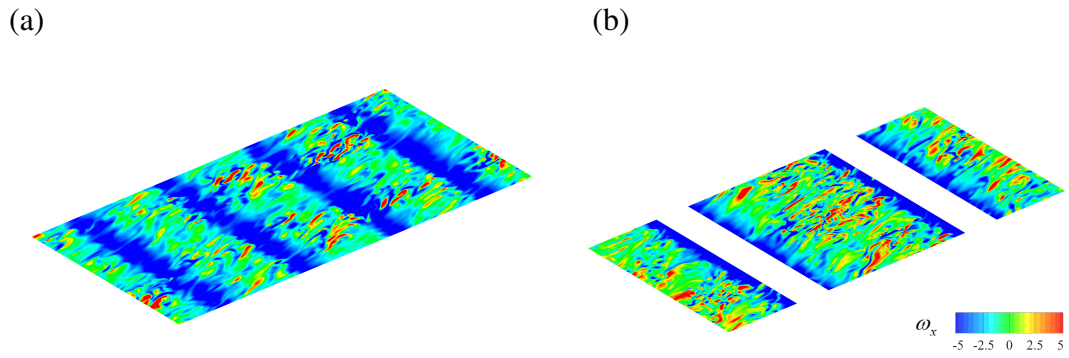

Figure 5.4: Streamwise vorticity contour on a horizontal plane at $z^+ \approx 16$ at $ft \approx 6$: (a) 4Bump$_{15}$, and (b) 2Bump$_{30}$

Table 5.3: DNS parameters* in the series where the surface buoyancy flux is varied for the 4Bump case and $Re_* \approx 700$. The subscript on the case label stands for the normalized Obukhov length scale, L^+

Case	Re_*	Ri_b	Initial L^+	h^+	l^+	AR (l/h)	$N_x \times N_y \times N_z$	Δx^+, Δy^+, Δz^+_{min}
4Bump_{700}	668	**0.312**	700	15	175	11.6	$481 \times 256 \times 129$	5.55, 5.20, 0.71
4Bump_{600}	668	**0.444**	600	15	175	11.6	$481 \times 256 \times 129$	5.55, 5.20, 0.71
4Bump_{500}	668	**0.563**	500	15	175	11.6	$481 \times 256 \times 129$	5.55, 5.20, 0.71
4Bump_{400}	668	**0.851**	400	15	175	11.6	$481 \times 256 \times 129$	5.55, 5.20, 0.71
4Bump_{250}	668	**1.442**	250	15	175	11.6	$481 \times 256 \times 129$	5.55, 5.20, 0.71

* Here l is the streamwise half-length of the bump and is related to λ (the roughness wave length) by λ=4l.

5.2.3 Effect of surface buoyancy flux

In chapter 3, we found that surface roughness changes the thermal structure of the Ekman boundary layer and enhances near-surface transport. In particular, for a given $L^+ \approx 700$, the introduction of roughness elements with sufficient steepness as in the 4Bump case changed the turbulence regime form strongly stable in the flat-bottom case to weakly stable. In this series of simulations, the effect of increasing surface buoyancy B_s is investigated in rough-bottom cases. We change the value of initial L^+ in the 4Bump case and assess changes in the behavior of the stratified EBL. A question of particular interest is as follows: Can surface cooling overcome the destabilizing effect of roughness to revert the flow to a strongly stable regime of intermittent turbulence or even relaminarize the EBL?

Figure 5.5 shows the time evolution of normalized volume-integrated turbulent kinetic energy and bulk Richardson number for 4Bump cases with different initial L^+. The subscript to the case label stands for the normalized Obukhov length scale (L^+). It is noteworthy that, with a sufficiently large stabilizing buoyancy flux of $L^+ = 250$, the 4Bump case reaches $Ri_b = 1.44$ which, as per the current DNS, is sufficient to completely relaminarize the EBL and keep it so until the end of the simulation at $ft = 20$. The flat case of Gohari and Sarkar (2018) that had a

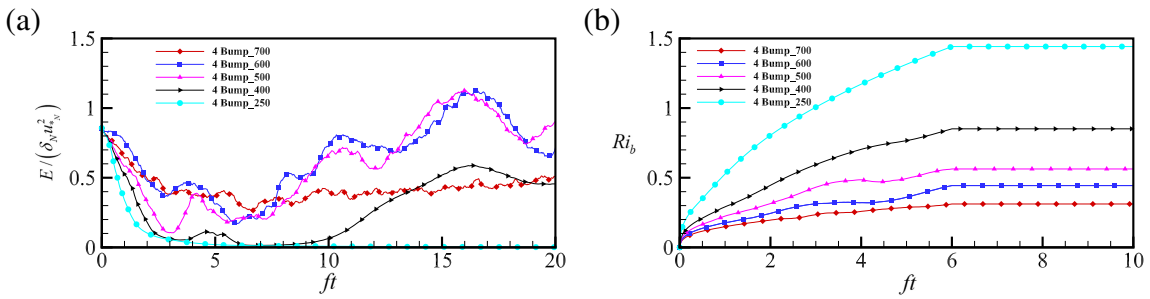

Figure 5.5: Time series of integrated turbulent kinetic energy ($E/(\delta_N u_{*_N}^2)$) and bulk Richardson number (Ri_b) in 4Bump cases with different values of the prescribed surface buoyancy flux. The subscript to the label stands for the normalized Obukhov length scale, L^+.

combination of $L^+, ft_{cooling}, Re_*$ that led to final $Ri_b = 1.45$ and 1.96 had final flow states that, similar to the current rough case with $Ri_b = 1.44$, was also laminar. The flat case of Gohari and Sarkar (2018) whose final $Ri_b = 0.91$ had negligible TKE after its intial collapse but recovered to a state with spatially intermittent turbulence similar to the present case 4Bump_{400} with final $Ri_b = 0.851$ where the flow also recovers to a state of local intermittency.

5.3 Results at higher Reynolds Number

In chapter 3, we fixed the surface buoyancy flux to a value sufficient for turbulence collapse during the initial transient and changed the number of bumps (equivalently the steepness of the roughness element) to evaluate surface roughness effects. In section 5.2.3 of the present chapter, we varied the value of the surface buoyancy flux measured by L^+. We found that the introduction of roughness elements with height of $h^+ = 15$ and the reduction of L^+, each decreased the overall stability of the flow. These results were obtained at a low Reynolds number $Re_* = 700$. At high Reynolds number, the viscous scale is reduced and therefore the surface roughness (at fixed $h^+ = 15$) has smaller height relative to the boundary layer height. In order to examine the robustness of our results, simulations are conducted at a larger $Re_* = 1100$. Results are presented for a flat-bottom EBL with varying L^+ in section 5.3.1 and for the 4Bump surface,

again with varying L^+, in section 5.3.2. The surface buoyancy flux is applied over the interval of $ft = 6$ for all cases.

5.3.1 Flat case with different values of surface buoyancy flux

Table 5.4 summarizes the DNS parameters of the Flat case at the higher Reynolds number of $Re_* \approx 1100$ and with different values of the surface buoyancy flux. The superscript on the case label stands for the friction Reynolds number, Re_*, and the subscript for the normalized Obukhov length scale, L^+.

Table 5.4: DNS parameters of the series where the surface buoyancy flux is varied for the flat-bottom case at higher Reynolds number. The superscript on the case label stands for the friction Reynolds number, Re_*, and the subscript stands for the normalized Obukhov length scale, L^+.

Case	Re_*	Ri_b	Initial L^+	Cooling period	$N_x \times N_y \times N_z$	Δx^+, Δy^+, Δz^+_{min}
^{1100}Flat	1112	-	∞	6	$513 \times 418 \times 225$	8.89, 5.44, 0.99
^{1100}Flat$_{1100}$	1112	**0.331**	1069	6	$513 \times 418 \times 225$	8.89, 5.44, 0.99
^{1100}Flat$_{700}$	1112	**0.794**	700	6	$513 \times 418 \times 225$	8.89, 5.44, 0.99
^{1100}Flat$_{500}$	1112	**1.425**	501	6	$513 \times 418 \times 225$	8.89, 5.44, 0.99

* N_x, N_y, and N_z are the number of nodes (grid points) in the streamwise, spanwise, and vertical direction, respectively.

Figure 5.6 shows the iso-surface of λ_2, colored by streamwise vorticity, for the unstratified Flat case with $Re_* = 700$ (^{700}Flat) and $Re_* = 1100$ (^{1100}Flat). It is clear from the visualization that increasing the Reynolds number reduces the viscous scale so that the thickness of the inclined vortical structures become smaller. The number density of the vortical structures is also increased at the higher value of Re_*.

The ^{1100}Flat$_{1100}$ case has the same surface buoyancy flux as the previous Flat$_{700}$ case at the lower $Re_8 = 700$. Even with the same buoyancy flux, since increasing Re_* reduces

(a)

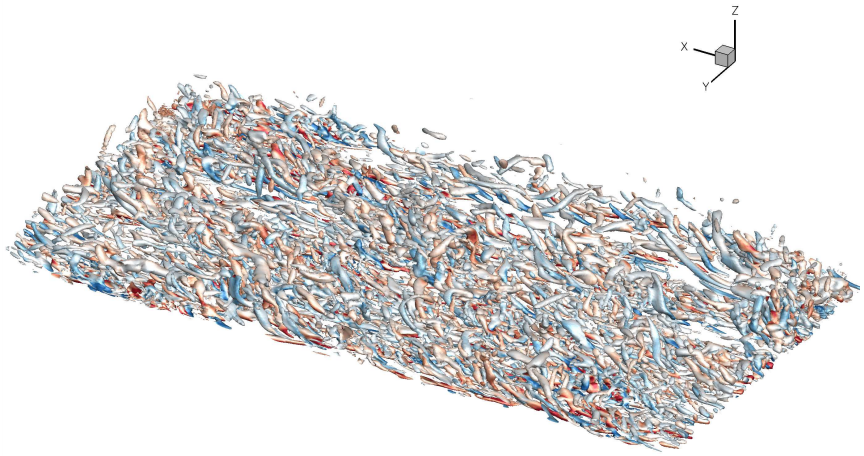

(b)

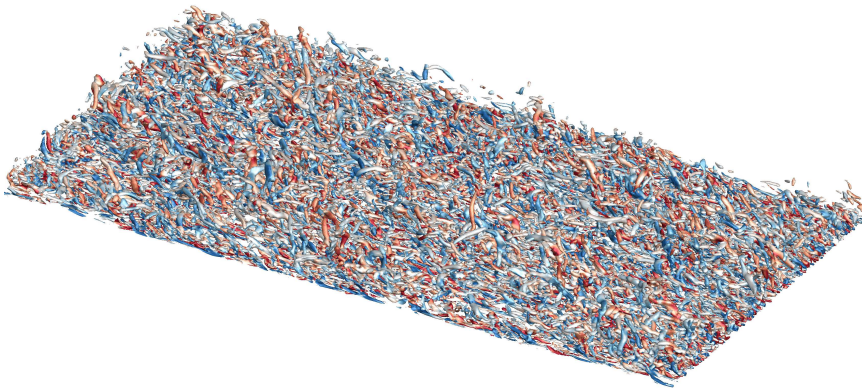

Figure 5.6: Isometric view of the λ_2 iso-surface ($\lambda_2 = -3.125(u_{*N}/z)^2$), colored by streamwise vorticity (ω_x), in the unstratified flat-bottom EBL: (a) $Re_* = 700$ and (b) $Re_* = 1100$.

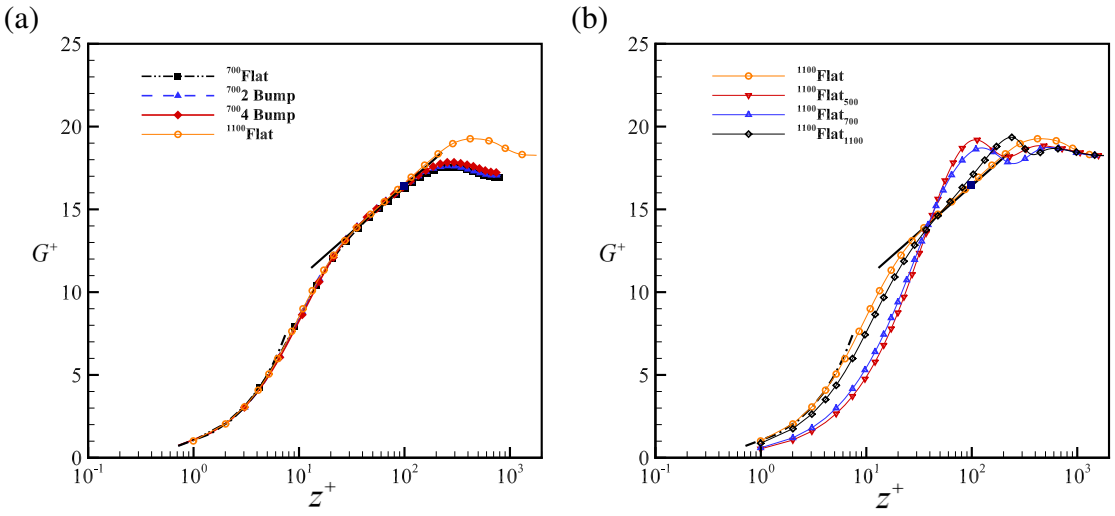

Figure 5.7: Mean velocity profiles: (a) unstratified cases (^{700}Flat, ^{700}2Bump, ^{700}4Bump) at $Re_* = 700$ are compared with the ^{1100}Flat case, and (b) ^{1100}Flat cases with different values of surface buoyancy flux. The logarithmic law with $\kappa = 0.41$ and $B = 5.3$ is also shown.

the viscous length scale of Ekman layer, the value of L^+ increases. This case with increased $L^+ = 1069 \approx 1100$ is examined to assess stabilization by buoyancy when the Reynolds number is increased. Additionally, ^{1100}Flat$_{700}$ and ^{1100}Flat$_{500}$ cases with higher values of surface buoyancy flux, i.e. lower values of L^+ are are also simulated.

Figure 5.7 shows the magnitude of normalized mean horizontal velocity, denoted by $G^+ = \sqrt{\langle u \rangle^2 + \langle v \rangle^2}$, as a function of normalized vertical distance from the wall. The solid line represents a log-law profile with the Von Karman constant κ=0.41 and B = 5.3. Profiles of the velocity in the unstratified (Figure 5.7 a) flat and bump cases are compared with the higher Reynolds number Flat case(^{1100}Flat). The statistics are obtained by averaging over the horizontal x-y plane and a half inertial period ($ft \approx \pi$). Beyond $z^+ \approx 30$, mean velocity profiles follow the log law and the log law region is elongated at the higher Reynolds number. In the stratified cases (Figure 5.7 (b)), the mean velocity profile is altered by buoyancy. With increasing surface buoyancy flux (decreasing L^+), the flow changes to weakly stable and then strongly stable regimes, similar to the behavior at lower $Re_* = 700$.

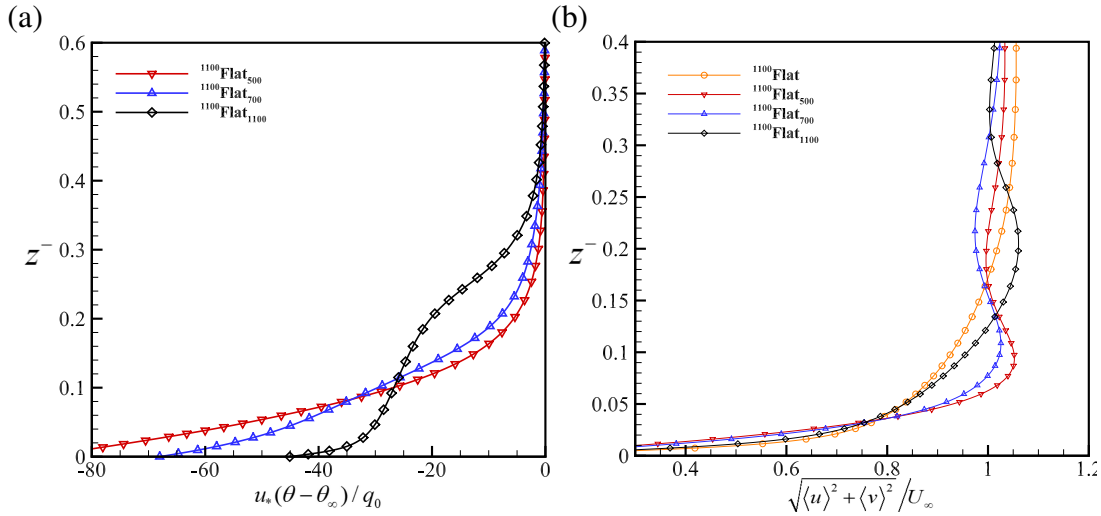

Figure 5.8: Influence of varying the surface buoyancy flux in the flat-bottom case with $Re_* = 1100$: (a) potential temperature ($u_{*_N}(\theta-\theta_\infty)/q_0$), and (b) velocity ($G=\sqrt{\langle u\rangle^2+\langle v\rangle^2}$). The statistics are obtained by averaging over the horizontal plane and half an inertial time period ($ft \approx \pi$).

Figure 5.8 shows profiles of the normalized potential temperature ($u_{*_N}(\theta-\theta_\infty)/q_0$) and the velocity ($G=\sqrt{\langle u\rangle^2+\langle v\rangle^2}$). In the stratified EBL (figure 5.8 a), the application of surface buoyancy flux changes the near-surface temperature distribution substantially. Strong near-surface inversion of temperature profile is observed for the ^{1100}Flat$_{500}$ and ^{1100}Flat$_{700}$ cases in figure 5.8 (a). Such a strong inversion is a feature of the very stable boundary layer. In contrast, the buoyancy flux of ^{1100}Flat$_{1100}$ case is not sufficient to stabilize the flow as much and its temperature profile, similar to the ^{700}4Bump$_{700}$ case, has a surface layer which is more mixed and reminiscent of a weakly stable boundary layer. This distinction among the cases is also reflected in the velocity profiles of figure 5.8 (b). A low-level jet (LLJ) with super-geostrophic velocity forms in the surface layer because of the strong surface buoyancy flux. As L^+ increases, the peak of the LLJ moves upwards and the LLJ profile broadens. This effect of weakening stability is similar to the introduction of surface roughness with increasing element steepness as was discussed in chapter 3.

The previously discussed results at the low $Re_* = 700$ showed that the final Ri_b provides

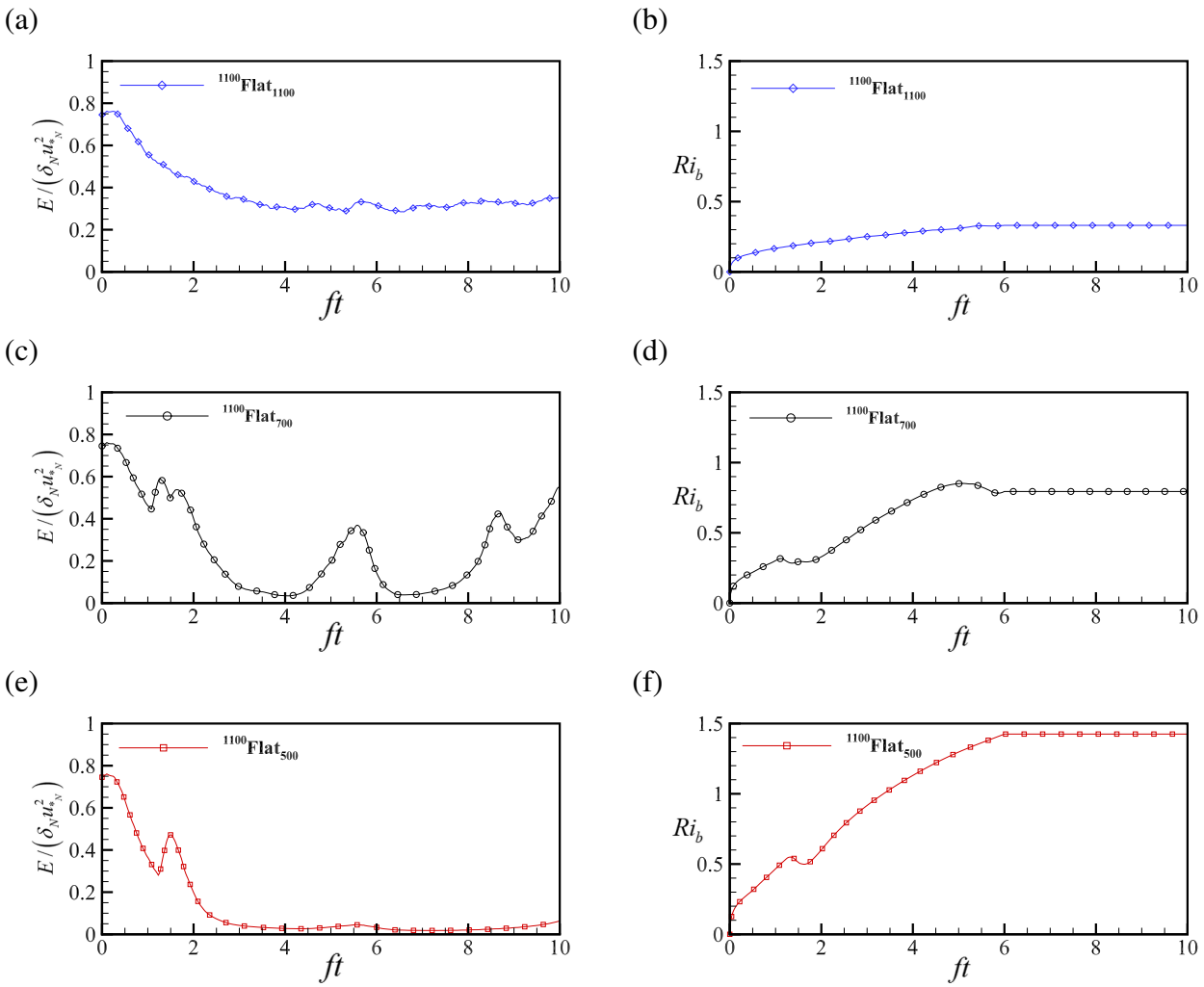

Figure 5.9: (a) Overall behavior of the stratified Flat cases at $Re_* \approx 1100$: (a,b) $^{1100}\text{Flat}_{1100}$ cases, (c,d) $^{1100}\text{Flat}_{700}$ cases, and (e,f) $^{1100}\text{Flat}_{500}$ cases. Left column shows integrated turbulent kinetic energy ($E/(\delta_N u_{*_N}^2)$) and right column shows bulk Richardson number (Ri_b).

guidance to the overall state of the flow and this guidance was not sensitive to the variation in the present simulations of roughness, the value of applied surface buoyancy flux and the duration of its application. Ri_b less than approximately 0.4 identifies a weakly stable boundary layer that has a weak thermal inversion and where the state of continuous turbulence is maintained. When Ri_b exceeds 0.4 the flow transitions to a very stable boundary layer which exhibits significant oscillations of TKE and a LLJ. When the final Ri_b takes values increasingly beyond 0.4, the temporal and spatial intermittency increases, there is cyclical collapse and rebirth of turbulence, and the amplitude of the LLJ increases. At sufficiently large Ri_b (about 1.4), there is complete turbulence collapse during the initial transient and turbulence does not recover because the LLJ induced shear or the roughness-induced fluctuations are not sufficient to overcome the strong near-surface stratification and the near-surface values of the gradient Richardson number (Ri_g) exceed 0.25.

The robustness of the final value of Ri_b as a flow-regime diagnostic is assessed in Figure 5.9 which shows the temporal evolution of integrated TKE and bulk Richardson number at the higher $Re_* = 1100$. The final value of Ri_b for ${}^{1100}\text{Flat}_{1100}$, ${}^{1100}\text{Flat}_{700}$, ${}^{1100}\text{Flat}_{500}$ case is 0.331, 0.794, and 1.425, respectively. The Ri_b-guided prediction inferred from the lower-Re_* results is that ${}^{1100}\text{Flat}_{1100}$ is weakly stable with continuous turbulence, ${}^{1100}\text{Flat}_{700}$ is in the very stable regime with intermittent turbulence, and ${}^{1100}\text{Flat}_{500}$ is in the very stable regime where turbulence does not recover after collapse. The evolution of TKE in the left column of Figure 5.9 is in agreement with this prediction.

The influence of surface buoyancy flux on horizontal fluctuations ($u_{h,rms} = \sqrt{u_{rms}^2 + v_{rms}^2}$) and vertical ($w_{rms}$) fluctuations is shown in figure 5.10 (a) and (b), respectively. The averaging time window is chosen from $ft = 6$ to $ft = 9.14$ which is half the inertial period ($ft = \pi$). Increasing the surface buoyancy flux (decreasing L^+) damps all components of velocity fluctuation so that both $u_{h,rms}$ and w_{rms} decrease. The reduction of peak w_{rms} in figure 5.10 (b) is stronger than the reduction of peak $u_{h,rms}$ in figure 5.10 (a) pointing to the anisotropic stabilization by buoyancy

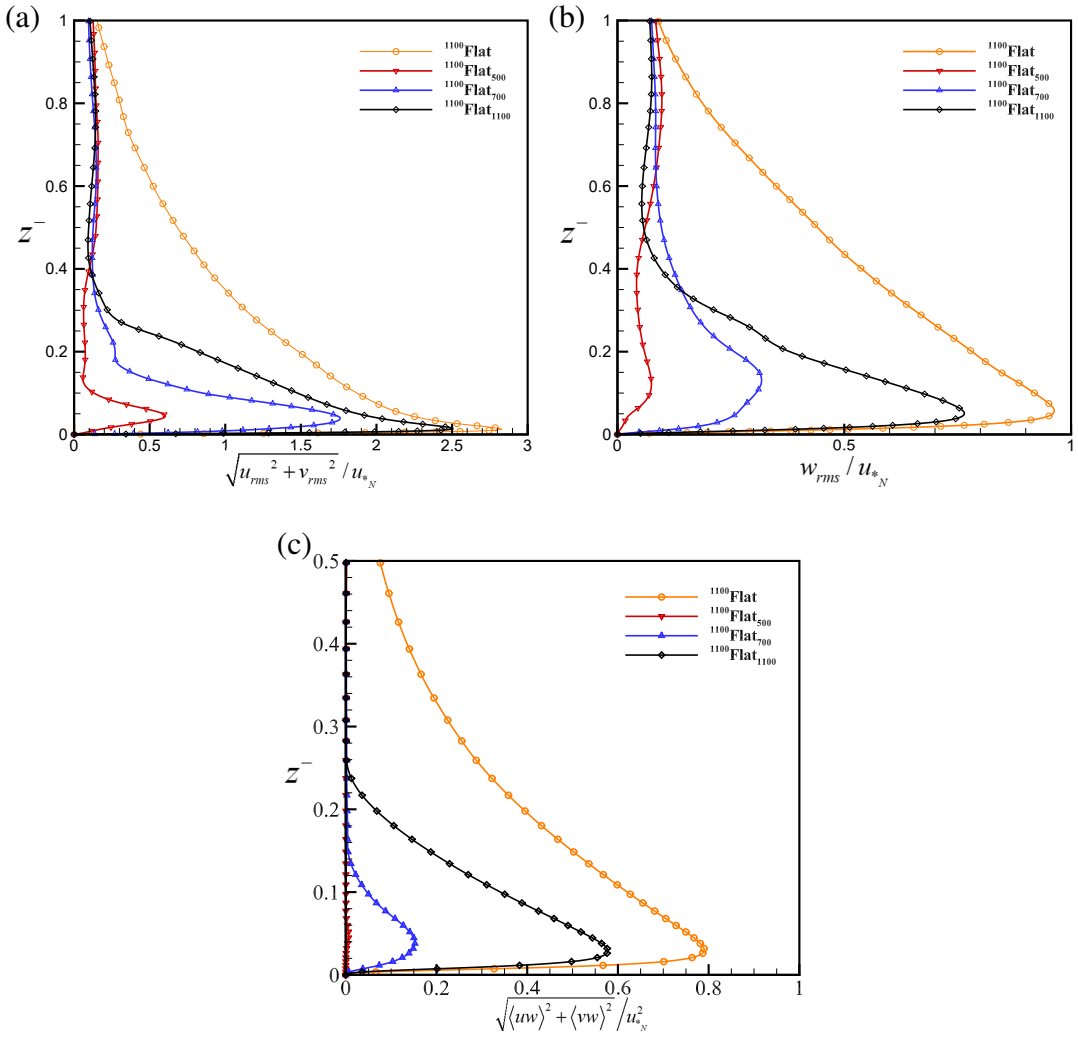

Figure 5.10: Time averaged profiles of velocity fluctuation statistics contrasted between unstratified (left column) and stratified (right column) conditions: (a) horizontal velocity fluctuations,($\sqrt{u_{rms}^2 + v_{rms}^2}$), (b) vertical velocity fluctuations, (w_{rms}), and (c) turbulent momentum flux.$\sqrt{\langle u'w'\rangle^2 + \langle v'w'\rangle^2}/u_{*_N}^2$.

which preferentially suppresses fluctuations in the vertical velocity component. The turbulent momentum flux ($\sqrt{\langle u'w'\rangle^2 + \langle v'w'\rangle^2}/u_{*_N}^2$) is plotted in figure 5.10 (c). The stratification of the $L^+ = 500$ case is strong enough to damp the momentum flux to almost zero. Therefore, TKE in the $L^+ = 500$ case is unable to recover at late time after its initial collapse as shown in figure 5.9.

We have seen that, in the stratified EBL, decreasing the surface buoyancy flux is similar to the introduction of surface roughness insofar as diminishing the stabilization by buoyancy (i.e. diminishing the final Ri_b) and enhancing the level of TKE. However, differences in the nature of turbulence enhancement are revealed upon comparison of the r.m.s profiles in figure 5.10 with the stratified cases in the right column of figure 3.13. For instance, the w_{rms} profile in the stratified 4Bump case (figure 3.13 d) shows a nonuniform augmentation with respect to the flat case: there is a substantial increase in its near-surface value but the value in the outer layer ($z^- > 0.2$) decreases. In contrast, decreasing the surface buoyancy flux by increasing L^+ in the flat case (figure 5.10 b) enhances w_{rms} throughout the boundary layer.

5.3.2 4 Bump case with different values of surface buoyancy flux

Roughness tends to enhance turbulence while cooling buoyancy flux applied to the surface tends to diminish turbulence. In the present section, we investigate how roughness in the form of the 4Bump surface geometry responds to the different values of surface buoyancy flux considered in section 5.3.1 for the flat case. A question of particular interest is whether the surface roughness provides sufficient destabilization to counteract buoyancy and maintain turbulence in the case with $L^+ = 500$. Recall that turbulence did not recover in the flat case with $L^+ = 500$. Table 5.5 summarizes the DNS parameters of the 4Bump case with different values of surface buoyancy flux simulated at the higher Reynolds number of $Re_* \approx 1100$. The superscript to the case label stands for the friction Reynolds number, Re_*, and the subscript for the normalized Obukhov length scale, L^+.

Figure 5.11 contrasts the overall behavior of the stratified 4Bump cases with corresponding

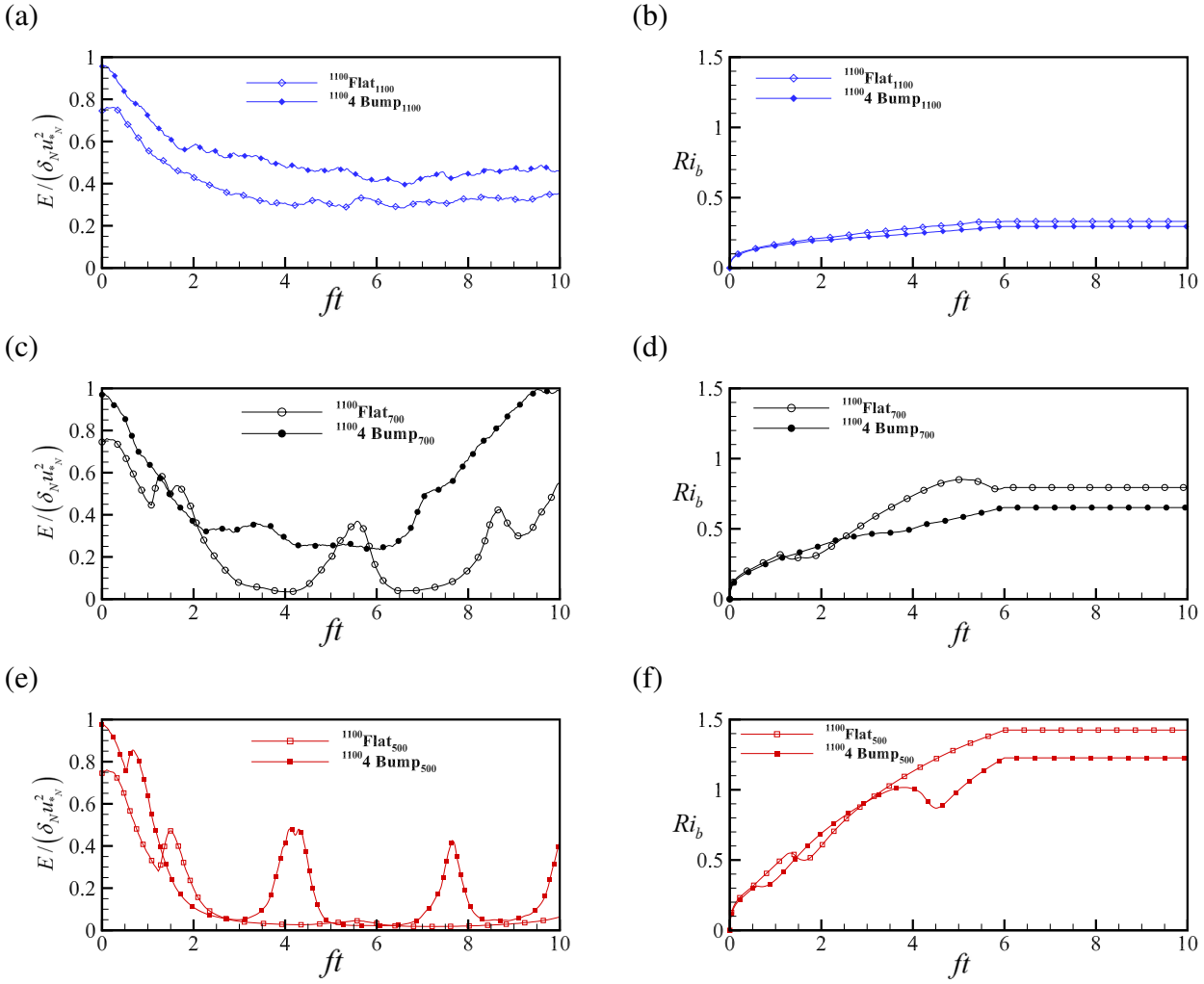

Figure 5.11: (a) Overall behavior of the stratified 4Bump cases at $Re_* \approx 1100$ comparison with Flat cases: (a,b) ^{1100}4Bump$_{1100}$ cases, (c,d) ^{1100}4Bump$_{700}$ cases, and (e,f) ^{1100}4Bump$_{500}$ cases. Left column shows integrated turbulent kinetic energy ($E/(\delta_N u_{*_N}^2)$) and right column shows bulk Richardson number (Ri_b).

Table 5.5: DNS parameters* of the series for the 4Bump case at higher Reynolds number where, similar to table 5.4 for the flat-bottom case, the surface buoyancy flux is varied. The superscript on the case label stands for the friction Reynolds number, Re_*, and the subscript stands for the normalized Obukhov length scale, L^+.

Case	Re_*	Ri_b	Initial L^+	h^+	l^+	$N_x \times N_y \times N_z$	Δx^+,Δy^+,Δz^+_{min}
^{1100}4Bump	1129	-	∞	15	175	$769 \times 418 \times 225$	5.55, 5.20, 0.71
^{1100}4Bump$_{1100}$	1129	**0.295**	1100	15	175	$769 \times 418 \times 225$	5.55, 5.20, 0.71
^{1100}4Bump$_{700}$	1129	**0.651**	700	15	175	$769 \times 418 \times 225$	5.55, 5.20, 0.71
^{1100}4Bump$_{500}$	1129	**1.227**	577	15	175	$769 \times 418 \times 225$	5.55, 5.20, 0.71

* N_x, N_y, and N_z are the number of nodes (grid points) in the streamwise, spanwise, and vertical direction, respectively. Here l is the streamwise half-length of the bump and is related to λ (the roughness wave length) by λ=4l.

flat cases. Comparing the 4Bump cases with the flat cases, the initial value of TKE is higher because of surface roughness. At later time, generally the 4Bump cases have more fluctuation energy relative to the corresponding flat cases. The difference in the initial value of TKE is preserved during the time evolution of the two cases with $L^+ = 1100$ (Figure 5.11a) and there is little difference in the final value of Ri_b, which is approximately 0.3 (Figure 5.11b), placing these cases in the weakly stable regime. In figure 5.11 (d), the final values of Ri_b for ^{1100}4Bump$_{700}$ and ^{1100}Flat$_{700}$ are 0.651 and 0.794 (between 0.4 and 1.0), respectively. Although these values of Ri_b place both cases in the subclass of very stable regime where turbulence is maintained at long time, there are differences. TKE in the flat case collapses to almost zero during the intial transient in the flat case and then recovers. However, the initial decrease of TKE in the 4Bump case is more moderate. Both cases show an increase of TKE shortly after the surface cooling is removed at $ft \approx 6$. Figure 5.11 (e) compares the TKE evolution of the ^{1100}4Bump$_{500}$ case with the ^{1100}Flat$_{500}$ case; both cases have a large surface buoyancy flux corresponding to $L^+ = 500$. Turbulence collapses to zero in the flat case and does not recover. Roughness elements are somewhat effective in counteracting the extinction of turbulence by stratification, e.g. TKE recovers at $ft \approx \pi$ in the 4Bump case. However, later at $ft \approx 5$, the roughness-induced fluctuations are not sufficient to

overcome the strong stratification and TKE again becomes negligible. The competition between roughness and buoyancy in the $^{1100}4\text{Bump}_{500}$ case leads to a cyclic pattern of TKE collapse followed by rebirth. The final value of $Ri_b = 1.23$ in this case places it squarely in the very stable regime but, with its cyclic behavior of collapse and rebirth, it is different from lower values of Ri_b (e.g. between 0.4 and 1.0) in the very stable regime where turbulence recovers without intermittently collapsing at later time and it is also different from higher values of Ri_b (e.g. larger than 1.4) where turbulence does not recover at all.

Figure 5.12 compares contours of integrated turbulent kinetic energy ($E/(\delta_N u_{*_N}^2)$) and gradient Richardson number (Ri_g) between Flat and 4Bump cases for two values of the surface buoyancy flux: L^+ = 500 and 1100. Comparison between figure 5.12 (b) and (d) shows that changing the surface buoyancy flux influences the local stability measure, i.e. gradient Richardson number, $Ri_g(z,t)$. The thickness of the subcritical region with $Ri_g < 0.25$ is substantially reduced for $L^+ = 500$ relative to $L^+ = 1100$ in the flat-bottom cases, leading to turbulence collapse in the case with $L^+ = 500$ as shown in figure 5.12 (c). The effect of the surface roughness becomes clear upon comparison of the second row (flat) with the third row (4Bump) of the figure. Comparison of panels (c) and (e) show that, after the intial collapse, there are cyclic bursts of turbulence in the 4Bump case. These originate in the region of Ri_g (plotted in panel (f)) with subcritical values less than 0.25. However, turbulence is unable to persist after rebirth because the increased buoyancy flux of the $L^+ = 500$ cases is able to stabilize the upper region of the boundary layer for both rough and smooth surfaces. After $ft \approx 6$, the Ri_g values in the $z^- > 0.2$ region are similar between the 4 bump and flat cases.

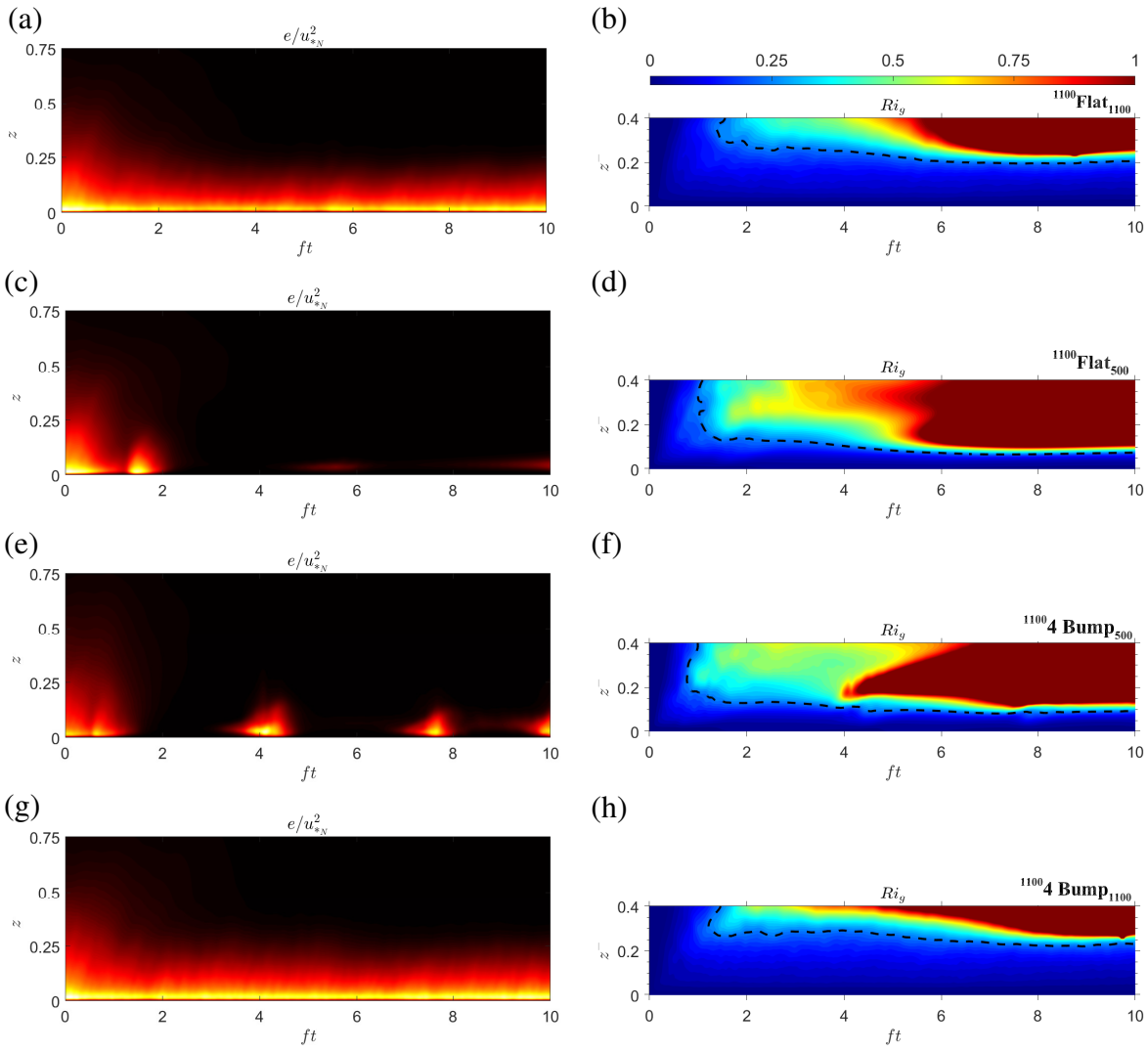

Figure 5.12: Contours of (left column) integrated turbulent kinetic energy($E/(\delta_N u_{*_N}^2)$) and (right column) gradient Richardson number (Ri_g): (a,b) ^{1100}Flat$_{1100}$, (c,d) ^{1100}Flat$_{500}$, (e,f) ^{1100}4Bump$_{500}$, and (g,h) ^{1100}4Bump$_{1100}$ cases. The black dashed line shows $Ri_g = 0.25$.

Chapter 6

Summary and conclusions

In this study, we perform a direct numerical simulation (DNS) study of neutral and stably stratified turbulent Ekman layers where the stable stratification is imposed by applying a cooling buoyancy flux. The stratified Ekman boundary layer (EBL) has served as a canonical problem that is amenable to high-resolution simulation and is relevant to the stratified ABL. However, roughness effects in the EBL have not been studied previously using DNS. This motivates the present investigation of an EBL on a surface with two-dimensional bumps.

Chapter 3 reports a DNS study where the Reynolds number (Re_*) based on friction velocity is fixed at approximately 700, the cooling flux is fixed at a nondimensional value of $L^+ \approx 700$ which is sufficient to induce turbulence collapse during the initial transient (Gohari and Sarkar, 2018), the roughness amplitude is fixed at a small value in the transitionally-rough regime, and the slope of the elements (equivalently, number of bumps per unit length) is varied. The focus is on the competition between flow stabilization by buoyancy and possible destabilization by the roughness.

We find that the flow evolution is substantially affected by roughness in the stratified EBL, especially so in the case with 4Bumps, the case with the highest number of bumps per unit length and also the highest geometrical slope. In the 4Bump case, the minimum TKE reached during

the initial turbulence collapse is significantly larger than in the Flat case. Furthermore, later in time after turbulence recovery, the near-surface flow state is continuously turbulent in the 4Bump case in contrast to the local intermittency (turbulent patches interspersed within quiescent regions of near-laminar flow) in the Flat and 2Bump cases. The MO stability functions show that, at locations where z is not small compared to the local Obukhov length, buoyancy affects the mean momentum and temperature profiles. Furthermore, this buoyancy effect is substantially weaker in the 4Bump case although the applied surface cooling flux is identical among cases. By increasing the number of bumps per unit length keeping bump height constant, the slope of the roughness element is systematically increased in the present DNS. It is the increase in slope that enhances the magnitude of the roughness-associated effect on turbulence from 2Bump to 4Bump cases.

Mahrt (1998) classifies the stable ABL into two regimes: (i) a very stable ABL that has a strong thermal inversion at the surface and vertical fluctuations which, although very small near the surface, have a peak at an elevated location, and (ii) a weakly stable ABL that has a weak thermal inversion and vertical fluctuations that, although somewhat reduced near the surface with respect to the neutral state, are substantial and do not display a peak at an elevated location. Examination of mean and turbulence profiles in the DNS results reveal that the Flat case belongs to the very stable regime while the 4Bump case belongs to the weakly stable regime. Here, we find that, for the same environmental forcing, roughness elements induce a qualitative change in the boundary layer, namely, from the strongly stable regime to the weakly stable regime. As the neutral BL thins and near-surface turbulence weakens during the initial response to the applied cooling flux, the reach of the roughness elements is sufficient to keep the local gradient Richardson number from becoming supercritical (exceeding $1/4$) and concurrently maintain turbulence structures. The present result is obtained for a relatively low-Re flow amenable to DNS, where the roughness elements correspond to a transitionally rough regime. It is possible that, at higher Re and in a fully rough ABL, roughness elements can also lead to a qualitatively similar destabilization if their reach becomes sufficient compared to the buoyancy-induced thinning of

the ABL.

The mechanism of turbulence collapse and rebirth is investigated in detail with the analysis of turbulent fluxes. The inhibition of surface-layer shear production, associated with the buoyancy-induced reduction of the turbulent momentum flux, is the reason for turbulence collapse as was found by Ansorge and Mellado (2014); Shah and Bou-Zeid (2014), and is not associated with the TKE decrease by the positive buoyancy flux. Collapse is followed by turbulence recovery in both flat and rough cases. Notably, the mechanism of turbulence recovery in the rough cases is different from that in the Flat case. In the Flat case, a strong LLJ is formed at the end of turbulence collapse and, as found by Gohari and Sarkar (2017), pressure transport of fluctuations from the outer layer into the sheared lower flank of the LLJ triggers locally intermittent turbulence as the fluctuations interact with the enhanced shear of the LLJ. In contrast, we find in the 4Bump case that the enhanced vertical (w) velocity in the near-surface roughness layer enhances the turbulent momentum flux and thus increases TKE production (P). Also, unlike the Flat case, P does not decay to zero in the rough cases during the intial collapse of turbulence.

It is worth noting that the small-amplitude ($z^+ = 15$) roughness considered here has very little effect on the flow in the absence of stratification. However, the amplitude is sufficient for the influence of roughness to reach into the boundary-layer region where buoyancy-induced suppression of turbulent fluxes has commenced. Here, small-amplitude roughness height is less than ($z^+ < 30$), which is the range of the buffer layer.

To characterize the influence of rotation on turbulence structures and large-scale motions, we repeated DNS of the Ekman boundary layer at the moderate Reynolds number $Re_* \approx 700$ in a large domain ($16\ \delta_N \times 4\ \delta_N \times 2\ \delta_N$) which is 8 times larger than the previous simulation ($4\ \delta_N \times 2\ \delta_N \times 2\ \delta_N$). The large-scale structures of an EBL are compared to those of a channel and the premultiplied two-dimensional spectra of the velocity fluctuations are compared. Linear stability analysis is conducted to reveal the existence of unstable modes which sustain the transverse outer-layer roll structures observed in visualizations of the streamwise velocity.

We further investigated the stratified rough boundary layer by conducting additional parametric studies where cooling flux, cooling time and roughness height (keeping aspect ratio constant) were independently varied. For the two-dimensional bumps in the transitionally rough regime considered here, the height of the roughness element is not the key governing geometrical parameter. Instead, the steepness of the surface roughness is more important. Increasing the cooling time and decreasing the cooling flux reduce the net amount of stabilizing buoyancy added to the flow and, similar to the introduction of roughness elements, have the overall effect of increasing turbulence levels in the EBL. A significant difference is that roughness preferentially increases vertical velocity fluctuations in the near-surface region while a decrease in the cooling flux or cooling time leads to an increase of velocity fluctuations which is more uniform across the boundary-layer depth.

Taking account of all the simulations, the overall state of the flow can be classified into weakly stable and strongly stable regimes in the sense of Mahrt (1998). We also find that the final value of Ri_b provides sufficient guidance to determining the overall state of the flow and, furthermore, distinguishes among different states of intermittency of fluctuations in the very stable regime. When the final Ri_b takes values below 0.4, the flow is a weakly stable boundary layer which has a weak thermal inversion and a state of continuous turbulence is maintained. When the final Ri_b takes values from 0.4 to 1.0, there is a regime change to a very stable boundary layer where, after the initial collapse, turbulence recovers albeit with near-inertial oscillations of TKE with amplitude that increases with increasing Ri_b. When Ri_b lies between 1.0 and 1.4 and the stratification is somewhat stronger, the competition between buoyancy and turbulence leads to a cyclic pattern of TKE with successive cycles of complete collapse of turbulence followed by rebirth. When the value of final Ri_b is over 1.4, turbulence does not recoverer at all after its initial collapse.

Bibliography

André, J. C. and Mahrt, L. (1982). The nocturnal surface inversion and influence of clear-air radiative cooling. *J. Atmos. Sci.*, 39(4):864–878.

Ansorge, C. and Mellado, J. P. (2014). Global intermittency and collapsing turbulence in the stratified planetary boundary layer. *Boundary-Layer Meteorol.*, 153(1):89–116.

Armenio, V. and Sarkar, S. (2002). An investigation of stably-stratified channel flow using large eddy simulation. *J. Fluid Mech.*, 459:1–42.

Balakumar, B. and Adrian, R. (2007). Large-and very-large-scale motions in channel and boundary-layer flows. *Philosophical Transactions of the Royal Society A: Mathematical, Physical and Engineering Sciences*, 365(1852):665–681.

Baltzer, J., Adrian, R., and Wu, X. (2013). Structural organization of large and very large scales in turbulent pipe flow simulation. *Journal of Fluid Mechanics*, 720:236–279.

Banta, R. (2008). Stable-boundary-layer regimes from the perspective of the low-level jet. *Acta Geophysica*, 56(1):58–87.

Banta, R., Newsom, R., Lundquist, J., Pichugina, Y., Coulter, R., and Mahrt, L. (2002). Nocturnal low-level jet characteristics over kansas during cases-99. *Boundary-Layer Meteorology*, 105(2):221–252.

Banta, R. M., Mahrt, L., Vickers, D., Sun, J., Balsley, B. B., Pichugina, Y. L., and Williams, E. J. (2007). The very stable boundary layer on nights with weak low-level jets. *J. Atmos. Sci.*, 64:3068–3090.

Basu, S. and Porté-Agel, F. (2006). Large-eddy simulation of stably stratified atmospheric boundary layer turbulence: a scale-dependent dynamic modeling approach. *jas*, 63(8):2074–2091.

Beare, R., Macvean, M., Holtslag, A., Cuxart, J., Esau, I., Golaz, J.-C., Jimenez, M., Khairoutdinov, M., Kosovic, B., Lewellen, D., Lund, T., Lundquist, J., Mccabe, A., Moene, A., Noh, Y., Raasch, S., and Sullivan, P. (2006). An intercomparison of large-eddy simulations of the stable boundary layer. *Boundary-Layer Meteorol.*, 118(2):247–272.

Blackadar, A. K. (1957). Boundary layer wind maxima and their significance for the growth of

nocturnal inversions. *Bull. Am. Meteorol. Soc.*, 38(5):283–290.

Brucker, K. and Sarkar, S. (2007). Evolution of an initially turbulent stratified shear layer. *Phys. Fluids*, 19:101105.

Brucker, K. A. and Sarkar, S. (2010). A comparative study of self-propelled and towed wakes in a stratified fluid. *J. Fluid Mech.*, 652:373–404.

Businger, J. A. (1973). Turbulence transfer in the atmospheric surface layer. In *Workshop on micrometeorology*, pages 67–100. Amer. Meteor. Soc.

Businger, J. A. and Arya, S. P. S. (1975). Height of the mixed layer in the stably stratified planetary boundary layer. In *Adv. Geophys.*, volume 18, pages 73–92. Elsevier.

Coleman, G. N., Ferziger, J. H., and Spalart, P. R. (1990). A numerical study of the turbulent ekman layer. *J. Fluid Mech.*, 213:313–348.

Cuxart, J. and Jiménez, M. A. (2007). Mixing processes in a nocturnal low-level jet: an LES study. *J. Atmos. Sci.*, 64:1666–1679.

Cuxart, J., Yagüe, C., Morales, G., Terradellas, E., Orbe, J., Calvo, J., Fernández, A., Soler, M., Infante, C., Buenestado, P., Espinalt, A., Joergensen, H., Rees, J., Vilá, J., Redondo, J., Cantalapiedra, I., and Conangla, L. (2000). Stable atmospheric boundary-layer experiment in Spain (SABLES 98): A Report. *Boundary-Layer Meteorol.*, 96(3):337–370.

Damiens, F., Millet, C., and Lott, F. (2018). An investigation of infrasound propagation over mountain ranges. *jasa*, 143(1):563–574.

De Angelis, V., Lombardi, P., and Banerjee, S. (1997). Direct numerical simulation of turbulent flow over a wavy wall. *Phys. Fluids*, 9:2429–2442.

Deardorff, J. W. (1972). Numerical investigation of neutral and unstable planetary boundary layers. *Journal of the Atmospheric Sciences*, 29(1):91–115.

Del Álamo, J. C. (2005). *The Large Scale Organization of Turbulent Channels. PhD. Thesis*. Universidad Politécnica de Madrid.

Del Alamo, J. C., Jiménez, J., Zandonade, P., and Moser, R. D. (2004). Scaling of the energy spectra of turbulent channels. *Journal of Fluid Mechanics*, 500:135–144.

Deusebio, E., Brethouwer, G., Schlatter, P., and Lindborg, E. (2014). A numerical study of the unstratified and stratified Ekman layer. *J. Fluid Mech.*, 755:672–704.

Finnigan, J. (2000). Turbulence in plant canopies. *Annu. Rev. Fluid Mech.*, 32:519–571.

Flack, K. A. and Schultz, M. P. (2010). Review of hydraulic roughness scales in the fully rough regime. *J. Fluids Engr.*, 132:041203–1–10.

Flores, O. and Riley, J. (2011). Analysis of turbulence collapse in the stably stratified surface layer using direct numerical simulation. *Boundary-Layer Meteorol.*, 139(2):241–259.

Flores, O. and Riley, J. J. (2018). Energy balance in stably-stratified, wall-bounded turbulence. *CISM Int. Centre Mech. Sci.*, 580:89–99.

Garcia-Villalba, M. and del Alamo, J. C. (2011). Turbulence modification by stable stratification in channel flow. *Phys. Fluids*, 23(4):045104.

Garcia-Villalba, M. and Del Alamo, J. C. (2011). Turbulence modification by stable stratification in channel flow. *Physics of Fluids*, 23(4):045104.

Garg, R. P., Ferziger, J. H., Monismith, S. G., and Koseff, J. R. (2000). Stably stratified turbulent channel flows. I. stratification regimes and turbulence suppression mechanism. *Phys. Fluids*, 12(10):2569–2594.

Gayen, B. and Sarkar, S. (2011). Direct and large-eddy simulations of internal tide generation at a near-critical slope. *J. Fluid Mech.*, 681:48–79.

Gohari, S. M. I. and Sarkar, S. (2017). Direct numerical simulation of turbulence collapse and rebirth in stably stratified ekman flow. *Boundary-Layer Meteorol.*, 162(3):401–426.

Gohari, S. M. I. and Sarkar, S. (2018). Stratified ekman layers evolving under a finite-time stabilizing buoyancy flux. *Journal of Fluid Mechanics*, 840:266–290.

Gong, W., Taylor, P. A., and Dornbrack, A. (1996). Turbulent boundary-layer flow over fixed aerodynamically-rough two-dimensional sinusoidal waves. *J. Fluid Mech.*, 312:1–37.

He, P. and Basu, S. (2015). Direct numerical simulation of intermittent turbulence under stably stratified conditions. *Nonlinear Processes in Geophysics Discussions*, 2(1):179–241.

Jacobitz, F. G., Sarkar, S., and VanAtta, C. W. (1997). Direct numerical simulations of the turbulence evolution in a uniformly sheared and stably stratified flow. *J. Fluid Mech.*, 342:231–261.

Jalali, M., Rapaka, N. R., and Sarkar, S. (2014). Tidal flow over topography: effect of excursion number on wave energetics and turbulence. *J. Fluid Mech.*, 750:259–283.

Jiménez, J. (2004). Turbulent flows over rough walls. *Annu. Rev. Fluid Mech.*, 36:173–196.

Jiménez, J., Del Álamo, J. C., and Flores, O. (2004). The large-scale dynamics of near-wall turbulence. *Journal of Fluid Mechanics*, 505:179–199.

Kosović, B. and Curry, J. A. (2000). A large eddy simulation study of a quasi-steady, stably stratified atmospheric boundary layer. *J. Atmos. Sci.*, 57:1052–1068.

Li, Q. and Bou-Zeid, E. (2019). Contrasts between momentum and scalar transport over very

rough surfaces. *J. Fluid Mech.*, 880:32–58.

Lozano-Durán, A. and Bae, H. J. (2019). Characteristic scales of townsend's wall-Attached eddies. *J. Fluid Mech.*, 868:698–725.

Mahrt, L. (1985). Vertical structure and turbulence in the very stable boundary layer. *J. Atmos. Sci.*, 42(22):2333–2349.

Mahrt, L. (1989). Intermittency of atmospheric turbulence. *Journal of the Atmospheric Sciences*, 46(1):79–95.

Mahrt, L. (1998). Stratified atmospheric boundary layers and breakdown of models. *Theoretical and computational fluid dynamics*, 11(3-4):263–279.

Mahrt, L. (1999). Stratified atmospheric boundary layers. *Boundary-Layer Meteorol.*, 90(3):375–396.

Melgarejo, J. W. and Deardorff, J. W. (1974). Stability functions for the boundary-layer resistance laws based upon observed boundary-layer heights. *J. Atmos. Sci.*, 31(5):1324–1333.

Metzger, M., McKeon, B., and Holmes, H. (2007). The near-neutral atmospheric surface layer: turbulence and non-stationarity. *Philosophical Transactions of the Royal Society of London A: Mathematical, Physical and Engineering Sciences*, 365(1852):859–876.

Monin, A. S. (1970). The atmospheric boundary layer. *Annual Review of Fluid Mechanics*, 2(1):225–250.

Napoli, E., Armenio, V., and Marchis, M. D. (2008). The effect of the slope of irregularly distributed roughness elements on turbulent wall-bounded flows. *J. Fluid Mech.*, 613:385–394.

Nieuwstadt, F. (2005). Direct numerical simulation of stable channel flow at large stability. *Boundary-Layer Meteorol.*, 116(2):277–299.

Nieuwstadt, F. T. M. (1984). The turbulent structure of the stable, nocturnal boundary layer. *J. Atmos. Sci.*, 41(14):2202–2216.

Obukhov, A. (1971). Turbulence in an atmosphere with a non-uniform temperature. *Boundary-Layer Meteorol.*, 2(1):7–29.

Ohya, Y. (2001). Wind-tunnel study of atmospheric stable boundary layers over a rough surface. *Boundary-Layer Meteorology*, 98(1):57–82.

Ohya, Y., Neff, D. E., and Meroney, R. N. (1997). Turbulence structure in a stratified boundary layer under stable conditions. *Boundary-Layer Meteorology*, 83(1):139–162.

Pichugina, Y. L., Tucker, S. C., Banta, R. M., Brewer, W. A., Kelley, N. D., Jonkman, B. J., and Newsom, R. K. (2008). Horizontal-velocity and variance measurements in the stable boundary

layer using doppler lidar: Sensitivity to averaging procedures. *Journal of Atmospheric and Oceanic Technology*, 25(8):1307–1327.

Poggi, D., Katul, G. G., and Anderson, J. D. (2004). A note on the contribution of dispersive fluxes to momentum transfer within canopies. *Boundary-Layer Meteorol.*, 111(3):615–621.

Poulos, G. S., Blumen, W., Fritts, D. C., Lundquist, J. K., et al. (2002a). Cases-99: A comprehensive investigation of the stable nocturnal boundary layer. *Bull. Amer. Meteorol. Society*, 83(4):555.

Poulos, G. S., Blumen, W., Fritts, D. C., Lundquist, J. K., Sun, J., Burns, S. P., Nappo, C., Banta, R., Newsom, R., Cuxart, J., Terradellas, E., Balsley, B., and Jensen, M. (2002b). Cases-99: A comprehensive investigation of the stable nocturnal boundary layer. *Bull. Amer. Met. Soc.*, 83(4):555–582.

Rapaka, N. R., Gayen, B., and Sarkar, S. (2013). Tidal Conversion and Turbulence at a Model Ridge: Direct and Large Eddy Simulations. *J. Fluid Mech.*, 715:181–209.

Raupach, M., Antonia, R., and Rajagopalan, S. (1991). Rough-wall turbulent boundary layers. *Applied mechanics reviews*, 44(1):1–25.

Reynolds, W. C. and Hussain, A. K. M. F. (1972). The mechanics of an organized wave in turbulent shear flow. part 3. theoretical models and comparisons with experiments. *J. Fluid Mech.*, 54(2):263–288.

Schmid, P. (2007). Nonmodal Stability Theory. *Ann. Rev. Fluid Mech.*, 39(1):129–162.

Schmid, P. J. and Henningson, D. S. (2001). *Stability and Transition in Shear Flows*.

Shah, S. K. and Bou-Zeid, E. (2014). Direct numerical simulations of turbulent Ekman layers with increasing static stability: modifications to the bulk structure and second-order statistics. *J. Fluid Mech.*, 760:494–539.

Shapiro, A. and Fedorovich, E. (2010). Analytical description of a nocturnal low-level jet. *Q. J. R. Meteorol. Soc.*, 136(650):1255–1262.

Shingai, K. and Kawamura, H. (2004). A study of turbulence structure and large-scale motion in the Ekman layer through direct numerical simulations. *J. Turb.*, 5:N13.

Smedman, A.-S., Tjernström, M., and Högström, U. (1993). Analysis of the turbulence structure of a marine low-level jet. *Boundary-Layer Meteorol.*, 66(1-2):105–126.

Spalart, P. R. (1988). Direct simulation of a turbulent boundary layer up to $Re_\theta = 1410$. *J. Fluid Mech.*, 187:61–98.

Stull, R. (1988). *An introduction to boundary layer meteorology*. Kluwer Academic Publishers.

Sullivan, P. P. and McWilliams, J. C. (2002). Turbulent flow over water waves in the presence of stratification. *Phys. Fluids*, 14:1182–1195.

Sullivan, P. P., McWilliams, J. C., and Moeng, C.-H. (2000). Simulation of turbulent flow over idealized water waves. *J. Fluid Mech.*, 404:47–85.

Sun, J., Mahrt, L., Banta, R., and Pichugina, Y. (2012). Turbulence regimes and turbulence intermittency in the stable boundary layer during CASES-99. *J. Atmos. Sci.*, 69:338–351.

Talmadge, C. L., Waxler, R., Xiao, D., Gilbert, K. E., and Kulichkov, S. (2008). Observation of low-frequency acoustic surface waves in the nocturnal boundary layer. *jasa*, 124(4):1956–1962.

Townsend, A. (1967). Wind and the formation of inversions. *Atmospheric Environment (1967)*, 1(2):173–175.

Van de Wiel, B. J. H., Moene, A. F., Steeneveld, G. J., Baas, P., Bosveld, F. C., and Holtslag, A. A. M. (2010). A conceptual view on inertial oscillations and nocturnal low-level jets. *J. Atmos. Sci.*, 67(8):2679–2689.

Williamson, J. H. (1980). Low-storage Runge-Kutta schemes. *Journal of Computational Physics*, 35(1):48–56.

Wilson, D. K., Noble, J. M., and Coleman, M. A. (2003). Sound propagation in the nocturnal boundary layer. *jas*, 60(20):2473–2486.

Yang, D. and Shen, L. (2010). Direct-simulation-based study of turbulent flow over various waving boundaries. *J. Fluid Mech.*, 650:131–180.

Zilitinkevich, S. (1972). On the determination of the height of the ekman boundary layer. *Boundary-Layer Meteorol.*, 3(2):141–145.

Zilker, D. P., Cook, G. W., and Hanratty, T. J. (1977). Influence of the amplitude of a solid wavy wall on a turbulent flow. part 1. non-separated flows. *J. Fluid Mech.*, 82:29–51.